Title

Nano-Electrochromic Active Plasmonics: Wireless Electrophysiology and Flat Optics

Permalink

https://escholarship.org/uc/item/1p87n9v0

Author

Habib, Ahsan

Publication Date

2021

Peer reviewed|Thesis/dissertation

UNIVERSITY OF CALIFORNIA
SANTA CRUZ

NANO-ELECTROCHROMIC ACTIVE PLASMONICS: WIRELESS ELECTROPHYSIOLOGY AND FLAT OPTICS

A dissertation submitted in partial satisfaction of the
requirements for the degree of

DOCTOR OF PHILOSOPHY

in

ELECTRICAL ENGINEERING

by

Ahsan Habib

December 2021

The Dissertation of Ahsan Habib
is approved:

Professor Ahmet Ali Yanik, Chair

Professor Holger Schmidt

Professor Marco Rolandi

Peter Biehl
Vice Provost and Dean of Graduate Studies

Table of Contents

List of Figures

List of Tables

To my parents,

Khandakar Habibullah and Surya Khanam

Abstract

Nano-Electrochromic Active Plasmonics: Wireless Electrophysiology and Flat Optics

by

Ahsan Habib

Active plasmonic devices have recently emerged as plasmonic/nanophotonic technologies with tunable optical characteristics. However, electro-optic effects in plasmonic metals are weaker than their photonic counterpart since plasmonic materials such as Au and Ag have extremely high electron densities, resulting in the effective screening of the externally applied electrical fields. In this thesis, to overcome these limitations, I introduce electric field tunable loading of plasmonic nanostructures and demonstrate wireless electric-field sensors for electrophysiology and flat optic modulators.

First, I introduce an ultrasensitive and extremely bright nanoscale electric-field probe overcoming the low photon count limitations of existing optical field reporters. I demonstrate that electrochromic loading of plasmonic nanoantenna allows us to realize optical field probes with $10 - 100$ million times larger cross sections than fluorescence molecules and $\sim$ 3000-fold enhanced sensitivities than conventional plasmonic nanoantennas. Using our nanoprobes, I realize optical detection of electric-field dynamics from diffraction limited spots and high-speed recordings with sub-millisecond temporal response times ($\sim$ 191 µs). Furthermore, I demonstrate label-free optical recording of electrogenic activity of cardiomyocyte cells with low-intensity light. Our nanoprobes offering high spatiotemporal resolution measurement capability opens the door to label-free electrophysiological studies with photons.

Finally, I introduce a subwavelength-thick ($<$ 250 nm) nano-electrochromic flat optic modulator that utilizes the electrochromic modulation mechanism in combination with highly dispersive Fano resonances in extraordinary light transmission (EOT) effect. We demonstrate electro-optic switching capability that can simultaneously deliver remarkably high modulation depth ($\sim$ 17.6 dB) and high speed ($\sim$ 500 µs, $\sim$ 2 kHz) switching capability beyond the video rates. The field-effect flat optic modulator shown here paves the way to the advancement of technologies based on electrochromic soft materials.

Acknowledgments

First and foremost, I would like to thank my advisor Professor Ahmet Ali Yanik, for his guidance, enthusiasm, and constant encouragement throughout the years of my doctoral study. From him, I learned not only the need for profound research but also the importance of looking at the bigger picture. His insights have greatly helped me in several crucial phases of this research. I would like to thank the members of my committee, Professor Holger Schmidt and Professor Marco Rolandi, for their review of this thesis. I would also like to thank all the colleagues from our UCSC NanoEngineering Research Group, in particular Dr. Xiangchao Zhu, Maverick McLanahan, and Neil Hardy, for breaking the ground with me on this project. And all my colleagues: Mustafa Mutlu (thank you for being a good friend of mine), Reefut Inum, Sierra Catelani, Sabrina Fong, and many undergraduates. Dr. Imran Hussain and Evan Peterson, both for technical discussions and all kinds of fun discussions. I am very grateful to my colleague, Neil Hardy, for proofreading my thesis.

I was blessed with a baby girl Alveera Ashfee Ahsan during my Ph.D. study, and I thank her for being my inspiration. She became one of the main sources after her birth, and I could recharge myself and work harder on my research. Additional co-authors also contributed to work in Chapter 2 (Xiangchao Zhu, Sabrina Fong, and Ahmet Ali Yanik), which was previously published (Nanophotonics. 9, 3805–3829 (2020)), Chapter 3 (Xiangchao Zhu, Uryan I. Can, Maverick L. McLanahan, Pinar Zorlutuna, and Ahmet Ali Yanik), which was previously publis

Chapter 1

Introduction

Plasmonics is a rapidly growing sub-field of modern optics, which deals with the manipulation of electromagnetic waves by coherent coupling of photons to free electron oscillations at the metal-dielectric interface [1–7]. Due to its ability to localize light at nanoscale volumes beyond the diffraction limit and the drastically enhanced light matter interactions, as a result, surface plasmonics has emerged as a fruitful field for technological advancements [3,6]. Over the last few decades, we have witnessed transformational advancements in a myriad of promising application areas (Figure 1.1), ranging from energy conversion to ultrasensitive biosensing [8–22]. In recent years, significant effort has been made to develop large-scale, and low-cost nanofabrication techniques [18, 23, 24], to transfer plasmonic technologies from research laboratories to industry [25–27].

Optical modes of resonant plasmonic nanostructures are classified into two distinct types: surface plasmon polaritons (SPPs) and localized surface plasmon polaritons (LSPs) [28]. SPPs are propagating bound oscillations of electrons and electromagnetic waves at a metal-dielectric interface(Figure 1.2a). LSPs are standing wave surface plasmons that are tightly confined to a subwavelength nanoparticle surface (Figure 1.2b). Surface plasmon resonance occurs when the frequency of incident photon resonates with the oscillation of the conduction electrons in the metal. Plasmonic excitations lead to nanoscale confinement of electromagnetic field near metallic surfaces, which is often referred as plasmonic "hot spots" (Figure 1.2c). The light intensity at these hot spots can be several orders of magnitude stronger than incident light, and thus offering a drastically enhanced interaction of light with matter [10, 13]. Therefore, despite having modest Q value $(10 - 100)$ [29, 30] they can outperform high Q ($10^5 - 10^6$) [30, 31]

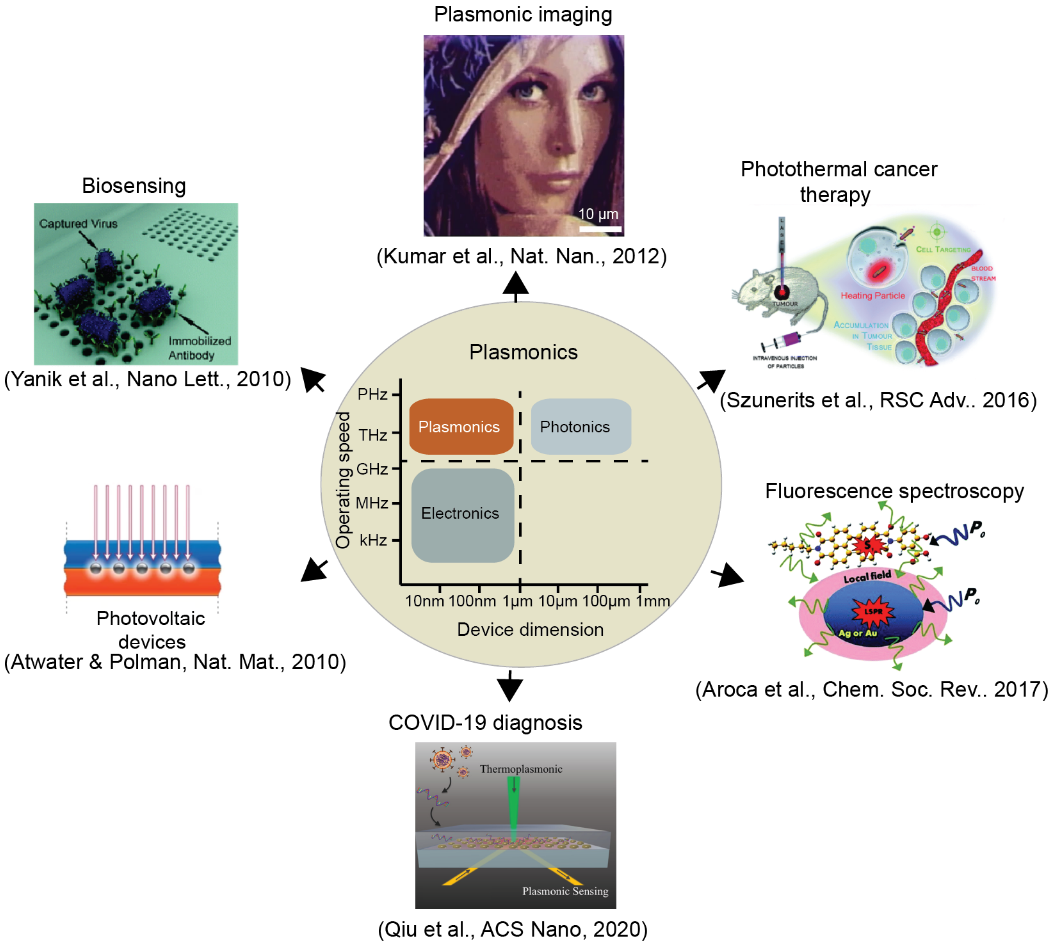

Figure 1.1: Plasmonics and its applications. In various fields of science and engineering, plasmonics has found a wide range of applications.

dielectric resonators, and are hence heavily used in biological and chemical sensing applications [16, 17, 32–49].

Conventionally, optical properties of plasmonic structures are predetermined by design and manufacturing processes, resulting in a fixed response for a given excitation—a significant impediment for many practical applications that requires tunability. Active control of plasmonic characteristics is needed for the advancement of plasmonic technologies such as modulators [50–53], and field-effect neurophotonics devices [54, 55]. Therefore, dynamically reconfigurable plasmonics, also known as “active plasmonics” [56, 57], has recently attracted significant interest [57, 58]. Since the term “active plasmonics” was introduced in 2004 [59],

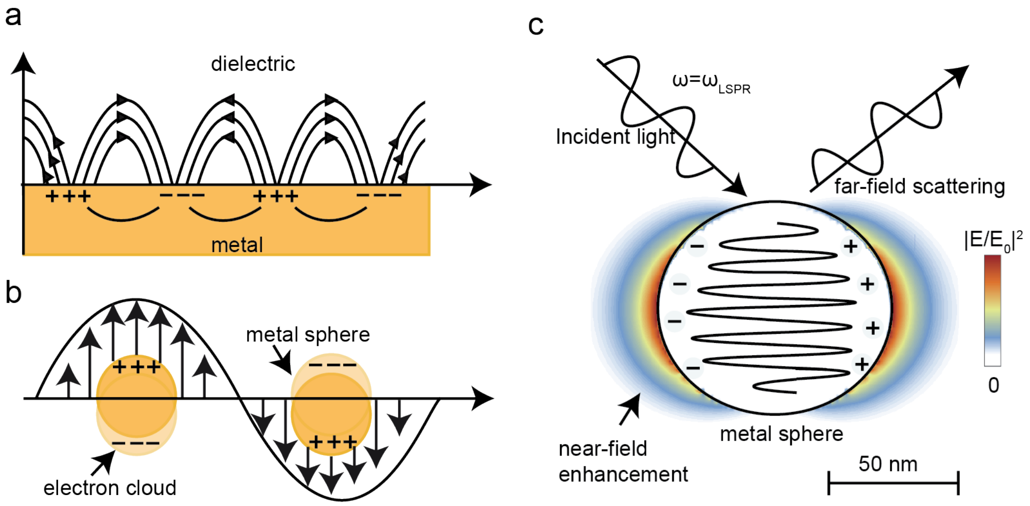

Figure 1.2: Schematics showing (a) a surface plasmon polariton (SPP) mode and (b) a localized surface plasmon (LSP) mode. (c)Near field enhancement $|E/E_o|^2$ along the metal (gold) sphere (diameter 100 nm). Finite difference time domain (FDTD) simulation shows that plasmonic excitation leads to strong light confinement.

this new field of research has grown at a phenomenal rate, as evidenced by the rapidly increasing number of annual citations to active plasmonics-related scientific articles (Figure 1.3). Progress in this field can facilitate the development of novel active plasmonic devices with unprecedented photon management capabilities, leading to a wide range of exciting new practical applications [43, 54, 60].

Recent experimental developments have suggested several alternative approaches for active control of plasmonic resonances, exploiting electrical [61–63], chemical [64], mechanical [65], thermal [66], and optical [67] methods. Recently, there has been a concerted effort focused on developing active plasmonic devices that exploit field-effect phenomena for precise controlling of the plasmonic characteristics [54, 55, 60, 62]. Electrical active control methods achieve tunability by modulating the free carrier density of the constituent plasmonic materials, such as gold (Au), silver (Ag), etc. [68–70]. Free carrier modulation of metals determines the plasma frequency ω_p, which is given by

$$\omega_p = \left(\frac{Ne^2}{m_e\varepsilon_0}\right)^{1/2} \tag{1.1}$$

Here, N is the electron density in the metal, e is the elementary charge, m_e is the effective mass

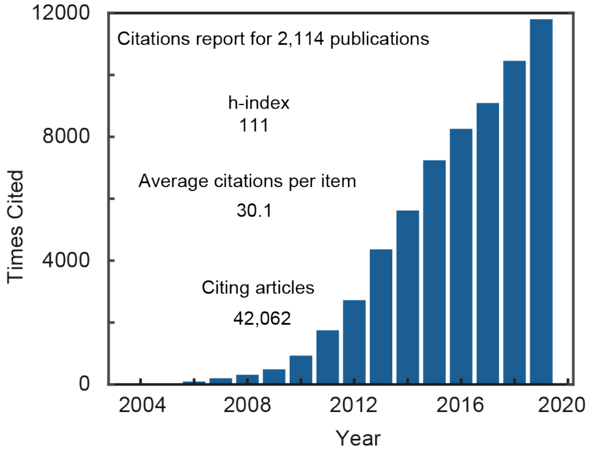

Figure 1.3: The total number of citations to active-plasmonics literature from 2004 to 2019 illustrates remarkable growth in this field. Adapted from ref. [58].

of the electron, and ε_0 is the vacuum permittivity. As illustrated in Figure 1.4, when an external field is applied, plasmonic surface experiences modulation of the electron density, hence the plasma frequency. This modulation results in a blueshifting (redshifting) of the plasmonic resonance with the increasing (decreasing) electron density [71]

$$\lambda_{res} = \frac{2\pi c(\varepsilon_\infty + 2\varepsilon_m)^{1/2}}{\omega_p} \tag{1.2}$$

Here, ε_∞ is the high frequency dielectric constant, c is the velocity of the light, and ε_m is the dielectric function of the electrolyte ($\varepsilon_m = \sqrt{n}$; n is the refractive index of the electrolyte solution). However, electron densities in plasmonic metals such as gold (Au) and silver (Ag) are high ($\sim 10^{23} cm^{-3}$) and cannot be readily modulated using external field [57, 72]. Therefore, a more effective modulation approach is needed for active plasmonics.

In this thesis work, I introduce electric field tunable loading of the plasmonic nanostructure with electrochromic polymers to realize the active plasmonic systems with high electric field sensitivity. I will demonstrate plasmonic systems, such as plasmonic nanoantenna array (PNA) and plasmonic nanohole array (NHA), that are loaded with electrochromic polymer material as a field tunable dielectric load to plasmonic nanoresonators [54]. In reverse operation mode, I show how an electrochromically loaded plasmonic (electro-plasmonic) nanostructure can act as a reporter of local electric-field dynamics to the far-field. I demonstrate drastically (3×10^3 times) enhanced field sensitivities with respect to previous studies focused on bare

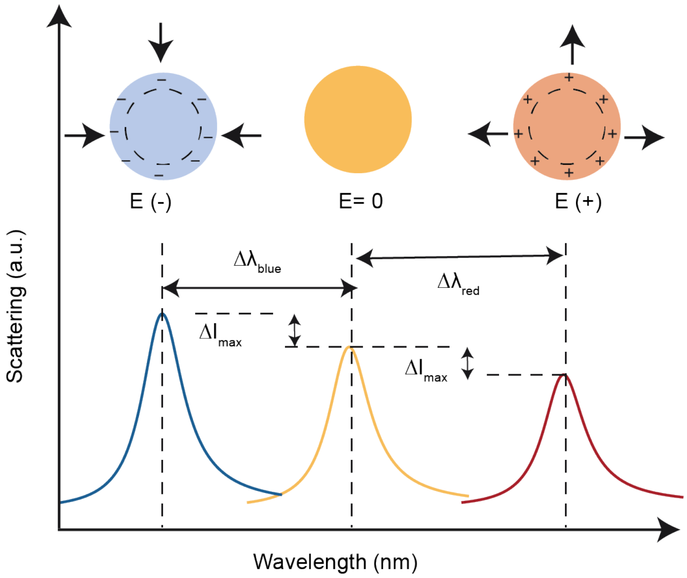

Figure 1.4: Schematic depiction of spectral characteristics obtained due to the modulation of electron density of the plasmonic metal sphere. (Middle; yellow color) Metal sphere without any external electric field. (Left, blue color) An increase in electron density causes a blueshift with an increase of scattering intensity. The electric field direction is toward the metal sphere. (Right, red color) A decrease in electron density causes a redshift with a decrease of scattering intensity. The electric field direction is away from the metal sphere.

plasmonic resonators by performing electro-optic measurements from diffraction-limited volumes.

1.1 Thesis Contributions

Since Hermann von Helmholtz's first measurement of nerve impulses in 1849, electrophysiologists have been developing tools to gain simultaneous access to the activity of single cells in large networks. Electrical technologies such as microelectrode arrays (MEAs) have made significant progress towards this goal. However, fundamental limitations associated with on-chip signal conditioning (e.g., front-end amplifiers, right underneath, or nearby, the electrodes) requirements and tighter upper limits for the low noise transfer of spiking cell information over a multiplexed wire remains to be addressed. Probing membrane potential with optical voltage reporters is a promising alternative technique that can potentially open the door to unprecedented spatiotemporal resolution measurements by harnessing photons [73]. Optical electrophysiology technologies such as genetically encoded voltage indicators (GEVIs) have recently attracted considerable interest that transforms membrane potential fluctuations into changes in light intensity. GEVIs are based on fluorescent protein fusions to a voltage-sensing domain, provide a strong optical response to membrane potential changes. However, due to the small cross-sections of molecules (10^{-2} nm^2) [74] and quantum yields ($QY \sim 10^{-4} - 10^{-3}$) [75], fluorescence-based bioelectrical measurements suffer from poor signal-to-noise ratio limitations due to low photon count signals.

Shot noise, which reflects the quantal nature of light and the probabilistic nature of photon detection, is the dominant noise source in low-photon count measurements [73]. We can consider two simple scenarios to demonstrate the effect of shot noise on signal detection. In the first scenario, the detector registers 10^6 photons per second, meaning that 1000 photons are recorded in each bin an average assuming 1 ms integration time. So, in the presence of an action potential(AP), a voltage reporter that experiences increased fluorescence signal by 10 percent will lead to 100 extra photons (signal) on average in each bin. In the second scenario, the same detector registers 10^4 photons per second. Assuming identical excitation and detection conditions and voltage reporters, each bin will contain one photon for the signal. Because shot noise is proportional to the square root of the number of available photons detected during an experiment [76], the second scenario will be shot noise limited. As a result, even for GEVIs that have excellent voltage sensitivity (100%), real-time measurement of electrophysiological signals is not possible with them. Using higher intensity light sources is not likely to solve this problem, since this can lead to photobleaching and phototoxicity. More importantly, genetic mutations are needed to incorporate GEVI into the cell's membrane, preventing its potential utility in humans. Most recently, field-sensitive quantum dots (QDs) has emerged as extracellular alternatives to GEVI, circumventing the need for genetic mutations. QD field probes have relatively larger much larger cross-sections than GEVI. However, QDs use quantum confined stark effect (QCSE) for electric-field detection, a relatively weak effect. Hence, QD field-probes suffer from shot-noise limitation much like GEVIs, but for a different reason.

In this thesis, I introduce a new class of extremely bright label-free extracellular optical field probes that overcome the photon count and field sensitivity limitations of existing optical voltage reporters. I demonstrate label-free probing of local electric fields and electrophysiological signals using loaded plasmonic nanoresonators with high temporal (sub-millisecond) and spatial (diffraction-limited) resolutions. I use electrochromic loading of plasmonic resonators, which causes the wavelength and intensity of their far-field plasmonic resonance to change in response to changes in membrane potential during an action potential (AP).

In addition, this thesis focuses on the development of ultra-sensitive and high speed "flat optical" modulators. Optical instruments have remained bulky and expensive since the days of Galileo and Van Leeuwenhoek. They were made by refining mechanical parts, usually made of glass, that manipulate light to sense, measure, and project. Recently, "flat optics," has emerged as an alternative to traditional approaches. Recent studies have shown that planar nanostructures can perform similar static optical functions to bulky components [77, 78]

Most recently, active flat-optical components that incorporate electrochromic materials (electro-plasmonics) have emerged. One important application in this field is developing a fast, and high-modulation depth flat optical modulator for electronic display [54, 67, 79–82]. However, electro-plasmonic modulation, with an ultra-high contrast ratio typically required for practical purposes, has not yet been demonstrated. Previous electro-plasmonic approaches exploit the change in the imaginary part of the effective refractive index, which is difficult to modulate significantly and is limited by the representative electrochromic material's inherent characteristics. In contrast to the traditional electro-plasmonic modulator, I use the real part of the refractive index to tune the spectrally sharp Fano resonant extraordinary light transmission (EOT) spectrum of the plasmonic nanohole array. In addition, I employ novel spectral engineering of the spectrally sharp Fano resonant extraordinary light transmission (EOT) spectrum of the plasmonic nanohole array. I show an unprecedented 17.6 dB modulation depth with a sub-millisecond switching rate.

1.2 Thesis Outline

A brief description of the content of the five chapters of this thesis is as follows:

Chapter 1: Introduction – Problem Statement and Research Motivation

In this chapter, I present a brief background on plasmonics and active plasmonics. I present the bottlenecks of the existing electrically tunable active plasmonic devices. I introduce an alternative mechanism for the electrical tuning of plasmonic resonances.

Chapter 2: Active Plasmonic Antenna: An Emerging Toolbox from Photonics to Neuroscience

In this chapter, I discuss the latest and most important findings in active plasmonic and provide an overview of active plasmonic nanoantenna (PNA) devices. First, I summarize the basic principles underlying PNAs and their general properties. Subsequently, I discuss a powerful and universal inverse design approach for the rapid and efficient engineering of PNAs with high quality-factor and narrow resonance linewidth spectral characteristics. I then emphasize two advanced nanofabrication techniques that enable high-throughput, large-scale manufacturing of PNAs with remarkable structural uniformity and homogeneity at a wafer scale. Later, I describe an elegant optical nanocircuit framework that helps us to capture the sophisticated optical response of PNAs and provide guidance for the rational design of active PNAs. Then, I use the optical nanocircuit theory to classify the recently developed strategies for active tuning of passive PNAs into four distinct categories. Finally, I discuss potential applications of active PNAs for electrophysiological recordings.

Chapter 3: Electro-plasmonic Nanoantennas for All-optical Electrophysiological Recordings

In this chapter, I present a new class of extremely bright non-fluorescent optical voltage sensors that can sensitively detect local electric-field dynamics. I demonstrate 3.25×10^3 fold enhanced electric field sensitivities over traditional plasmonic nanoantennas. I show that our electrochromically loaded plasmonic (electro-plasmonic) nanoantennas offer high signal-to-shot-noise ratio (SSNR $50-220$) measurement from single nanoscale resonators. I also demonstrate label-free and non-invasive in vitro measurement of the electrogenic activity of cardiac muscle cells(CM) through our in vitro measurements using low-intensity light, which is two to three orders of magnitude lower than the typical light intensities used for fluorescent voltage probes.

Chapter 4: Nano-Electrochromic Flat Optics: A High-Performance Electrochemical Plasmonic Fano Switch

In this chapter, I develop a novel hybrid flat electro-optic modulator merging plasmonic and electrochromism to overcome the low modulation depth of plasmonic modulators. I exploit the highly dispersive and steep spectral profiles of plasmonic Fano resonances. I experimentally demonstrate a highly efficient active tuning scheme of Fano resonance in an electro-plasmonic structure comprising 2D plasmonic nanohole arrays coupled to a thin electrochromic polymer load. Our subwavelength-thick device offers a highly dispersive Fano resonance that can be spectrally tuned over a wide spectral range using a small modulation voltage (~ 1.5 V) that is compatible with CMOS electronics. Our plasmon-enhanced electro-optic modulator providing sub-millisecond switching times and remarkably high modulation depth (17.6 dB) paves the way for developing electro-optic modulators for ultra-thin display technologies.

Chapter 5: Conclusion – Major Contributions and Future Work

This chapter summarizes the major contributions of this dissertation and future directions to extend this work.

Chapter 2

Active Plasmonic Nanoantenna

Concepts adapted from radio frequency (RF) devices have brought forth subwavelength scale optical nanoantenna, enabling light localization below the diffraction limit. Beyond enhanced light-matter interactions, plasmonic nanoantennas conjugated with active materials offer strong and tunable coupling between localized electric/chemical/mechanical phenomena and far-field radiation. During the last two decades, great strides have been made in the development of active plasmonic nanoantenna systems with unconventional and versatile optical functionalities that can be engineered with remarkable flexibility. This chapter reviews the fundamental characteristics of active plasmonic nanoantennas and recent advances in this burgeoning and challenging nano-optics sub-field. The underlying physical mechanisms underpinning dynamic reconfigurability and several promising approaches to the development of active plasmonic nanoantennas with novel characteristics are discussed. This chapter is a modified version of following publication:

A. Habib, X. Zhu, S. Fong, and A. A. Yanik, "Active plasmonic nanoantenna: an emerging toolbox from photonics to neuroscience:," Nanophotonics, vol. 9, no. 12, pp. 3805–3829, 2020. `https://doi.org/10.1515/nanoph-2020-0275`

2.1 Metallic plasmonic nanoantennas

Metallic PNAs are one of the most commonly used structures in the nanophotonic toolbox due to their ease of engineering [83–85]. PNAs allow light manipulation at subwavelength scales and enable enhanced electron-photon coupling [28]. Inspiration for these optical antennas can be traced back to their radio-wave and microwave counterparts (Figure 2.1a). Electrical antennas driven by high-frequency voltage sources induce oscillations of currents (oscillating polarization), leading to radio- and microwave radiation. Analogously, PNAs driven by high-frequency "optical sources" induce oscillations of "optical current" in the nanostructures, yielding electromagnetic radiation spanning from ultraviolet to visible and near-infrared regime [84–87]. Because the characteristic dimension of an antenna is typically on the order of the electromagnetic radiation wavelength, PNAs are basically a nanoscale version of its much larger ubiquitous radio frequency (RF) counterpart. Nevertheless, compared to the RF analogue, PNAs operate with significantly deviated physical principles (Figure 2.1b) [84, 88]. Nanoscale optical antennas offer extremely efficient bilateral energy conversion between localized electromagnetic fields and far-field optical radiation [83–85]. The fundamental reason behind this unique feature is associated with the strong coupling of coherent oscillations of free electrons in metals (surface plasmons) to the incident light. At optical resonance, PNAs allow the electromagnetic field to be funneled from continuum to ultra-small, nanometer-scale volumes through excitations of LSPs. LSPs confine the incident field to the antenna structure's close vicinity at dimensions smaller than the operating wavelength, leading to intense light focusing beyond the diffraction limit. A variety of different PNA shapes and configurations are demonstrated to support LSPRs, including triangle [72,89,90] , star-like geometry [91], core-shell structure [84,92], Yagi-Uda antenna [93,94], and V-antennas [95,96]. By virtue of coherent plasmonic excitations, optically resonant nanoantenna can dramatically boost light-matter interactions by several orders of magnitude and strongly enhance local field intensities. Such gigantic field concentration and amplification (hotspots) result in a remarkably efficient light collection from a plasmonic cross-section that can be significantly larger than the physical cross-section of PNAs [1, 97] (Figure 2.1c).

PNAs have become an invaluable tool in a plethora of cutting-edge applications due to their drastically enhanced optical scattering and absorption cross sections at resonance. These include single molecule super-resolution microscopy [89, 98], high-efficiency photovoltaics [9, 11], ultrafast quantum information processing [99, 100], ultrasensitive biosensing [16, 19], integrated optical nanocircuitry [88], and augmented reality [101, 102]. The latest advances in precise nanoscale fabrication and nanophotonic characterization techniques as well as powerful electromagnetic simulation methods have enabled scientists and engineers to understand

and harness plasmon excitations in metallic PNAs [11,83,85,103]. By employing these well-established tool sets, sophisticated devices can be readily designed with virtually any desired functionality through rigorous parametric optimization processes [29, 104]. For example, a well-engineered array of PNAs can support long-lived, and high quality (Q)-factor optical resonances and high field enhancements over a broad-spectral range down to the deep ultraviolet (UV) regime. One fascinating advantage benefiting from these nanostructures is the subwavelength interfacing of optics and electronics with superior speed and bandwidth over state-of-the-art optoelectronic systems [85,90,105].

2.1.1 High Q-factor broadband plasmonic nanoantennas

Optical characteristics of PNA critically depend on the imaginary and real components of the metal's dielectric constant, an intrinsic property of the selected element (Figure 2.1d). Over the past decades, various materials have been explored in detail [85,110–115]. To date, gold (Au), silver (Ag), and aluminum (Al) remain the most commonly used metals because of their high free-electron density and low intrinsic losses [85]. However, to fully exploit the strong light-matter interaction for practical applications, considerable efforts have yet to be made to control plasmon damping processes in realization of high-quality factor (Q-factor) plasmon resonances [19,29,104,116,117]. Metallic resonators, such as PNAs, yield broad linewidth resonances due to rapid dephasing of coherent oscillations within 2–10 fs [116, 118]. Short plasmon lifetime of LSPRs arises from plasmon damping through two dissipation channels: radiative decay (photon emission) and nonradiative coupling (heat generation) [104, 116] (Figure 2.1e). Radiatively lost electromagnetic energy is reversible and can be harnessed to excite neighboring plasmonic resonators [19, 119]. Non-radiative decay, however, leads to irreversible electromagnetic energy loss [97, 120, 121]. The strength of nonradiative decay losses is controlled by direct interband transition, phonon-assisted intraband transition and Landau damping rates [104, 122]. At high optical frequencies, interband transitions associated with the intrinsic properties of metals become particularly strong, precluding access to much of the UV and visible (vis) spectrum. Rapid damping of plasmon energy severely limits the buildup of optical near-field intensities, resulting in weaker light-matter interactions. Therefore, it is of crucial importance to delay the dephasing of plasmonic excitation in order to realize strong electron-photon coupling and obtain high Q-factor LSPRs. Controlling radiative and non-radiative losses

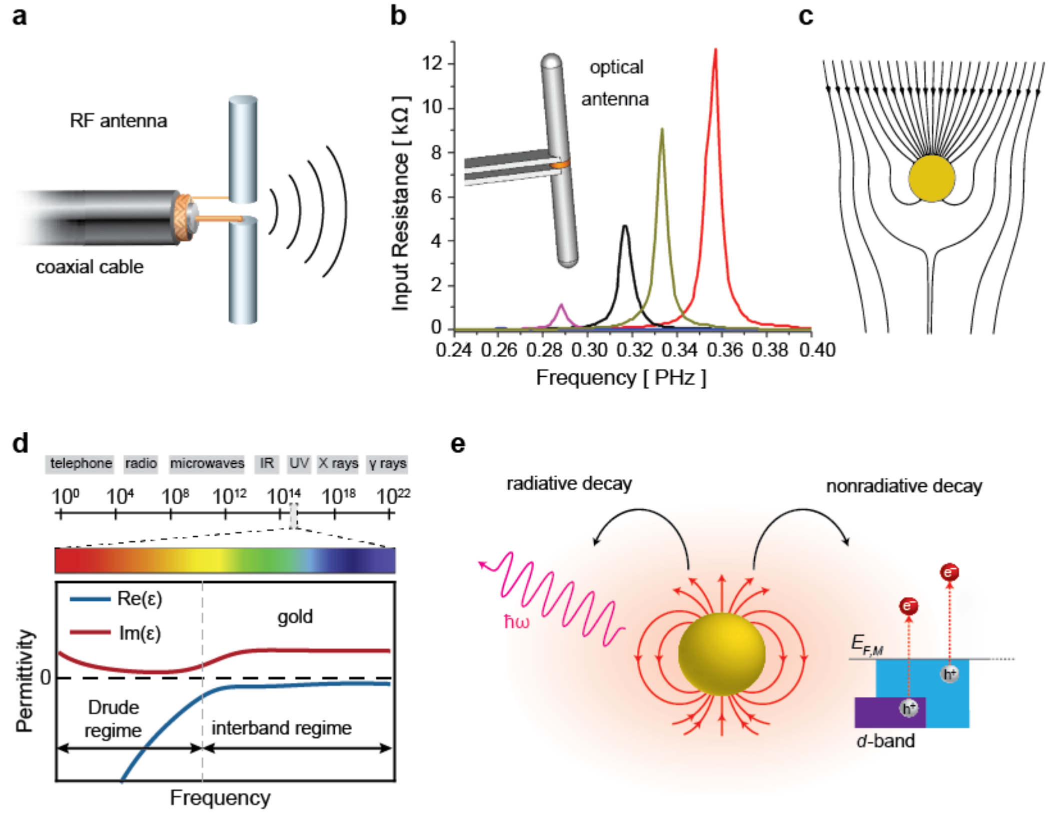

Figure 2.1: Subwavelength PNAs: (a) A conventional dipolar antenna operating in the RF regime. Connecting the antenna to an electrical coaxial wire enables energy conversion between local RF sources and far-field electromagnetic radiation. Adapted from Ref. [106] with permission from American Association for the Advancement of Science; (b) PNAs operating in the optical regime. Adapted from Ref. [107] with permission from the American Physical Society; (c) Electromagnetic energy is strongly focused through the optically resonant metal PNA when the LSPR condition is met. Adapted from Ref. [98] with permission from Springer Nature; (d) Dielectric function (experimental data by Johnson and Christy [108]) of gold at optical frequencies; (e) A schematic illustration of surface plasmon decay mechanisms: the plasmon can either decay radiatively into re-emitted photons (left), or non-radiatively decay into energetic electrons (right). Adapted from Ref. [109] with permission from Springer Nature.

in a metallic resonator, on the other hand, is a major fundamental and practical challenge.

Recently, Zhu et al. reported an elegant and universal approach enabling rapid and efficient inverse engineering of remarkably narrow linewidth and high Q-factor PNAs, independently from the metals and dielectric environment surrounding the antennas [29] (Figure 2.2). They showed that long-lived plasmonic excitations can be realized over the entire visible spec-

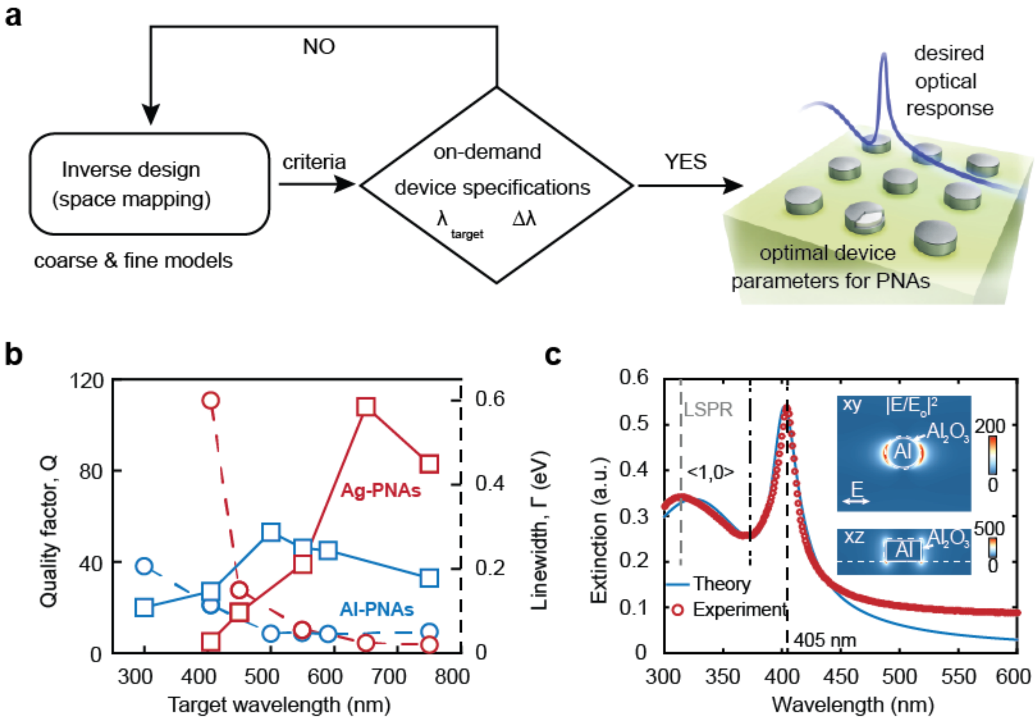

Figure 2.2: High Q-factor Al-PNAs over a broad spectral window: (a) Space mapping algorithm enabling inverse design of high Q-factor (narrow resonance linewidth) PNAs at a desired wavelength; (b) Optical characteristics of coupled Al-PNAs (blue color) and Ag-PNAs (red color) that are designed using this space mapping algorithm are compared over a broad spectral range; (c) Experimentally measured extinction spectrum of optimized Al-PNAs (red circles) demonstrates strong Fano-like resonance behavior (blue curve). Inset shows the cross-sectional near-field intensity profiles of the Al-PNAs; (c) Adapted from Ref. [29] with permission from American Chemical Society.

trum and deep into the ultraviolet regime by quenching radiative losses using far-field coherent interactions in Al-nanoantennas arrays and harnessing the distinctively favorable dielectric characteristics of the Drude-like Al. To achieve this, Zhu et al. introduced a powerful and versatile inverse-design technique offering a general and efficient way to optimize any PNA arrays fabricated on refractive index mismatched super-/substrates (Figure 2.2a). Traditional trial-and-error based design approaches require computationally expensive, central processing unit (CPU) and time-intensive three-dimensional rigorous electromagnetic simulations of tens to hundreds of candidate structure [123, 124]. In stark contrast, space mapping based inverse-design method enables ultrafast and accurate retrieval of the fittest sets of structural parameters, which yield the on-demand PNA characteristics with a minimal number of high-fidelity and computationally expensive simulations [29]. Using this novel design approach, Zhu et al. demonstrated remarkably high Q-factor ($27 \leq Q \leq 53$) Al-nanoantenna arrays over the entire visible spectrum, outperforming even similarly optimized Ag-nanoantenna arrays in green-blue-violet wavelengths ($\leq$ 550 nm) and near-UV regime (300 nm) (Figure 2.2b). Unprecedently, drastically narrow linewidth (15 nm) and record high Q-factor (Q $\sim$ 27) Al-PNAs have been experimentally demonstrated (Figure 2.2c).

2.1.2 High-throughput and scalable nanofabrication

Real-world adaptation of nanoscale technologies critically depends on development of high throughput and high yield nanofabrication techniques, offering precise structural uniformity at nanoscale. The last few decades, we have witnessed exciting progress in development of scalable nanofabrication techniques including top-down electron-beam [125], ion-beam [126], nanostencil [24, 127], nanosphere [128, 129] lithography and bottom-up self-assembly schemes [91, 92, 130–134]. However, major hurdles remain in realization of large-scale low-cost manufacturing methods of PNAs with minimal structural inhomogeneities and nonuniformities (polydispersity). As LSPR energy strongly depends on the size and material of PNAs, poorly controlled nano-features give rise to unpredictable LSPR behavior and unfavorable heterogeneous broadening of resonance linewidths, especially for small size nanoantennas [29, 104]. In particular, fabrication of plasmonic nanostructures often need metal lift-off processes, which leads to significant variations in nanoscale features. Recently, Zhu et al. demonstrated an effective strategy for tackling these challenges by employing a high-throughput wafer-scale lift-off free fabrication approach based on UV-interference lithography and reactive ion etching [29](Figure 2.3a). They demonstrated low-cost large-area nanofabrication of Al-nanodisk arrays fabricated over 8 inch fused-silica wafers with excellent structural variations with sub-30 nm feature sizes (Figure 2.3b-c). Employing this novel nanofabrication technique, we recently demonstrated remarkably high Q-factor Al-nanoantenna arrays [29].

Nanostencil lithography (NSL), an alternative lift-off free fabrication technique, offers high-resolution nanofabrication capability on unconventional and flexible substrates [24, 127]. A major drawback of this technique, however, was the difficulty of fabricating nanostencil masks using electron-beam lithography. Recently, Zhu et al. developed a deep-UV (DUV)

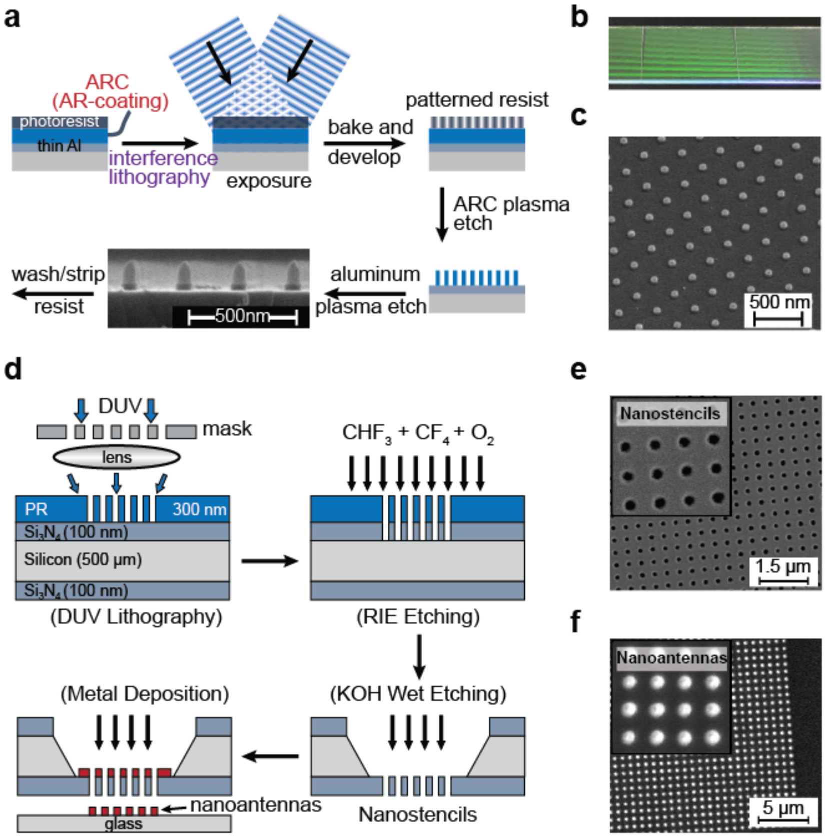

Figure 2.3: High-throughput and wafer-scale fabrication of PNA: (a) Schematic of the deep-UV (DUV) nanofabrication approach enabling lift-off free patterning of plasmonic nanostructures with exceptional uniformity; (b) A (1 inch × 3 inch) glass slide with millions of Al-PNA structures on it is shown; (c) Scanning electron microscope (SEM) image of a Al-PNA fabricated on glass substrate using this technique. (a) and (b) adapted from Ref. [29] with permission from American Chemical Society; (d) Schematic illustration of the DUV-based nanostencil patterning technique enabling fabrication of PNA in a lift-off free manner. High-quality and large area nanostencils, free-standing silicon nitride (Si_3N_4) thin films with an array of open-ended nanoapertures, are first fabricated using the DUV nanopatterning; (e) SEM image of a nanostencil with a periodic array of circular nanoapertures arranged in a square lattice. The nanohole diameter and array periodicity are 130 nm and 380 nm, respectively; (f) SEM image of an Au-PNA array fabricated on a glass substrate using this nanostencil and mask deposition process. The diameter and height of the resulting nanodisk antennas are 140 nm and 120 nm, respectively.

lithographic nanofabrication technique enabling high-throughput wafer-scale manufacturing of large area stencils using suspended silicon nitride (Si_3N_4) membranes [135]. Using this technique, they demonstrated 4 inch wafer stencils housing 200 million nanoapertures with remarkably uniform nanoscale features. We used DUV-based NSL to pattern PNAs, i.e., nanodisk arrays, on a non-conductive glass substrate (Figure 2.3d). To do this, we placed nanostencils with open-ended nanoapertures in intimate contact with the substrate to ensure perfect transfer of the nanoantenna pattern with minimal shadowing effect (Figure 2.3e). Using a single directional metal deposition step, we demonstrated remarkably precise and reliable patterning of 200 million Au-nanodisk antenna on glass substrates (Figure 2.3f). Beyond this particular example shown here, this DUV nanofabrication scheme allows fabrication of high-density PNAs on unconventional substrates, including rigid, flexible, stretchable, and biocompatible materials [24, 127].

2.1.3 Lumped optical nanocircuit theory

Adaptation of antenna concepts from the RF communications has revolutionized our ability to manipulate light at subwavelength scale, opening up the possibility of optical information processing at the nanoscale [88, 136, 137]. Likewise, concepts of lumped circuit elements and RF design is providing guidelines for future innovations and new technological breakthroughs for nanoscale optics. Lumped circuit elements allows simplification of the analysis of complex circuits and enable conceptual understanding of effective modularization of each circuit element [138]. In this respect, a comprehensive understanding of the internal mechanism of each circuit element is not needed when designing a circuit; only the relation between the voltage across each element and the current flowing through the element is sufficient. Therefore, by hiding much of the internal operational complexity within an individual device design, RF electronic circuits can be readily constructed with desired functionalities at the system level and on a very large scale [13, 86, 136]. However, simple scaling of RF design concepts to optical wavelengths is not feasible because at infrared (IR) and optical frequencies, metals have strong Drude losses and do not exhibit conductivity in the conventional sense due to the large negative real part of their permittivities [136]. Therefore, a modified quantitative design approach, an analogue of RF circuits, is needed.

Alù and Engheta pioneered a general theoretical framework for PNA-based optical nanocircuits using RF design concepts [136, 137] (Figure 2.4a). In their optical nanocircuit approach, metals ($Re[\varepsilon] < 0$), insulators (the surrounding dielectric, $Re[\varepsilon] > 0$), and energy dissipation (heating) are modeled as nanoscale capacitors, inductors, and resistors, respectively

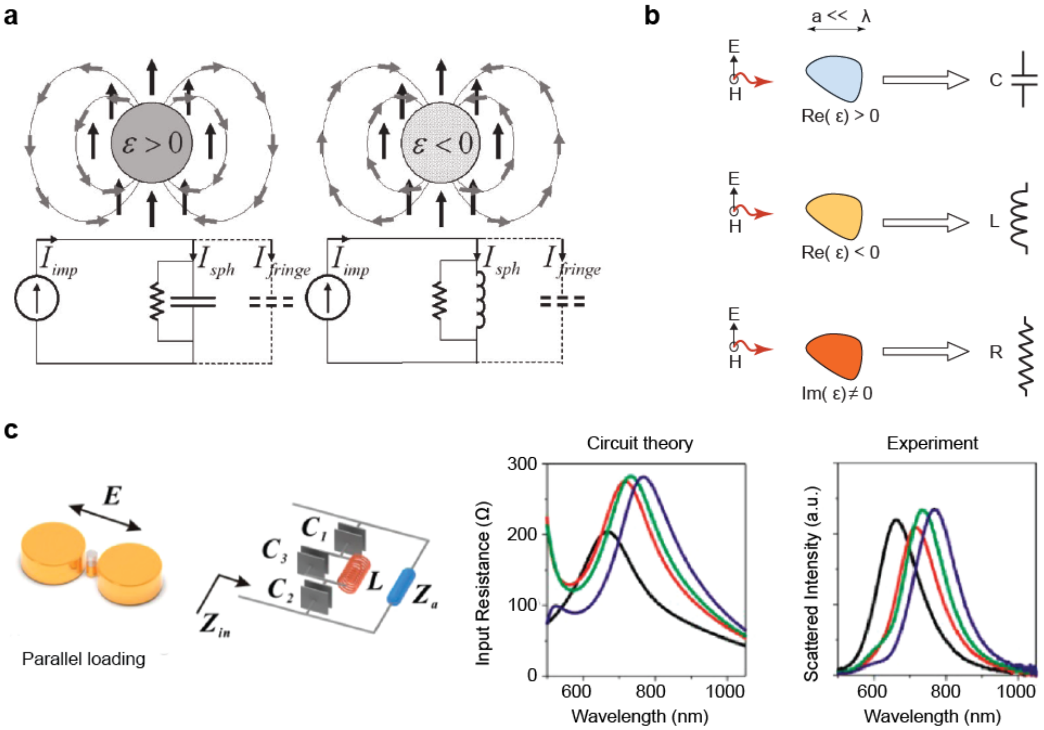

Figure 2.4: Optical nanocircuit representation of PNAs: (a) The concept of optical nanocircuit theory in the optical domain. Adapted from Ref. [137] with permission from American Physical Society; (b) A subwavelength nanoantenna, when illuminated by a monochromatic light, behaves as three lumped optical circuit element: nanocapacitor (top), nanoinductor (middle) and nanoresistor (bottom). Adapted from Ref. [136] with permission from American Association for the Advancement of Science; (c) Schematic showing the equivalent optical circuit model of a loaded PNA (first and second panels). Far-field scattering spectrum of the PNA obtained with the optical nanocircuit model (third panel) is in remarkable agreement with experiment (fourth panel). Adapted from Ref. [139] with permission from American Chemical Society.

(Figure 2.4b). These three basic nanocircuit elements operating at IR and optical frequencies form the building blocks and modules for the design of “metatronic” circuits of arbitrary complexity via LSPs at the deep subwavelength scale. In their follow-up work studies, Alù and Engheta further developed the concepts of optical input impedance, optical radiation resistance, loading, and impedance matching in the optical frequency regime [106, 140]. By solving Maxwell’s equations and following the Kirchhoff’s current law, the electric fields and “flowing optical currents” can be tightly linked to the optical impedances of lumped nanocircuit elements in the same way one would model the electric current flowing in RF lumped circuit elements.

Based on Alù and Engheta's groundbreaking work, a great deal of effort has been made by many other research groups [54, 106, 139, 141–150], using these concepts in designing novel uses of plasmonic devices with functionalities merging electronic/chemical/mechanical phenomena with optics at nanoscale. Based on lumped optical nanocircuit theory, researchers demonstrated design, optimization, and analysis of novel practical PNA-based devices. Researchers are now capable of realizing plasmonic nano-optic devices that work seamlessly in the optical domain with desired optical performance through the optimization of lumped circuit elements [54, 106, 139]. One of the most notable examples is the impedance-matched optical dimer nanoantennas designed using fully three-dimensional (3D) lumped nanocircuit models [139] (Figure 2.4c). In this work, Liu et al. used the lumped circuit elements to realize accurate control and tuning of the optical response of the PNAs with great flexibility, in a similar way to turning the frequency-tuning knob of a radio [139] . The authors demonstrated a nanocircuit paradigm to construct PNA-based optical nanofilters with various topologies, opening the door to the development of integrated optical circuit for applications in data storage, wireless optical links, and related areas.

2.2 Reconfigurable plasmonic nanoantenna

Plasmonic resonance characteristics of passive PNAs are set in stone during the design/fabrication; and can only be altered with permanent morphological changes [151]. The need for reconfigurability in plasmonic response has spurred broad research activities. In the past two decades, a steady and rapid evolution from passive PNAs to active PNAs with optical characteristics controlled by nanoscale physical phenomena has occurred. A concerted, highly interdisciplinary effort has been devoted to the development of active systems in realization of post-fabrication dynamic reconfigurability in a fully reversible and repeatable, fast, and ideally programmable manner. Until now, a variety of schemes have been proposed and developed in pursuit of in situ active control by electrical [61–63], chemical [64, 152–154], optical [67], thermal [66], or mechanical [65, 155, 156] means. A key aspect of active PNAs is the scalability and reconfigurability of their optical properties through accurate control over their structural dimensions, materials, surrounding media and near-field coupling between individual components in the case of multielement arrangements. From a practical perspective, active PNAs with tunable resonances promise to enable critical optical functions for ultrabroadband

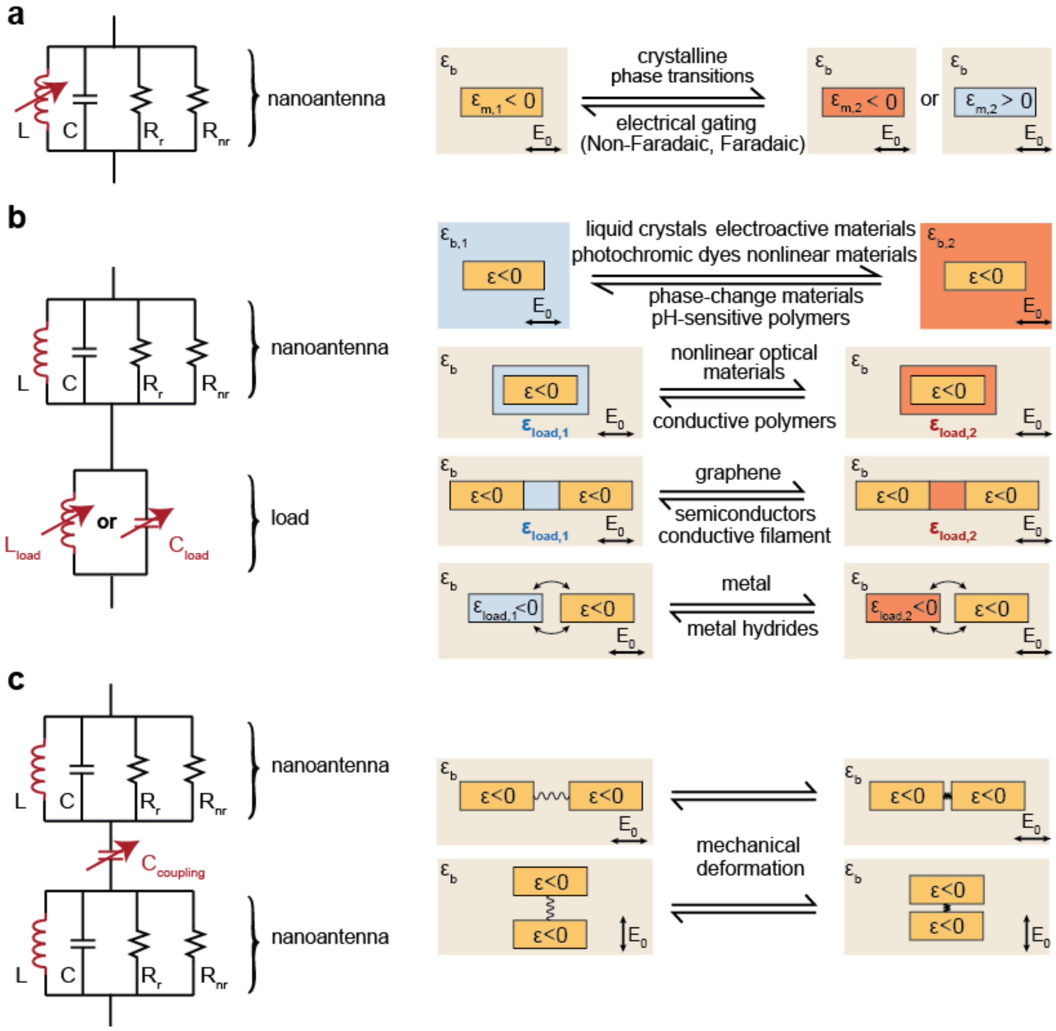

Figure 2.5: Mechanisms employed for active PNAs are summarized using lumped optical nanocircuit elements. (a) Modulations in the optical characteristics of the PNA metal are captured using tunable nanoinductors; (b) Modulation of PNA characteristics through the coupled dielectric medium is incorporated using a tunable load consisting of nanocapacitors or nanoinductors; (c) Modulation of the near field coupling between PNA elements is represented by tunable nanocapacitors. (a)-(c) The left panel shows the lumped optical nanocircuit representation of active PNAs for various tuning mechanisms. The right panel shows the schematic of reversible dynamic transition of PNAs by various external stimuli. r, radiative; nr, nonradiative.

sensors [46], tunable flat-lenses [157], holograms [158], dynamic switches [159], interferometry photonic platforms [160], neural activity tracking [55, 161], and information encryption [162]. We harness lumped optical nanocircuit theory to categorize current active PNA systems and develop an in-depth systematic understanding of the physical mechanisms behind most of these active plasmonic devices. In the following sections, we show that there are three distinct routes that lead to dynamic reconfigurability for PNAs (Figure 2.5). The first is based on direct modulation of the metal dielectric properties, which is effectively equivalent to tuning of the nanoantenna inductance (Figure 2.5a). The second is achieved by loading PNAs with active materials, which are represented by antenna-loaded nanocircuit elements that consist of either a tunable nanoinductor or nanocapacitor (Figure 2.5b). The third approach relies on modulation of the near-field coupling between adjacent nanoantenna elements in a multielement PNA arrangement; the variations in the coupling strength can be described using a tunable nanocapacitor that bridges different nanocircuits representing each nanoantenna element (Figure 2.5c). Table 2.1 shows the the strengths and limitations of these approaches.

2.3 Modulation through metallic properties

The first approach is through active tuning of PNA's inductance (Figure 2.5a). This can be achieved by direct modulation of free carrier densities and dielectric functions of the conductive metal nanostructures by means of crystalline phase transitions or electrical gating. The frequency dependent permittivity of metals can be described by the Drude model [28]

$$\varepsilon_{metal}(\omega) = \varepsilon_r(\omega) + i\varepsilon_i(\omega) = \varepsilon_\infty - \frac{\omega_p^2}{\omega^2 + i\omega\Gamma} + \varepsilon_{inter}(\omega), \quad \omega_p = \sqrt{\frac{n_e e^2}{m^* \varepsilon_0}} \tag{2.1}$$

where ε_r and ε_i are the real and imaginary parts of the dielectric function, respectively, ε_∞ is the high-frequency-limit dielectric constant, ω is the frequency of light, Γ is the damping frequency, $\varepsilon_{\text{int}\,er}$ represents the contribution from interband transitions, and ω_p is the plasma frequency. The magnitude of plasma frequency depends on carrier density n_e, the electron charge e , and its effective mass m^* . In the quasi-static regime (nanoantenna diameter $d \ll \lambda$) [28], the Fröhlich condition, corresponding to LSPR in a Drude free-electron metal nanoantenna, is fulfilled when $\varepsilon_r = -2$. LSPR occurs at $\omega_f = \omega_p/\sqrt{3}$, where ω_f is the Fröhlich frequency. Hence, spectral location of LSPR is directly connected to electron density at the Fermi level, as in n_e ($\omega_f \sim \sqrt{n_e}$).

Table 2.1: Comparison between different modulation mechanisms

Mechanisms	Strengths	Limitations	References
A. Modulation of PNA metallic properties			
Electrical gating	(i) Excellent reversibility; (ii) Stable, no electrochemical degradation	(i) Small electric field sensitivity (0.00028 nm/mV); (ii) Small LSPR shift ($< 2.5\ nm$); (iii) Small SSNR (< 0.09)	[54, 163]
Crystalline phase transition	(i) Large LSPR shift ($> 50\ nm$)	(i) Slow switching time (minutes); (ii) Non-localized	[164]
B. Modulation via loading			
Capacitive loading			
Loading in bulk medium	(i) Large LSPR shift ($\backsim 192\ nm$); (ii) Small gating voltage ($\backsim 1\ V$)	(i) Instability due to photobleaching; (ii) Slow switching time (seconds); (iii) Limited tuning range	[165–168]
Nanoscale loading	(i) High electric field sensitivity (0.91 nm/mV); (ii) High SSNR (> 200); (iii) Fast response ($200\ \mu s$); (iv) Low energy consumption ($9\ fJ/pixel$); (v) Excellent reversibility	(i) Limited tuning range; (ii) Electrochemical degradation	[54, 57, 67]
Inductive loading			
Graphene nanoload	(i) Large LSPR shift ($> 650\ nm$) (ii) Excellent reversibility	(i) Limited to NIR and MIR wavelengths; (ii) Large gating voltage ($> 10\ V$)	[169]
Metal nanoload	(i) Large optical contrast ($\backsim 80\%$)	(i) Limited reversibility ($\backsim$ 30 cycles); (ii) Electrochemical degradation; (iii) Complicated nanofabrication	[43, 170]
C. Modulation via near field coupling			
	(i) Low energy consumption; (ii) Large LSPR shift ($> 100\ nm$); (iii) Excellent reversibility	(i) Small SSNR; (ii) Sophisticated optical setup	[155, 171, 172]

2.3.1 Crystalline phase transition

Catalytically active non-coinage transition metals, such as metal hydrides, have emerged as a particularly strong class of active nanoplasmonic devices (Figure 2.6a). These materials typically undergo in situ, reversible crystalline phase transformations between metallic and dielectric hydride states through hydrogenation and dehydrogenation (Figure 2.6b). The resultant crystal and electronic structural alterations lead to dramatic changes in the optical properties of PNAs, thereby causing noticeable spectral shifts in their LSPRs. Metal hydride-based PNAs have been reviewed extensively elsewhere [60, 173], and we give only a brief overview here using an optical circuit model. Up to now, metal hydrides have attracted significant interest for the development optical hydrogen sensors [164, 174, 175], switchable mirrors [176, 177], chirality switching [178], and dynamic color displays [162]. Palladium (Pd), magnesium (Mg), zirconium (Zr), titanium (Ti), and vanadium (V) are some of the most promising metal hydride materials. Mg, in particular, has attracted a great deal of attention [60] due to its earth-abundance, low cost, reversibility, superior plasmonic properties at high optical frequencies. Furthermore, it offers excellent gravimetric and volumetric hydrogen capacities [179], and benefits from the high surface-to-volume ratios offered by this material. Recently, there is growing interest in creating metal alloy (e.g. $Mg - Pd$, $Au - Pd$) PNAs to realize broader dynamic tuning range and faster response times. Another focus is to suppress the unfavorable hysteresis effect during the de-/hydrogenation processes with respect to single-metal-based devices [60, 175](Figure 2.6c).

2.3.2 Electrical gating

Field-effect tuning of free carrier density in metals offers reversible modulation capability of PNA spectral behavior at high switching speeds [180–182]. Modulation of the plasmonic response of a PNA via an externally applied bias can be accomplished in either dielectric media [54, 55] or ionic solutions [72, 183]. In a typical dielectric medium such as air, an applied bias tunes plasmonic resonances by changing the carrier density n_e of the PNA within a skin depth at the surface, kown as Thomas-Fermi screening length [153, 184, 185]. Depending on the direction of the applied electric field, carrier density Δn_e increases (decreases) due to charge accumulation (depletion) [186, 187]. This free-carrier density variation results in alteration of the plasma frequency ω_p. According to Drude model, changing electron density leads

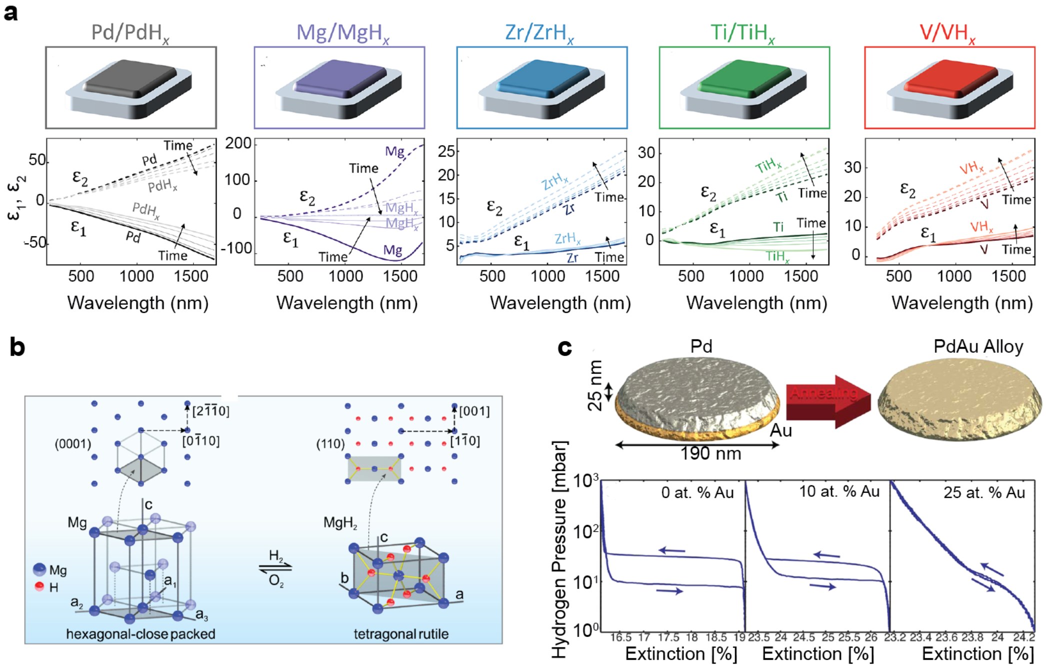

Figure 2.6: Crystalline phase transition: (a) In situ crystalline phase transformations. Top panels show schematics of PNAs consisting of metal and metal hydrides. Bottom panels display the complex dielectric function of each metal and its hydride. Adapted from Ref. [173]; (b) Crystallographic phase transition between metal and metal hydrides takes place during de-/hydrogenation processes. Inset shows the atomic arrangements in the $Mg(0001)$ and MgH_2 (110) crystal planes. Adapted from Ref. [60]; (c) Suppression of the unfavorable hysteresis effect during de-/hydrogenation processes by using metal alloy PNAs. Top panel illustrates the nanofabrication of metal-alloy PNA using the hole-mask colloidal lithography (left) and thermal annealing (right) methods. Bottom panel displays the hydrogen adsorption and desorption isotherms for three different alloy compositions. Adapted from Ref. [175].

to modulation of the metal permittivity, causing spectral shifting in the LSPR frequency of the nanoantenna [188].

Compared to electrical biasing in dielectric medium, electrical gating within a ionic medium (i.e., liquid- or solid-state electrolyte solution) can lead to larger LSPR resonance shift [189, 190]. Modulation of plasmonic response in ionic medium can be achieved through either non-Faradaic charging [62, 191] or Faradaic charging [192–194]. In non-Faradaic processes, application of an electrical potential difference between PNA and a reference electrode results in the formation of an atomic scale (Å) electrical double layer (EDL) in the close vicinity of the nanostructure surface. EDL consists of an internal Stern layer and an adjacent Gouy-

Chapman diffuse layer: (i) the Stern layer is formed by specific adsorption of counterions, while (ii) the diffuse layer emerges by the nonspecifically adsorbed ions that screen the charges on the PNA surface (Figure 2.7a). The strong electric field build up in the EDL results in alteration of the plasma frequency ω_p ; thereby, it leads to spectral shifting of the PNA resonance with an external electric field [189, 195, 196]. Using the Drude model and double-layer capacitor approximation, the modulation depth and speed of modulation for the plasmon resonance can be found [196, 197]. The amount of the resonance shift is found to linearly scale with the applied potential, whereas the switching speed is determined by the RC charging time of the EDL. A key demonstration of non-Faradaic charging was reported by Somekh's group [191, 195]. They demonstrated that the scattering intensity of PNAs can be modulated through non-Faradaic charging processes using an external electrode. In addition, they showed that the surface plasmon modes of the PNAs with elongated morphologies (plate- or rod-shape) exhibited higher oscillator strengths and therefore were more sensitive to surface charge perturbations with respect to PNAs with spherical shapes [191].

In Faradaic charging, electrochemical reactions take place at the interface between PNAs and their surrounding electrolyte [154, 198–202]. This process involves electron transfer between the chemical species and the plasmonic nanostructures. In Faradaic electrochemical dis-/charging processes, metallic nanoantenna is coupled to redox reactions (oxidation/reduction), acting as a reservoir for the electrons (Figure 2.7b). Throughout cyclic redox reactions, the electrons can be stored in the PNAs and donated to the chemical species in an alternating manner. Electron transfer in and out of plasmonic structure leads to cyclic spectral shifting (blue-/red-shifting) of the LSPR of the PNA. So far, the Faradaic charging mechanisms have been employed to monitor the catalytic behavior [200,203,204], visualize photoinduced electrons [205], and observe the dynamics of electrochemical reactions [201,206,207]. Both non-Faradaic and Faradaic charging methods afford accurate control and manipulation of the free-carrier density of PNAs. However, both fall short of the field sensitivity requirements for practical applications such as neural action potential monitoring and electro-optic modulation. This is due to the metals' high intrinsic free carrier density ($10^{23}\ cm^{-3}$), which is significantly higher than the modulation itself ($n_e \gg \Delta n_e$) at practical voltages. Modulation of metal plasma frequency is often negligibly small ($\Delta\omega_p = \Delta n_e\,(\omega_p/2n_e\,)$) [54]. One promising approach to mitigate this issue is to use low-electron-density metals such as indium tin oxide ($10^{20}\ cm^{-3}$) or an elec-

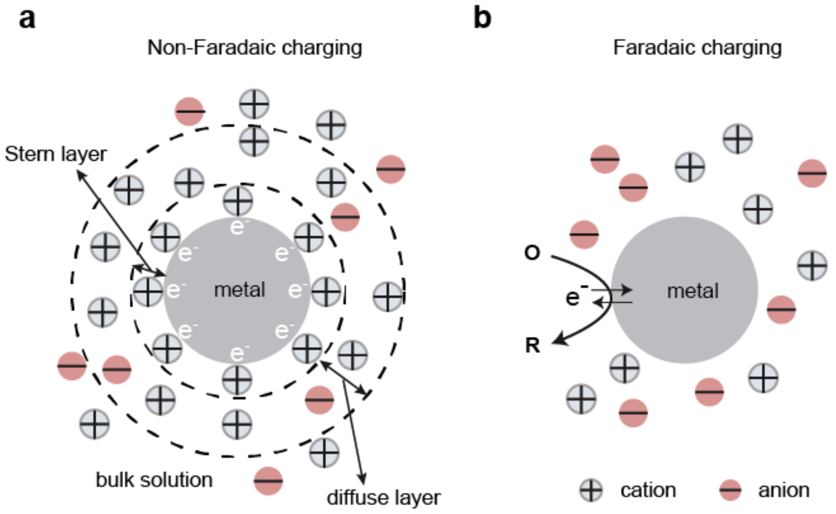

Figure 2.7: Faradaic and non-Faradaic charging of PNAs: (a) Non-Faradaic charging results in redistribution of free carrier charges in an atomic-scale electrical double layer surrounding the PNA; (b) Faradaic charging leads to injection or extraction of electrons through redox electrochemical reaction.

trochromic polymer (electron density 10^{18} cm^{-3}). However, low density metals offer LSPRs at long wavelengths, corresponding to THz frequencies [72, 208].

2.3.3 Loading of plasmonic nanoantennas

Alterations in the effective refractive index of PNA's surrounding dielectric medium offers an effective way to dynamically tune the peak position of the plasmonic resonance (Figure2.5b). Because the local electromagnetic field extend beyond the physical boundaries of a PNA, the resonant characteristics of PNAs are extremely sensitive to dielectric environment surrounding it. Therefore, active PNAs can be realized by modulating the complex dielectric function of the surrounding medium via an external mechanism. To date, the most promising active dielectric materials include liquid crystals [209–212], nonlinear materials [213–215], photochromic dyes [165, 216], amorphous crystalline phase change materials [217–221], pH sensitive polymers [222, 223], and electroactive materials [166, 224, 225]. These materials alter their refractive indices in response to applied stimuli including pH, temperature, light, electrical, and magnetic fields, leading plasmonic response modulation. Active control of the plasmon resonance of PNAs is achieved by controlling light-matter interactions within a nanometer volume (plasmonic hot spot) near the antennas, which is typically much smaller than the volume of the bulk active medium. For some applications, such as multiplexed neural tracking with subcellular resolutions [54] and dynamic color displays [162], it is desirable to minimize the active media thickness conjugated to PNAs in order to attain high plasmon switching speed. One effective approach is to incorporate the active materials into passive PNAs for external nanoscale loading (Figure 2.5b, right panel, second row).

Antenna loading, an elegant concept adapted from RF communications, offers a new degree of freedom and tremendous flexibility in real-time dynamic control of the far-field optical response of PNAs in a reversible and programmable manner. In RF engineering, a typical loaded antenna consists of two half-dipole antennas separated by a feed-gap. The feed-gap is often connected with an electronic circuit that can be readily tuned externally, which enables active modulation of antenna response. In essence, tunable feed-gap is an indispensable part of conventional RF antennas and provides practical testbeds for dramatic enhancement of the 'electrical length' (that is electrical resonance) of RF antennas. By employing lumped electronic circuit elements at this inter antenna gap, broadband resonant antennas can be realized without being limited by their fixed and small physical dimensions. From a fundamental perspective, the 'electrical length' concept plays a crucial role in allowing the tuning and matching properties of RF antennas to be tailored with great degree of freedom and without the need to physically alter the antenna's length or shape.

Inspired by tunable conventional RF technology, researchers have designed its plasmonic analogues loaded PNAs (LD PNAs) , which are composed of two tightly coupled nanoantenna arms separated by a narrow tunable gap at deep subwavelength scale [106, 139, 140]. This 'slot region' is in analogy to the feed element in RF antennas [140, 226]. Inter-antenna feed-gap load can be externally controlled, opening the door for active spectral tuning of the optical nanodipole antennas (Figure 2.5b). From the optical nanocircuit perspective, inserting active nanoloads of adjustable dielectric functions into the slot region leads to variations in the feed-gap capacitance/inductance. This results in a change in the resonance frequency and lead to altered far-field extinction spectrum of the antenna-load system. We want to emphasize that the framework of nanocircuit theory is the key in designing tunable LD PNA systems with desired functionalities. This is because the theory offers unambiguous physical insights into the general behavior of LD PNAs in response to external stimuli that give rise to remarkable

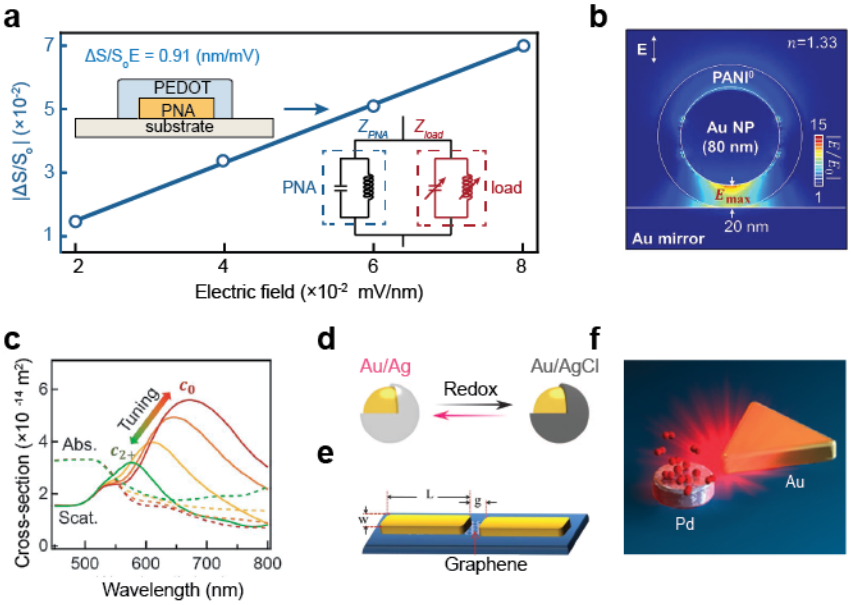

Figure 2.8: Loading of PNAs: (a) Non-Faradaic modulation of the scattering intensity of a PEDOT:PSS loaded Au-PNA (red) enables strong electro-optic modulation capability; (b) Local field enhancement (hot spot) of the LD-PNA. Adapted from Ref. [67]; (c) Optical scattering of the PANI-based LD-PNA shows a dramatic change in both spectral resonance and intensity during a Faradaic charging process. (left to right: oxidized to reduced PANI). Adapted from Ref. [67]; (d) A LD-PNA is created in an Au/Ag core shell fashion. Ag is employed as an inductive nanoload. Reversible transition of the nanoparticle shell between Ag and AgCl tunes the optical property of the LD-PNA. Adapted from Ref. [170]; (e) Graphene, serving as a inductive nanoload, is inserted into the inter-antenna gap to create a LD-PNA structure. Electrical gating of graphene modulates its free carrier density, leading to a change in the nanoload inductance and thereby alters the spectral resonance of the LD-PNA. Adapted from Ref. [169]; (f) Schematic showing a LD-PNA that incorporates Pd as a inductive nanoload, which can exhibit a significant change in its dielectric function during a reversible crystallographic phase transition triggered by de-/hydrogenation. Adapted from Ref. [43].

variations of the permittivities of their nanoloads. Moreover, it provides clear guidelines in designing tunable LD PNAs with excellent modulation depths, low switching thresholds, and ultrafast time responses.

To date, researchers have harnessed strong light-matter interactions enabled by PNAs to create novel LD-PNA configurations with varying levels of sophistication. Beyond the traditional split nanodipole antenna layout [145, 227–229], LD-PNAs have been designed in a sphere-, rod-, disc-, and dumbbell-shaped core/shell heterostructure [54, 67, 170, 230–232], heterodimer [43, 174, 233], composite trimer [234], molecular-level grafting [56, 235–237],and atomic-scale filamentary bridge [61, 169] configurations. In all these proposed nanoantenna configurations, the thickness of the nanoload is generally not larger than the electromagnetic field decay length of LD-PNAs. A fundamental reason behind this is ultrathin nanoloads not only facilitate the exploitation of the strong light confinement and local-field enhancement offered by PNAs, but also permit efficient in- and out-coupling of local physical mechanism (external stimuli) to the subwavelength feed-gap volumes (nm^3). Until now, a wide range of active materials, including photoconductive semiconductors (silicon) [227], graphene [169], conductive filament [61], metal (silver) [170], metal hydrides (e.g. Pd) [43, 233], conductive polymers [54, 67, 170, 230–232], and nonlinear optical materials [238], have been employed as tunable nanoloads (Figure 2.5b). These nanoloads change their optical properties depending on external stimuli, which are usually based on pH, ionic strength, light, temperature, phase change, electrical gating, and magnetic tuning [56, 232].

Antenna loading schemes can be classified to two distinct categories: capacitive and inductive nanoloading. Tuning of the capacitive nanocircuit load by electrical gating leads to a novel class of electric-plasmonic devices. In a recent publication, we harnessed the low free carrier density property of a conductive polymer (poly(3,4-ethylenedioxythiophene) polystyrene sulfonate, PEDOT: PSS) to resolve the challenging low inherent electric field sensitivity issue, plaguing pristine PNAs [54]. We demonstrated that non-Faradaic charging of the conductive polymer can be sensitively and readily detected by remotely tracking the evolution in the far-field optical response of the LD-PNA (Figure 2.8a). Furthermore, we observed that Faradaic charging of the polymer through redox reactions also leads to dramatic shift in the spectral resonance of LD-PNAs. The amount of spectral shift is large enough to cause the scattered light to exhibit noticeable color changes. This Faradaic charging scheme together with the conductive polymer could be very useful for development of plasmonic color displays [232, 239–241]. Another prominent example of capacitive nanoloading is reported in an earlier work [67]. Baumberg et al. constructed a LD-PNA platform by incorporating a conductive polymer (polyaniline) as the nanoload. Authors showed that a strong effect of the complex refractive index of this polymer on the LSPR of the LD-PNA. Figure 2.8b shows the electric field profile of the system where an Au-PNA is encapsulated into a polyaniline (PANI) shell in a nanoparticle-on-mirror configuration. The authors utilized the unprecedented field localization (hot spots) in the Au-PNA to enhance the spectral sensitivity of the nanostructure to alteration in the optical properties of the capacitive nanoload. In their demonstration, application of a negative potential results in donation of electrons to the electrochromic nanoload, leading to strong modulation in the far-field spectra. This increased electron density is effectively equivalent to the diminished capacitance of the nanoload. As a consequence, the optical resonance frequency of the LD-PNA decreases. The authors observed strong red-shifting of the plasmonic resonance wavelength of more than 100 nm (Figure 2.8c). On the contrary, reversal of the applied potential polarity causes electrons to leave the nanoload, leading to a blueshift in the antenna resonance (Figure 2.8c). Using Faradaic charging, the scattered light produced by the LD-PNA showed dramatic color change and a palette of different colors were generated.

In the case of inductive loading, metals and two-dimensional materials are among the most promising candidates to realize effective tuning of LD-PNA systems Byers et al. used a metal as an inductive nanoload and demonstrated active plasmon tuning of a Au/Ag core-shell PNA structure in a fully reversible fashion (Figure 2.8d) [170]. By implementing a well-established $Ag - AgCl$ redox chemistry, the authors achieved a drastic change in the dielectric constant in the nanoload by Faradaic charging. This work provides a new direction for the development of layer-by-layer active PNA devices. Yao et al. employed graphene as an inductive nanoload(Figure 2.8e) [169] . They achieved a broad tuning range of more than 650 nm in LSPR through electrical tuning of the graphene electron density [169] . Tuning of inductive nanoload can also be achieved through chemical reaction. A prominent example is the recent work by Liu et al., where the authors harnessed crystallographic phase transition through a process of de-/hydrogenation to modulate the dielectric function of a metal/metal hydride material [43]. In their LD-PNA system, a Pd-PNA, serving as the inductive nanoload, was placed in the near vicinity of an Au-PNA. In this metal-dimer configuration, these two PNAs strongly couple to each other through localized plasmonic excitations. The spectral characteristic of the antenna ensemble strongly depends on the optical properties of the Pd-PNA. When the Pd-PNA undergoes a crystallographic phase transformation from metal to metal hydride upon de-/absorption of hydrogen at its interstitial site, a dramatic change in the Pd's permittivity is observed. Tuning of this inductive nanoload through phase transition leads to significant modulations in the strength of the near-field coupling between the PNAs, thereby causing the far-field optical response of the dimer system to be effectively modulated.

2.3.4 Tuning of near-field coupling

Exploiting the mechanical degree of freedom offers an exciting and intriguing way to dynamically modulate plasmon modes of the nanoplasmonic structures. In a coupled multielement system, the strong near-field interactions among individual components control the optical characteristics. In principle, physical distance between the elements modulates their coupling strength in between, hence the far-field response of the system. This type of dynamic modulation can be understood within the framework of optical nanocircuit theory (Figure 2.5c). So far, there are three distinctively different approaches that have been developed to achieve dynamic tuning of the plasmon coupling strength between closely spaced nanoantenna structures.The first approach involves lithographically fabricated PNAs on a mechanically tunable elastomeric substrate [155–157, 242, 243]. By applying high-strain mechanical deformation (stretching/relaxation) to the compliant substrate, the distance between resonant nanoantennas are modulated with nanometer precision (Figure2.9a). Researchers achieved more than 100 nm spectral tuning range in a reversible and programmable manner. The second approach uses PNAs that are fabricated on a stiff pillar substrate. Pillars can deform when illuminated by high-energy electrons [171], strongly coupling intrinsic mechanical and electromagnetic degrees of freedom. By taking advantage of the in-gap plasmonic modes, researchers have demonstrated a remarkably precise tuning capability with electron beam illumination (Figure 2.9b). The third approach utilizes coupled PNAs fabricated using a bottom-up self-assembly technique. Authors coupled PNAs to each other using molecular structures with a conformational degree of freedom. Researchers demonstrated dynamically reconfigurable plasmonic nanostructures in a programmable manner by selectively manipulating relative PNA alignment via external stimuli such as pH and light (Figure 2.9c) [172, 244].

2.4 Electro-Plasmonic Nanoantenna and Electrophysiology

One of the most exciting and promising applications for dynamic PNAs is wireless measurement of electrophysiological signals. Electrophysiological measurements are used in understanding electrical activity of cells and linking low-level electrogenic circuits to high-level organ functions (e.g. memory and metabolism) [76]. Mapping electrophysiological signals is critical for our understanding of neuroscience, cardiology, and cellular biology at levels ranging

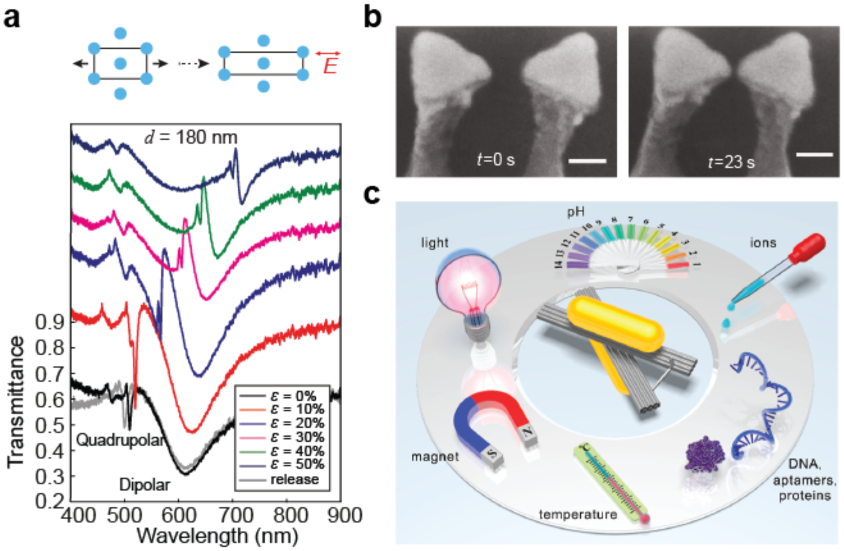

Figure 2.9: Tunable near field plasmon coupling: (a) The optical response of PNAs fabricated on a stretchable soft substrate can be reversibly tuned by strain modulation. Adapted from Ref. [155]; (b) The size of the inter-antenna gap of a pillar-bowtie PNA can be tuned under electron beam illumination. Adapted from Ref. [171]; (c) Schematic of possible ways for dynamic reconfiguration of DNA-based PNAs. Adapted from Ref. [172].

from the molecular and cellular to the behavioral. In this respect, development of electrophysiological recording techniques has created tremendous interest [75, 76, 249] . Since Luigi Galvani's groundbreaking discovery on the electrical nature of neurophysiology in the late 1770s, immense effort invested in the development of electrophysiological tools capable of measuring bioelectric activity of excitable cells [250, 251]. Despite considerable progress made over the past century, no current technology offers simultaneous electrophysiological recordings from large networks of electrogenic cells with high spatiotemporal resolution.

To date, the most reliable, electrophysiological recording tools are micrometer size multielectrode arrays (MEAs) [76, 252, 253] (Figure 2.9a). In principle, MEAs can record local field potentials in the extracellular space induced by transmembrane ion movement during cell firing events [254, 255]. However, use of electrons as information carriers imposes several fundamental constraints due to electronic nature of the measurements. In MEA measurements, every recording site or electrode in the array has to be wired to an external signal processing unit or require on-chip conditioning (Figure 2.9b) [248]. Shrinking the overall footprint of the metal electrodes, although offers markedly increased multiplexity and density of indi-

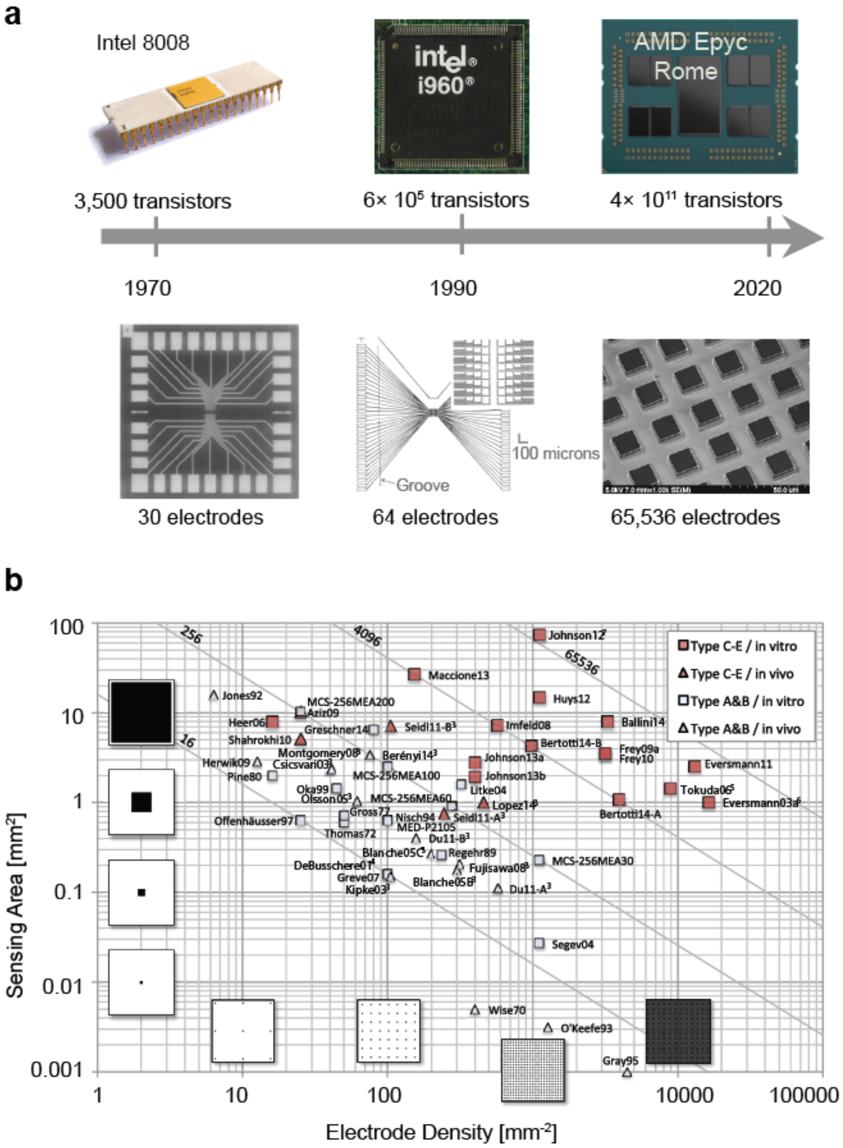

Figure 2.10: Scaling microelectrode arrays (MEAs): (a) A timeline of computer (top panel) and MEAs recording (bottom panel) technologies and transistor over the past five decades. The MEA images are adapted from Refs. [245–247]. The CPU images are adapted from the courtesy of 'Wikimedia Commons' and 'AMD'; (b) MEA comparison in terms of electrode density and total sensing area. Adapted from Ref. [248].

vidually addressable recording channels, adds a high level of complexity in electrical circuitry and wiring. From a circuit-level perspective, reducing electrode sizes inevitably introduces unwanted inter-channel crosstalk and results in unfavorable scaling of electrode impedance and thermal noise, degrading the signal-to-noise (SNR) ratio [256]. This density-versus-noise tradeoff severely restricts the accessibility to desired multiplexing and bandwidth operation capabilities for simultaneous recording of a large number of electrogenic cells. Well-established semiconductor industry manufacturing capabilities allow recording electrodes to be reduced in size and integrated with high density. Implementing extremely small metal electrodes, on the other hand, poses an enormous challenge due to parallel interfacing requirements with relatively sizable peripheral recording electronics that secure connections between multiplexed inputs and outputs [247, 256, 257]. Due to this fundamental bottleneck, the growth in the number of simultaneously recorded electrogenic cells has been limited [256]. Unlike microelectrode recordings, use of photons offers unparalleled (time/wavelength division) billion-fold enhanced multiplexing and information carrying capabilities. Photons are extremely fast, don not interact with each other. One can in principles use photonic elements to can realize high-bandwidth electrophysiological recordings without on-chip conditioning. Achieving this goal, however, largely depends on our ability to recruit reliable electro-optic translators that can efficiently convert bioelectric signals into high photon count optical signals [76]. This necessitates development of new photonic systems with excellent electro-optic characteristics.We recently introduced an ultrasensitive and extremely bright nanoscale electric-field probe enabling wireless monitoring of electrophysiological activity of cells [54]. Using massively multiplexed electro-plasmonic nanoantenna, we demonstrated reliable detection of local electric-field dynamics generated with remarkably high signal-to-shot noise (SSNR) ratios from diffraction-limited spots. In the next chapter, I will discuss this development of electro-plasmonic field probe and a the in-vivo detection of electrophysiological activity.

Chapter 3

Nanoelectrochromic Field Reporters in Electrophysiological Applications

Electrophysiological activity of cells is of fundamental importance to neuroscience, cardiology, and cellular biology. In this sense, development of techniques for optically mapping the electrogenic signals has created significant interest within the scientific community [75, 76, 249]. Photons are remarkably efficient reporters; light offers exceptional spatiotemporal resolution, unparalleled multiplexing, and high-bandwidth operation capabilities well beyond limits of electronic technologies. Harvesting photons for electrophysiological studies, on the other hand, largely depends on our ability to recruit efficient reporters converting local electrogenic activity to high photon-count far-field signals [258–261]. Typically, fluorescence molecules that can translate membrane potentials to an optical signal are used [76, 249]. These genetically encoded voltage indicators (GEVIs) have fundamental shortcomings associated to bleaching of fluorescent molecules (photostability) and generation of disruptive oxygen free radicals (phototoxicity) [76, 258]. Furthermore, GEVIs with tiny cross-sections ($\sim 10^{-2}$ nm^2) [74], and low quantum yields ($QE \sim 10^{-3}$–10^{-2}) [75] offer limited number of fluorescent photons for detection, hence suffer from signal-to-shot noise ratio (SSNR) limitations [76, 258, 259]. More recently, there has been a concerted effort focused on the development of non-fluorescent extracellular optical reporters exploiting inherent voltage sensitivity of noble metals [55, 191, 195, 262, 263] . Unlike fluorescence molecules, plasmonic resonators do not have photostability and phototoxicity limitations or require invasive genetic modifications. In principle, plasmonic nanoresonators with exceptionally large cross-sections ($\sim 10^4$

nm^2) offer orders of magnitude enhanced photon-flux measurements from diffraction limited volumes [264]. The main weakness of the field voltage reporters, on the other hand, is their low inherent electric-field sensitivity. Electro-optic effects in metals associated to non-Faradaic (electric-double layer) charging/discharging are very weak due to extremely high electron densities [72, 265]. As a result, optical field measurements utilizing plasmonic nanostructures are readily dominated by shot noise [265]. Despite extensive efforts, development of label-free and non-invasive optical probes that can detect local electric-field dynamics with high sensitivity, reliability, and spatiotemporal resolution remains elusive.

In this thesis, a new class of extremely bright label-free optical field probes overcoming the photon-count and field sensitivity limitations of state-of-art electro-optic field reporters have been introduced. Our non-invasive extracellular electro-plasmonic nanoprobes, offering more than three orders of magnitude enhanced field sensitivities over conventional plasmonic nanoantennas [55], enable high signal-to-noise ratio measurements from diffraction limited volumes at kilohertz (kHz) frequencies. To achieve ultrasensitive and high signal-to-noise ratio measurements, we employ active lumped nanocircuit elements that are analogous to tunable radio frequency (RF) antennas. Alu and Engheta theoretically formulated that antenna loading, a concept adapted from RF communications, could be employed to dramatically alter the far-field response of nanoscale plasmonic antennas operating in the optical domain [106, 140, 143]. Subsequent experimental studies have successfully shown tunable nanoantenna response by modifying the optical nanoload using lithographic techniques [139, 141], oxidation-reduction chemistry [170], and chemical absorption [43, 158]. Here, we introduce biocompatible electrochromic polymer poly(3,4-ethylenedioxythiophene): polystyrene sulfonate (PEDOT: PSS) as an electric-field controlled load enabling active and reversible tuning of the plasmonic resonances [266]. In reverse operation mode, we show that electrochromically loaded plasmonic (electro-plasmonic) nanoantenna functions as a reporter of the local electric-field dynamics and electrophysiological activity to the far-field. In the following, by projecting the (Au) electrode-PEDOT: PSS system to an equivalent circuit and using electrochemical impedance spectroscopy (EIS) and potential step voltammetry (PSV) measurements, we first optimize the electrochromic load parameters that govern the temporal response of our field probes. Our experiments show that electrochromic switching times of the PEDOT:PSS load can be drastically improved with lateral and vertical down scaling to nanoscale dimensions. We then introduce a selective electropolymerization technique enabling us to conformally coat metallic nanoantenna with ultrathin ($10 - 20$ nm thick) and nanoscale (0.01 μm^2) PEDOT: PSS loads. By performing electro-optic measurements from diffraction limited volumes, we subsequently demonstrate drastically ($\sim$ 3.25×10^3 times) enhanced field sensitivities with electrochromic loading and establish high signal-to-shot-noise ratio (SSNR $\sim 60 - 220$) measurement capability from single electro-plasmonic nanoprobes. Using dark-field opto-electrochemical measurements, we then prove the high frequency operation capability of our nanoprobes at kilohertz frequencies with sub-millisecond (< 0.2 ms) temporal response times. Finally, through our in vitro experiments, we establish label-free and non-invasive optical measurement of electrogenic activity of human induced pluripotent stem cell (hiPSC) derived cardiomyocytes (iCMs) using low-intensity light (11 mW/mm^2), which is two to three orders of magnitude lower than the typical light intensities used for fluorescent voltage probes [258]. Our nanoprobes, exploiting a novel electro-optic mechanism, puts forward a blueprint of an entirely new family of extracellular optical probes with high spatiotemporal resolution and signal-to-noise ratio electrophysiological measurement capability with light. This chapter is a modified version of following publication:

A. Habib and X. Zhu and U. I. Can and M. L. McLanahan and P. Zorlutuna and A. A. Yanik, “Electro-plasmonic nanoantenna: A nonfluorescent optical probe for ultrasensitive label-free detection of electrophysiological signals:,” Science Advances, vol. 5, no. 10, pp. eaav9786, 2019. `https://www.science.org/doi/abs/10.1126/sciadv.aav9786`

3.1 Materials and Methods

3.1.1 Fabrication of plasmonic nanoantenna arrays

Plasmonic nanoantenna arrays are fabricated using electron beam lithography (EBL) followed by a liftoff process (Figure 3.1). To minimize charging effects during EBL, high conductivity ($8 - 12$ Ω/cm) ITO glass slides (Structure Probe, Inc.) are used. Initially, ITO glass slides are cleaned in sonication bath of acetone and isopropyl alcohol for 5 $minutes$. Immediately after removal from the final sonication bath, the slides are blown dried using nitrogen. PMMA 495A4 (Microchem) electron-beam resist is spin coated at 4000 rpm and baked on a hotplate at 180^o C for 90 $seconds$. EBL is performed using FEI Quanta 3D FEG SEM with an accelerating voltage of 30 kV. Electron-beam exposed resist is developed for 1 minute in a

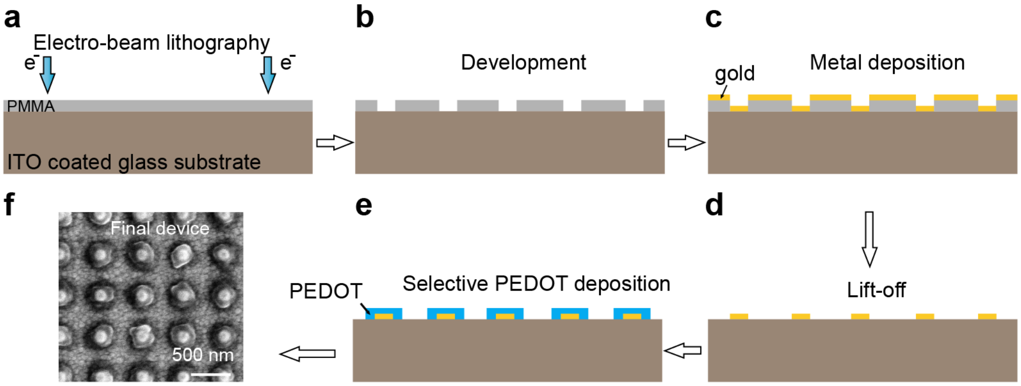

Figure 3.1: Fabrication steps of electro-plasmonic nanoantenna arrays. Electron beam patterning is used to define the nanoantenna using PMMA resist (a). The patterned sample is developed in MIBK: IPA (1:3) solution (b). Gold layer is deposited using a directional metal deposition technique. (c). Lift-off process results in immobilized metallic nanoantennas on the ITO glass substrate (d). Selective electropolymerization of PEDOT: PSS on gold surfaces leads to a conformal and ultrathin electrochromic load around the metallic nanoantenna (e). The SEM image of a fabricated electro-plasmonic nanoantenna array is shown (f).

methyl isobutyl ketone (MIBK)–isopropanol (IPA) solution (MIBK: IPA = 1:3) for 60 s, then rinsed in IPA for 1 $minute$ and blown dry with nitrogen. 45 nm thick gold layer (Kurt J. Lesker, 99.999 % purity) is evaporated on the developed substrates using a custom build electron-beam evaporator. The deposition is carried out at a pressure of 1.2×10^{-6} Torr and an evaporation rate of $0.5\ \AA/sec$. In the final step, the resist is removed through a lift-off process with acetone and IPA leaving behind the pristine plasmonic nanoantenna array on the ITO coated glass substrate.

3.1.2 Full-wave numerical simulations

Pristine and electro-plasmonic nanoantenna arrays are modeled using a full-wave Finite Element Time Domain (FDTD) solver provided by Lumerical Inc. The ”Au (Gold) - CRC” dielectric constants are used for gold structures [267]. The complex dielectric constants of PEDOT load (Figure 3.2) are obtained using Kramers-Kronig relation from a previous experimental study [266]. Perfectly matched layer (PML) boundary conditions are employed in the vertical direction. A linearly polarized excitation source ($400 - 900\ nm$) is employed in our simulations.

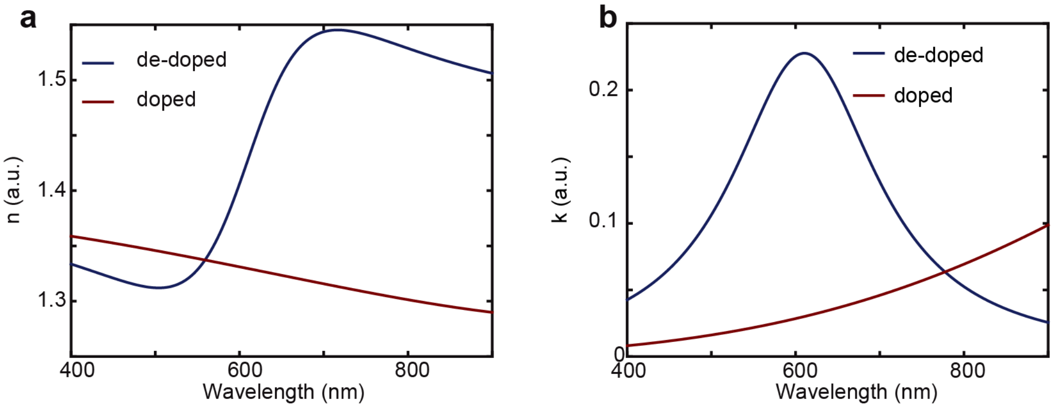

Figure 3.2: Complex refractive index (n-k) of the PEDOT polymer. Refractive index (a) and extinction coefficient (b) of the PEDOT polymer are shown for doped (red curves) and de-doped states (blue curves).

3.1.3 Electropolymerization of ultrathin PEDOT: PSS polymer

Electropolymerization of electrochromic polymer poly(3,4-ethylenedioxythiophene): polystyrene sulfonate (PEDOT: PSS) is performed using a three-electrode configuration. A custom-made platinum coil (Alfa Aesar, 13039) and Ag/AgCl (Warner instruments, $64-1282$) are used as the counter electrode and reference electrodes, respectively. Conducting substrate is employed as the working electrode. An aqueous solvent of $10\ mM$ EDOT monomer and $0.1\ M$ NaPSS is deposited using a galvanostatic approach. A constant current of $0.48\ mA/cm^2$ is applied for $1.67s$ for each $5\ nm$ of PEDOT: PSS film (Figure 3.3). Electropolymerization process is confirmed by cyclic voltammetry (CV) measurements in $0.1\ M\ TBAPF_6$ (Sigma-Aldrich, 281026) in propylene carbonate solution (Sigma-Aldrich, 310328). Selective deposition of PEDOT: PSS on Au surface is achieved using the same aqueous solvent solution under potentiostatic conditions ($740\ mV$ vs. $Ag/AgCl$) for $6.5\ s$.

3.1.4 Electro-optic characterization

To characterize pristine and electro-plasmonic nanoantennas, a custom-built electro-optic measurement platform based on an inverted microscope (Nikon TE2000-U) is used (Figure 3.4a). Its schematic is shown in Figure 3.4b. Electro-optics measurements are performed using a $670nm$ diode temperature stabilized laser modulated at a frequency of $500\ Hz$ (for synchronous detection of scattering signal using lock-in amplifier). The laser is focused onto the

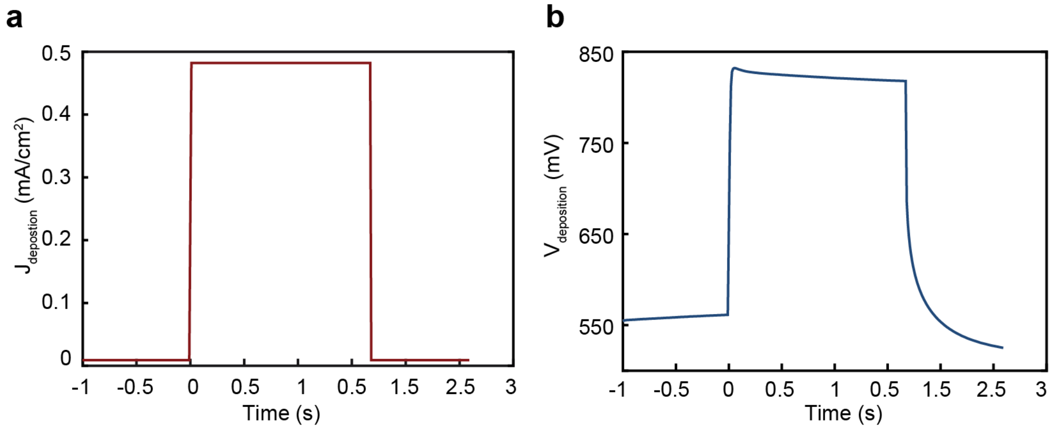

Figure 3.3: Electropolymerization of nanometer thick PEDOT: PSS films. (a) Galvanostatic deposition of $5nm$ PEDOT: PSS on gold electrode (gold substrate). A constant current 0.48 mA/cm^2 is applied for $1.67s$. (b) Corresponding voltage recorded by the potentiostat is shown.

nanoparticles at normal incidence using $40\times$ Nikon S Plan Fluor ELWD objective ($NA = 0.6$). The forward scattering light is collected using a custom collection optics with 50^o to the normal using a collection optics consists of a $20\times$ infinity corrected objective ($NA = 0.4$) with a front aperture of 3 mm, a fiber collimator, and a $600\mu m$ multimode optical fiber patch cable. The collected light is measured using a fiber-coupled silicon photodetector (Thorlabs PDA100A). A lock-in amplifier (Stanford Research Systems SR850) connected to an oscilloscope (Rigol DS4034) is used for detection. To characterize voltage dependent scattering response (electric-field sensitivity) of the nanoantenna, a second ITO covered glass slide is used as the counter electrode. The separation between electrodes is set to 100 μm using a PDMS spacer layer. A function generator (Rigol DG4102) is employed to control the applied voltage difference (electric field) between electrodes. The voltage-dependent ac scattering signal is measured using the lock-in amplifier, while the dc component of the scattering signal is monitored using the oscilloscope.

3.1.5 Optical circuit model

Optical circuit theory provides a useful theoretical framework [137] in understanding and engineering of complex nanoantenna structures [136]. Complex nanoantenna topologies can be quantitively analyzed as nanocircuits consisting of circuit elements with optical

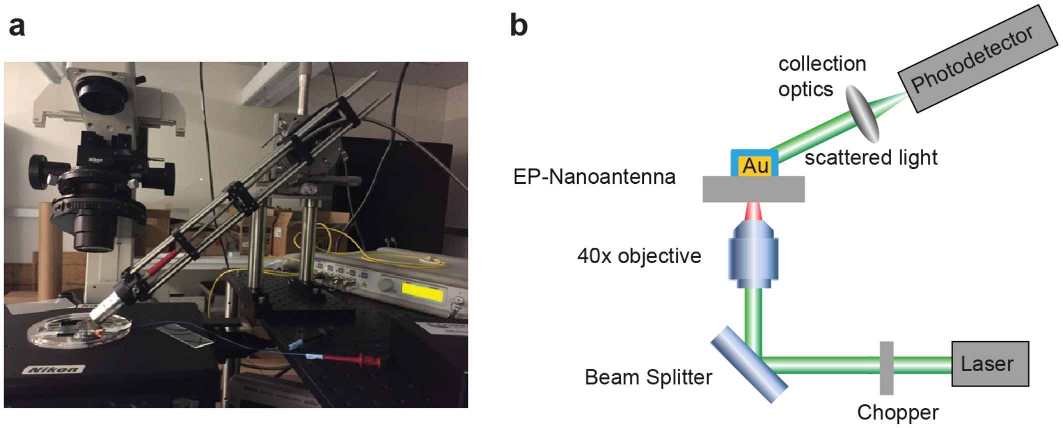

Figure 3.4: Electro-optic characterization setup. (a) The optical setup used in electro-optic characterization measurements for electric-field sensitivity is shown. (b) Schematics of the electro-optic setup is given.

“lumped impedance”, analogous to conventional electronics such as inductors, capacitors, and resistors. By solving Maxwell’s equations and calculating the electric displacement currents using Kirchhoff’s current law, the optical impedance of an electro-plasmonic nanoantenna can be found [137]. In our analysis, we first find equivalent circuit model of pristine nanoantenna, and then incorporate electrochromic PEDOT load to it. We define the metallic (Au) nanoparticle as a serially connected inductor and resistor (Figure 3.5a). Here, the inductor represents the negative permittivity of the metal, while the resistor incorporates ohmic and radiation losses [137]. The medium and glass substrate around the metallic nanoparticle are included as a parallel shunt nanocapacitor. The combined (effective) optical impedance of the nanoantenna is defined as $Z_0 = R_0 + jX_0$. Using FDTD simulations (Figure3.5b), the inductance $L_{\text{Antenna}} = 14\,\text{fH}$, capacitance $C_{\text{Antenna}} = 8$ aF, and resistance $R_{Antenna} = 3\ \Omega$, values are obtained through a retrieval method described in an earlier work [137, 144]. Based on this circuit parameters, the intrinsic resistance R_0 and reactance X_o are calculated as a function of the wavelength (Figure 3.5c). The optical circuit parameters obtained for the pristine nanoantenna are subsequently used in development of the equivalent circuit model of the electrochromically loaded nanoantenna. Electrochromic load is added to the pristine circuit model as a parallel tunable capacitor, representing the nonzero, positive and electric-field controlled real part of the PEDOT permittivity (Figure 3.5d). The capacitance of the PEDOT load is calculated using $C_{\text{PEDOT}} = \varepsilon_{\text{PEDOT}}\pi\left(r_0^2 - r_i^2\right)/h$ [140], where $\varepsilon_{\text{PEDOT}}$ is the load permittivity (obtained from ref. [266] using Kramers-Kronig relation), r_0 is the radius of the pristine Au nanoantenna and r_i (h) are the radius (height) of the electro-plasmonic nanoantenna with the conformal PEDOT layer. The nonzero imaginary part of the PEDOT permittivity is incorporated using a tunable resistor R_{PEDOT} [266]. The capacitance and resistance values of the electrochromic load are 1.49 aF (1.76 aF) and $350\ \Omega$ ($120\ \Omega$) for fully doped (de-doped) state. Capacitances (inductances) of the electro-plasmonic nanoantenna is extremely low, in the aF (fH) range. Hence, the electro-plasmonic nanoantenna has resonance frequencies $\omega_{res} = (LC)^{-1/2}$ in the visible regime.

3.1.6 Stem cell culture

1016SevA line human induced pluripotent stem cells (hiPSCs) are cultured on Geltrex (1 $\%$, Invitrogen, USA) coated culture flasks in mTeSR1 media (StemCell Technologies, Canada) supplemented with penicillin and streptomycin (P/S) (1 $\%$, Life Technologies, USA). hiPSCs are passaged using Accutase (StemCell Technologies, Canada) to detach, at approximately 70 $\%$ confluency, and seeded with Rho-associated, coiled-coil containing protein kinase (ROCK) inhibitor (5 μM, StemCell Technologies, Canada) supplemented mTeSR1. The culture is kept with daily media changes until 70 $\%$ confluency for passaging or 95 $\%$ confluency for differentiation.

3.1.7 Cardiomyocyte differentiation, maintenance and Ca^{2+} imaging

hiPSC derived cardiomyocyte (iCM) differentiation induction are adapted from a previously established protocol [268–270]. Briefly, RPMI Medium 1640 (Life Technologies, USA) are supplemented with beta-mercaptoethanol (3.4×10^{-4} $\%$, Promega, USA), P/S (1 $\%$) and B27 without any insulin (2 $\%$, Invitrogen, USA) (CM (-)) or B27 (2 $\%$, Invitrogen, USA) (CM (+)). On day 1, hiPSC media are replaced with CM (-) media with the addition of Wnt activator CHIR99021 (CHIR) (10 μM, Stemgent, USA). On day 2, 24 hours after the differentiation is initiated media are changed to CM (-). On day 4, iCMs are treated with Wnt inhibitor IWP-4 supplemented (10 μM, Stemgent, USA) CM (-) media. On day 6, the media are changed to CM (-) again. Starting from day 9-on media are changed every 3 days with CM (+). On day 35, iCMs are collected using trypsin-EDTA (0.25 $\%$, Corning, USA) and reseeded on fibronectin in phosphate-buffered saline (PBS) (50 μg/ml, Sigma-Aldrich, USA) coated substrates. iCM

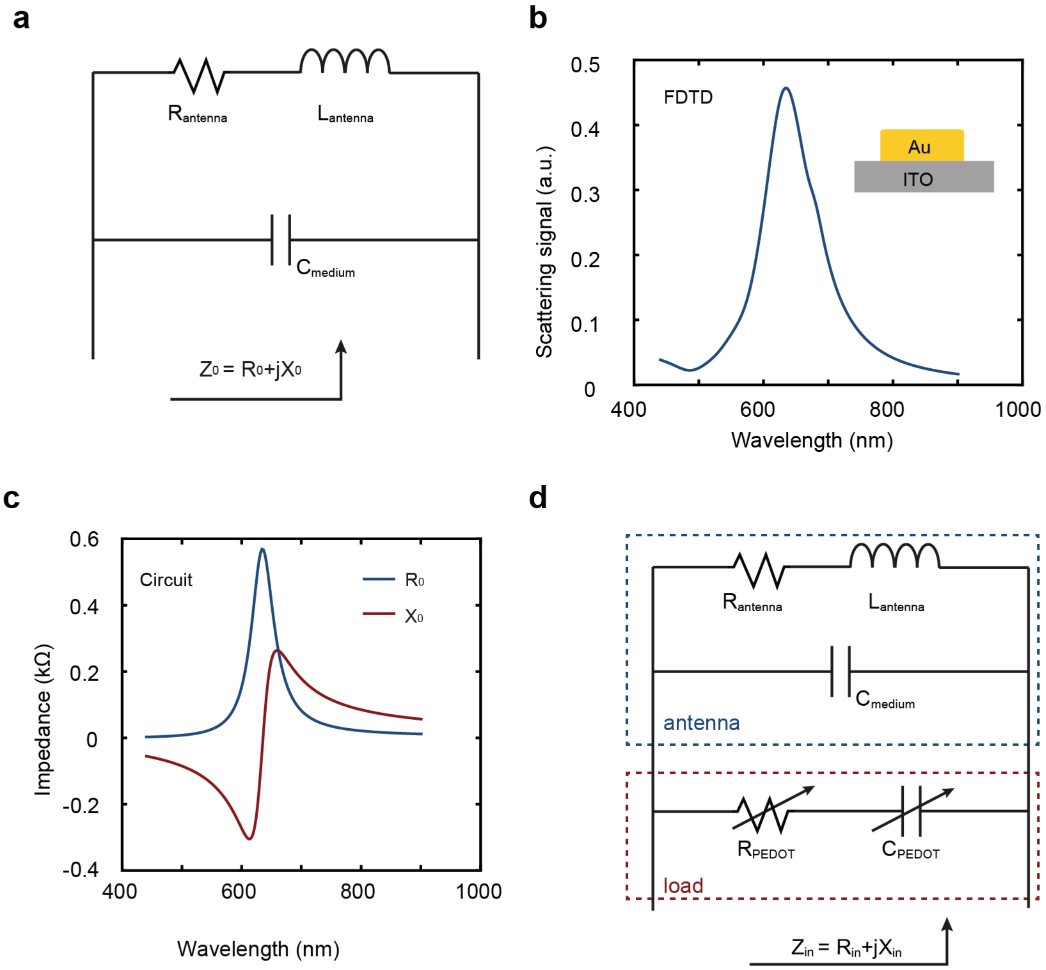

Figure 3.5: Lumped optical circuit model of nanoantenna. (a) Lumped nanocircuit model for the pristine nanoantenna is shown. (b) Scattering spectrum of the pristine nanoantenna obtained using FDTD simulations. (c) The resistance and reactance of the equivalent nanocircuit of the pristine nanoantenna is shown as a function of wavelength. (d) Equivalent nanocircuit model of the electro-plasmonic nanoantenna. Electrochromic doping is incorporated through tunable resistor and capacitor elements.

culture are then maintained in Dulbecco's Modified Eagle Medium (Hyclone, USA, DMEM) supplemented with fetal bovine serum (10 %, Hyclone, USA, FBS) and P/S (1 %) (DMEM). Functionality of iCMs is confirmed using Ca^{2+} indicators. iCMs are loaded with Fluo-4 acetoxymethy ester (Molecular Probes), which exhibits an increase in fluorescence intensity upon binding to Ca^{2+}, following manufacturer's instructions. Briefly, iCMs are incubated in Tyrode's salt solution (Sigma-Aldrich) loaded with 3 μM Fluo-4 acetoxymethy ester and 0.02 %

Pluronic F127 (Life Technologies) and incubated at 37 ^{o}C for 30mins. Then washed with Tyrode's salt solution and kept in normal culture medium. Ca^{2+} fluxing during spontaneous contractions are captured using high-speed fluorescence microscope imaging (Axio Observer.Z1, Carl Zeiss).

3.1.8 SEM imaging of cardiomyocytes

For SEM imaging, cells are fixed for 1hour in using 2 $\%$ glutaraldehyde (Sigma-Aldrich, USA) in sodium cacodylate buffer (Sigma-Aldrich, USA). Then another fixation step is performed for 1hour using 1 $\%$ Osmium tetroxide in sodium cacodylate followed by dehydration in 10 $\%$ ethanol. Finally, critical point drying is performed, and samples are attached to an SEM stub.

3.1.9 Photothermal heating

To investigate plasmon-assisted photothermal heating, we performed optical and thermal simulations of in pristine plasmonic nanoantennas (height 45 nm, diameter 90 nm, periodicity 500 nm) in solution environment using Lumerical's FDTD Solutions and Heat Transport Solver [271]. A broadband transverse magnetic plane wave source covering a wavelength range of $400 - 900$ nm is employed to illuminate the plasmonic nanoantenna array (11 mW/mm^2). The heat generation due to the Joule heating can be obtained from the heat source density given by $q = \vec{E} \cdot \vec{J}$, where $\vec{E}$ is the electric field and $\vec{J}$ is the current density. The total heat power Q generated inside the nanoantenna is a volume integral of the heat source density

$$Q = \int\limits_{V} q\left(r\right)\ d^3r \tag{3.1}$$

where $V$is the volume. Absorbed power obtained from FDTD simulations are used in the Heat Transport Solver to calculate to the three-dimensional temperature distribution around the plasmonic nanoantenna. The simulation region above the nanoantenna array is covered by water and the convection induced heat loss at the top surface of individual nanoantennas is modeled at the interface between water and nanoantennas. The simulation boundary was kept at room temperature (20 ^{o}C) by applying a fixed temperature thermal boundary condition at the bottom of the ITO substrate. Near-field enhanced electromagnetic field could be significantly high heat

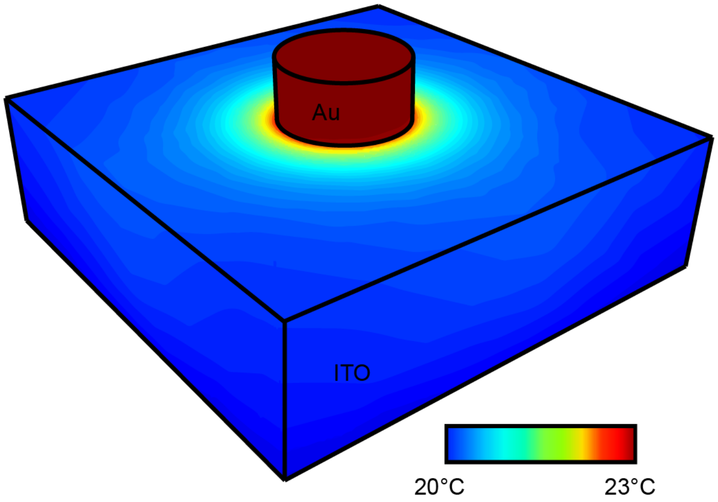

Figure 3.6: Photothermal heating due the nanoantenna. Temperature profile around the nanoantenna ((height 45 nm, diameter 90 nm) is shown. A small temperature (3 ^{o}C) rise relatively ambient is observed within close vicinity to nanoantenna.

source densities. However, due to small volume of our electro-plasmonic probes and low light intensities used in our experiments, a limited temperature increase is observed in our analysis. For an incident beam width of 1.13 mm covering approximately 4-million nanoantennas, the maximum temperature rise with respect to room temperature is about 3 ^{o}C, as shown in Figure 3.6.

3.2 Results

3.2.1 Electro-plasmonic nanoantenna

We use far-field response of the electro-plasmonic nanoantenna to monitor the local electric-field dynamics as summarized in Figure 3.7. Scanning electron microscope (SEM) image in Figure 3.7a demonstrates the substantial size difference between typical electrogenic (cardiomyocyte) cells and our electro-plasmonic field probes. The key advantage of electro-plasmonic probes is their potential for massive multiplexing through remote transduction of the local electric fields without being restricted by electrode layout or physical connections. Electro-plasmonic nanoantenna (height 45 nm and diameter 90 nm) when arrayed with sub-micron periodicity offers electric-field measurements with light from diffraction limited spots.

Using nanolithographic techniques, an array of 2.25 million electro-plasmonic nanoantennas (500 nm periodicity) is fabricated on a transparent indium tin oxide (ITO) coated glass substrate. To probe electric-field dynamics, we load the pristine plasmonic nanoantennas with PEDOT: PSS electrochromic polymer. With electrochromic polymers, thicker films are desirable to achieve strong electro-optic signals. Ultrathin layers, on the other hand, are required for faster charge-modulation characteristics [272]. Our analysis based on three-dimensional finite difference time domain (FDTD) simulations shows that plasmonic nanoantenna strongly confines the electromagnetic field within a narrow region around it (Figure 3.7b and Figure 3.7c). By taking advantage of drastically enhanced the light-matter interactions in these plasmonic hot spots, we can simultaneously achieve strong electro-optic sensitivity and fast electrochemical response using ultra-thin electrochromic loads.

Adopting RF antenna concepts, the far-field response of our electro-plasmonic nanoantenna to the local electric-field dynamics could be understood within the framework of optical circuit theory [106,136]. Here, the electrochromic load is incorporated to the lumped equivalent nanocircuit as a parallel arm composed of resistive (ohmic losses) and capacitive lumped-circuit elements. In our analysis, we first find the equivalent optical circuit parameters of pristine nanoantenna. Optical circuit parameters are obtained using FDTD simulations and a semianalytical retrieval method [139]. We then incorporate electrochromic load. The electric-field controlled capacitance of the electrochromic load couples the low-frequency local electric-field dynamics (< 1 kHz) to high-frequency (~ 460THz) electromagnetic resonances. Wavelength dependent susceptances of the lumped nanocircuit elements corresponding to pristine nanoantenna and its electrochromic load are shown in Figure 3.8. Optical circuit resonances occur when the intrinsic susceptance $\mathrm{Im}\,[1/Z_{antenna}\,]$ of the pristine nanoantenna (black solid curve) is compensated by the capacitive susceptance $-\omega C_{PEDOT}$of the electrochromic load in the doped (red curve) and de-doped (blue curve) states. The resonances occur at the intersections highlighted by the circles in Figure 3.8, leading to maximum scattering signal. For the doped (de-doped) electrochromic load, the resonance condition occurs at the shorter (longer) wavelength intersection (Figure 3.8). This is associated to the diminished resistive losses of the electrochromic load at the corresponding operating wavelength (Figure 3.2). Our circuit model clearly shows that switching from the doped (red curve) to de-doped (blue curve) state of the electrochromic load causes red shifting of the far-field plasmonic response in agreement with

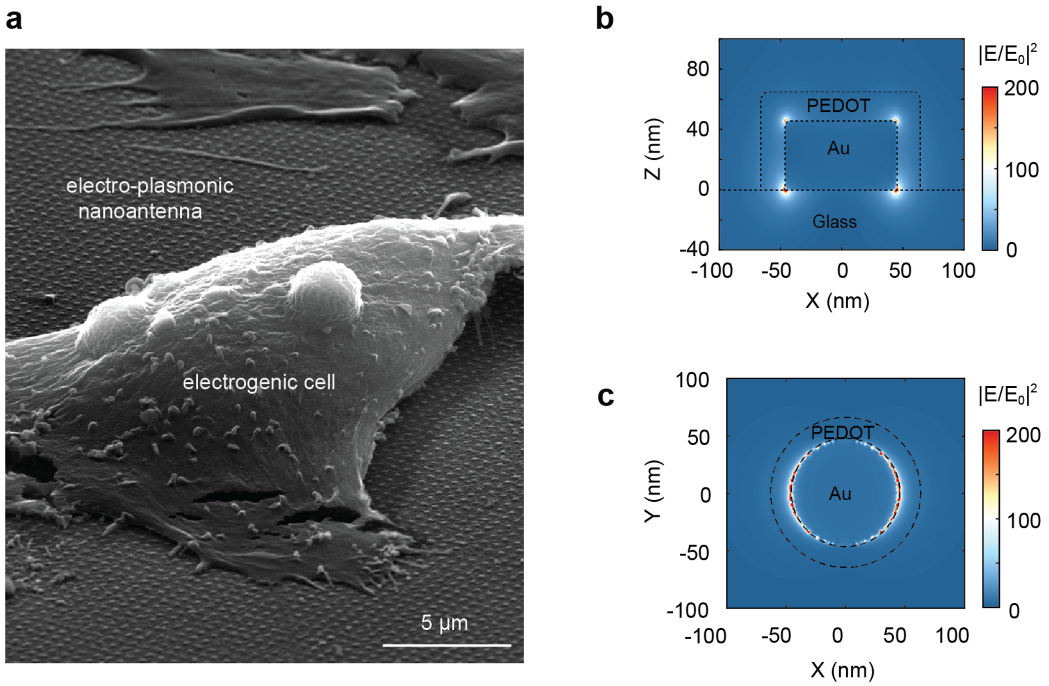

Figure 3.7: Electro-plasmonic nanoantenna. (a) Scanning electron microscope (SEM) image of cardiomyocyte cells cultured on an array of electro-plasmonic nanoantenna. Considerable size difference between loaded nanoantennas (height 45 nm, diameter 90 nm) and electrogenic cells is shown. 2.25 million electro-plasmonic nanoantenna are incorporated on a transparent substrate with nanometer spatial resolution, allowing measurement of electric-field dynamics from diffraction limited spots over a large surface area. (b) Side-view of near-field enhancement $|E/E_o|^2$ along the pristine nanoantenna at 678.8 nm. FDTD simulations show that plasmonic excitations lead to strong confinement of the light within the 20 nm thick electrochromic layer. (c) Top view of the near-field enhancement $|E/E_o|^2$ profile along the center of the pristine nanoantenna at 678.8 nm.

our FDTD simulations (Figure 3.9). Strong agreement in between FDTD simulation and optical circuit models is also observed for the spectral features and quality factors. Far-field response of our electro-plasmonic nanoantenna, a reporter of the local electric field dynamics, can be measured using spectroscopic or intensity-based techniques.

3.2.2 Nanoscale loading for sub-millisecond response times

To achieve high field sensitivity, we used PEDOT: PSS polymer as a field controlled nanoload coupled to the metallic nanoantenna (Figure 3.10a). In addition to its strong electro-optic properties, PEDOT has a number of advantages: (1) it shows fast and reversible elec-

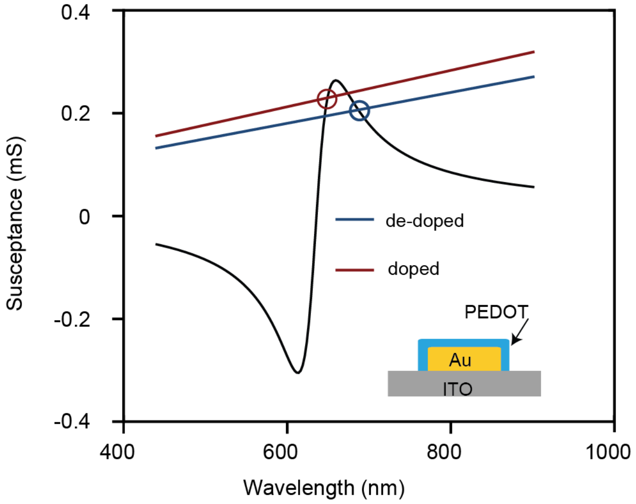

Figure 3.8: Susceptances of the gold nanoantenna and the PEDOT: PSS load for doped (red) and de-doped states (blue) are shown. Intersections (indicated by the circles) correspond to the open-circuit condition, the plasmonic resonance. For the doped (de-doped) electrochromic load, the resonance condition occurs at the shorter (longer) wavelength intersection due to the diminished resistance (losses) of the electrochromic load.

trochromic response, (2) it is stable as a thin film (down to 10 nm thicknesses) with high capacitance (routinely used in supercapacitors), (3) it is a biocompatible polymer that is extensively used in microelectrode arrays (MEAs) to improve electrical coupling between the electrodes and excitable cells, (4) it could be functionalized with biomolecules that stimulate cell growth and molecular attachment [273, 274]. In our experiments, we doped PEDOT polymer with poly(styrenesulfonate) (PSS) to lower the electrical impedance to achieve stronger electrical coupling to the local field [275]. Precisely controlled PEDOT:PSS layers are electropolymerized on gold electrodes using a galvanostatic approach in an aqueous solution containing 10 mM EDOT (3,4-Ethylenedioxythiophene) monomer and 0.1 M sodium poly(styrenesulfonate) ($NaPSS$). Electron microscopy measurements are used to determine the thicknesses of the electrodeposited ultrathin PEDOT: PSS films. Cyclic voltammetry (CV) measurements are subsequently performed to verify the reliability and repetability of the polymer layer deposition process. Our analysis shows that thicker PEDOT: PSS films yield larger capacitances as shown in Figure 3.10b, where the area enclosed by the voltammogram trace is a measure of the total capacitance.

Fast electro-plasmonic response to electric-field dynamics is essential to accurately

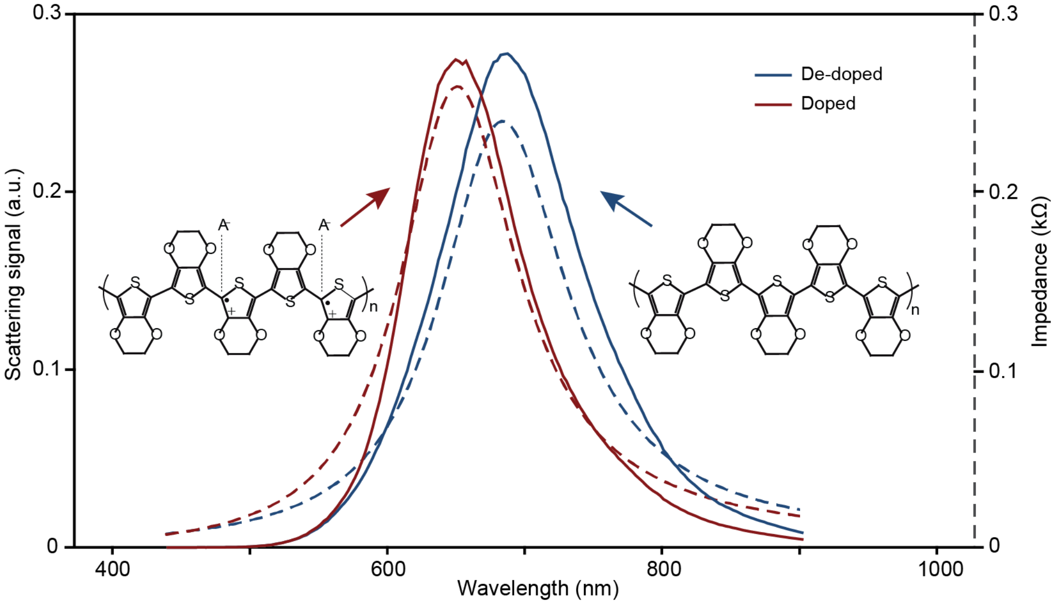

Figure 3.9: Far-field response of the electro-plasmonic nanoantenna to the doping state of electrochromic load. Electrochromic switching of the load from the doped (red curve) to the de-doped (blue curve) state leads to red shifting of the plasmonic resonance. FDTD stimulations (solid curves) and lumped nanocircuit model (dashed curves) are compared. The inset depicts the chemical structure of PEDOT for the doped (left) and de-doped (right) state. A^{-} represents the counterions.

detect the electrophysiological activity of excitable cells. To optimize the temporal response of our electro-plasmonic nanoantenna, we first evaluated the electrochemical characteristics of (Au) electrode-PEDOT: PSS system. To determine the RC time constants, the (Au) electrode-PEDOT:PSS system is mapped to an equivalent circuit model (Figure 3.10a) consisting of solution resistance R_{sol}, PEDOT:PSS layer electronic bulk capacitance C_{PEDOT}, finite-length Warburg diffusion impedance $Z_{Warburg}$, charge transfer resistance R_{CT}, and a constant phase element Z_{CPE}. $Z_{Warburg}$ is controlled by the diffusional time constant τ_D and the diffusional pseudo-capacitance C_D (Materials and Methods). We performed EIS measurements to obtain electrochemical circuit parameters and demonstrated an excellent agreement in between our circuit model and electrochemical measurements for a broad frequency range spanning from 1 Hz to 10 kHz (Figure 3.10c, Figure 3.10d and Table 3.1). Our analysis reveals that the capacitance of the PEDOT:PSS layer dominates impedance characteristics of the electrode-PEDOT:PSS system (Table 3.1-top). Decreasing surface area reduces the diffusional pseudo-capacitance (C_D)

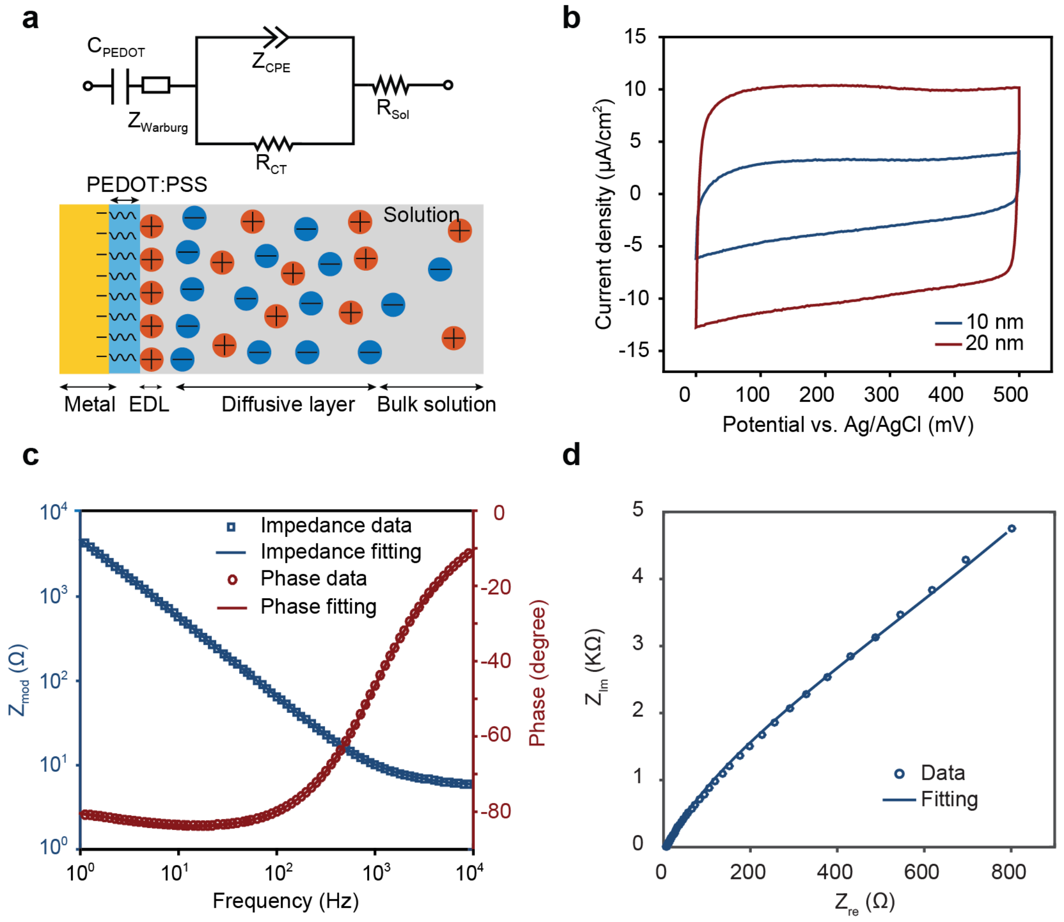

Figure 3.10: Electrochromic loading. (a) Equivalent circuit model of the (Au) electrode-PEDOT: PSS system used in EIS measurement (top). PEDOT: PSS layer electropolymerized on an Au surface is illustrated in an electrolyte solution (bottom) (b) Cyclic voltammograms of 10 nm (blue curve) and 20 nm (red curve) thick PEDOT: PSS coated Au electrodes. (c) Bode impedance plot of the (Au) electrode-PEDOT: PSS system. Excellent agreement is observed between EIS measurements and equivalent circuit model. (d) Nyquist plot for (Au) electrode-PEDOT: PSS system. We have applied an ac voltage $E_{ac} = 10$ mV (rms), and dc voltage $E_{dc} = 200$ mV versus Ag/AgCl (frequency range = 1 Hz -10 kHz) for EIS measurements. PEDOT: PSS thickness is 10 nm and area is $49\ mm^2$.

and PEDOT:PSS electronic bulk capacitance (C_{PEDOT}), which control the temporal response of the (Au) electrode-PEDOT:PSS system (Table 3.1-top); small surface area PEDOT:PSS films respond to voltage changes much faster than the larger area ones. Similarly, our circuit model predicts faster switching times with thinner PEDOT: PSS load. As shown in our EIS measurements (Table 3.1-bottom), this observation is associated to faster RC circuit response times due

Table 3.1: The numerical fitting results of equivalent circuit components of PEDOT coated electrodes: Bottom: $\sqrt{Area} = 13$ mm Top: 20 nm thick PEDOT.

PEDOT layer area vs. capacitances with fixed area				
$\sqrt{Area}$ (mm)	$Z_{Warburg}$		C_{PEDOT} (mF)	C_D (mF)
	$Y_o\left(S.\sec^{0.5}\right)$	$\sqrt{\tau_D}$ ($\sec^{0.5}$)		
3	59.09×10^{-3}	0.016	0.096	0.945
7	80.89×10^{-3}	0.028	0.13	2.26
PEDOT layer area vs. capacitances with fixed thickness				
Thickness (nm)	$Z_{Warburg}$		C_{PEDOT} (mF)	C_D (mF)
	$Y_o\left(S.\sec^{0.5}\right)$	$\sqrt{\tau_D}$ ($\sec^{0.5}$)		
10	7.390×10^{-3}	0.024	0.054	0.177
20	80.89×10^{-3}	0.028	0.13	2.26

to the drastically lower diffusional pseudo-capacitance of the thinner (10 nm) PEDOT:PSS film ($C_D = 0.177$ mF). A significantly higher diffusional pseudo-capacitance ($C_D = 2.26$ mF) is observed for thicker films (20 nm). Subsequently, we performed potential step voltammetry (PSV) measurements to determine the response times for varying thicknesses of PEDOT: PSS load and surface areas of electrode-PEDOT:PSS system. A step voltage ($+500$ mV versus $Ag/AgCl$to $+100$ mV versus $Ag/AgCl$) is used in these experiments. The response time is calculated from the recorded electrical current. It is defined as the time during which current falls to 37 % of its maximum value. In agreement with our circuit model predictions, linear scaling of the switching time with the active area of the electrode-PEDOT: PSS system is shown for fixed thickness (20 nm) PEDOT: PSS load (Figure 3.11, blue curve). Similarly, for a fixed area ($\sqrt{Area} = 7$ mm) electrode-PEDOT: PSS system, we observed that the electrochromic response time is linearly proportional with electrochromic load thickness (Figure 3.11, red curve). Accordingly, our electrochemical impedance analysis demonstrates that the temporal response of the PEDOT:PSS load can be drastically improved with lateral and vertical down scaling.

Following our electrochemical analysis, to achieve high-speed electrophysiological signal detection, we developed a selective electropolymerization technique enabling us to coat Au nanoantenna with ultrathin and conformal PEDOT:PSS polymer at nanoscale dimensions. A three-electrode glass cell system is employed under potentiostatic conditions using an aque-

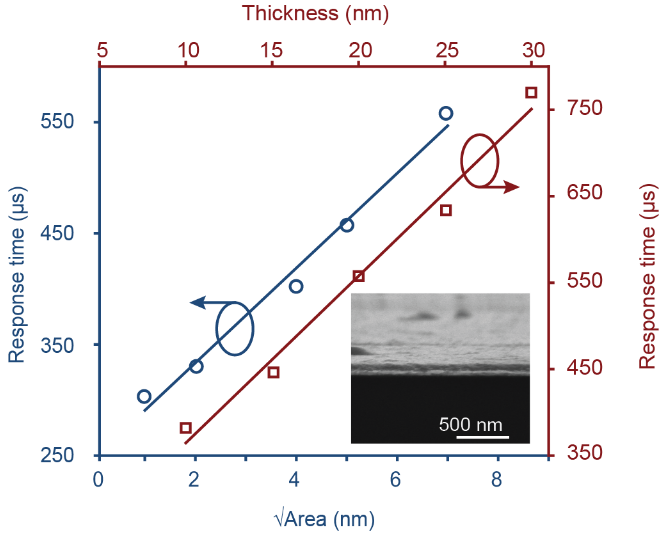

Figure 3.11: Response time of electrochromic load. Potential step voltammetry measurements to analyze the temporal response of the PEDOT: PSS film. Linear scaling of the electrochromic switching speed with the active area for fixed thickness $t = 20$ nm (blue curve) and thickness for fixed area $\sqrt{Area} = 7$ mm (red curve) is shown. Our electrochemical analysis suggests that it is advantageous to use a thinner and smaller surface area PEDOT: PSS load to achieve fast response times. .

ous solvent of 10 mM EDOT monomer and 0.1 M NaPSS (Materials and Methods). First, the nucleation potentials for the electropolymerization process are determined for the gold (Figure3.12, red curve) and ITO (Figure 3.12, blue curve) surfaces with CV measurements (scan rate: 50 mV/s). As shown in Figure 3.12 (left inset), no electropolymerization is observed for voltages below 675 mV. For voltages between 675 mV to 780 mV, polymerization initiates from the Au surface. In Figure 3.12 (middle inset), an SEM image demonstrating selective electrodeposition of PEDOT: PSS at 760 mV is shown. For electrodeposition voltages above 780 mV, both gold nanoantenna and ITO substrate are coated with PEDOT: PSS. In agreement with our CV measurements, non-selective electropolymerization is observed at a deposition voltage of 810 mV (Figure 3.12, right inset). Following an iterative procedure consisting of CV measurements and SEM imaging, we optimized our selective PEDOT: PSS loading technique and demonstrated reliable and conformal electro-deposition of ultrathin PEDOT films (down to 10 nm) with ultra-small footprint ($\sim 0.01\ \mu\text{m}^2$).

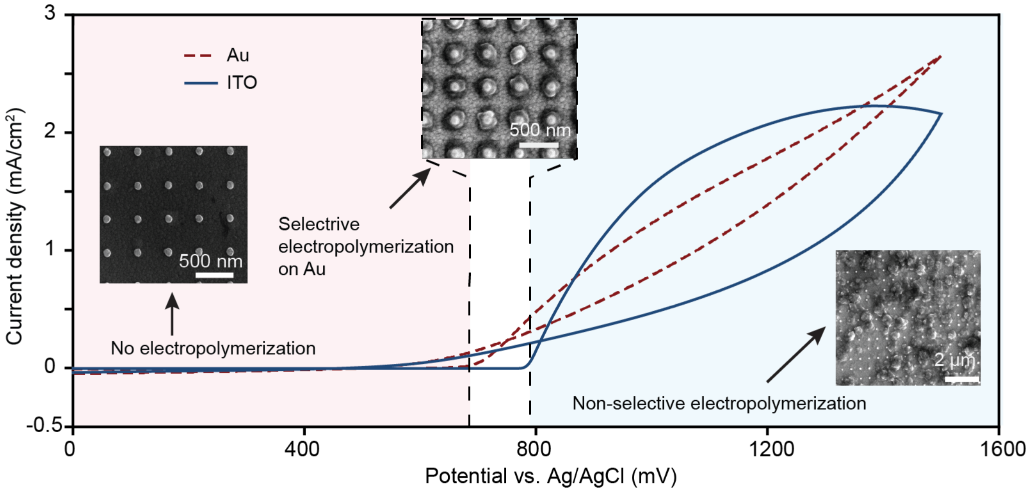

Figure 3.12: Selective deposition of electrochromic load. Selective electropolymerization of 3,4-ethylenedioxythiophene (EDOT) monomer in sodium poly(styrenesulfonate) (NaPSS) aqueous solution under potentiostatic conditions. First, cyclic voltammetry (CV) is used to characterize electropolymerization of PEDOT: PSS on Au (red curve) and ITO (blue curve) substrates. The nucleation point difference between Au and ITO surfaces is exploited for selective deposition of PEDOT: PSS on Au nanoantenna (insets).

3.2.3 Ultrasensitive electric-field detection

During a cellular firing event, membrane potential of an electrogenic cell (e.g. neurons or cardiomyocytes) experiences significant fluctuations as a result of Na^+ influx into the cell (spike phase) and K^+ efflux from the cell (repolarization phase). Such charge density (ion concentration) perturbations could give rise to strong transient electric fields. Field values as high as (10 mV/nm) are observed across membrane layers [276], while two to three orders of magnitude lower values (10^{-2} mV/nm -10^{-1} mV/nm) are detected in the extracellular environment and within the synaptic regions with extremely small ion currents ($\sim$ 10 pA) [277]. To determine field sensitivity of our electro-plasmonic nanoantenna, we performed electro-optic measurements with controlled electric-fields generated through a transparent counter electrode (Figure 3.13). For our sensitivity tests, we used a relatively low electric-field range (10^{-2} mV/nm to (10^{-1} mV/nm) that is comparable to the extracellular fields generated during electrogenic cell firing events [277]. Intensity-based scattering measurements are obtained in transmission configuration using a laser beam that is focused to a diffraction limited spot with an extra-long working-distance objective (Figure 3.4). Laser diode is modulated at a frequency of

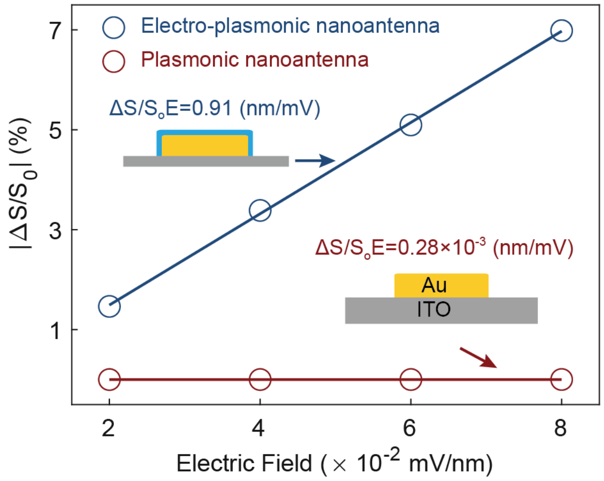

Figure 3.13: Field sensitivity of active plasmonic nanoantenna. Differential scattering signal versus applied electric-field strength. Electro-optic measurements are performed at a modulation frequency of 500 Hz. Absolute values of the differential scattering signals are compared for the pristine (red curve) and electro-plasmonic (blue curve) nanoantennas. times enhanced field sensitivity is shown for the electro-plasmonic nanoantenna. For low field values (2×10^{-2} mV/nm to 8×10^{-2} mV/nm), we observed large intensity changes (1-7 %) in scattering signal of the electro-plasmonic nanoantenna.

500 Hz, and the scattered light from the electro-plasmonic nanoantenna is detected with an amplified photodetector connected to a lock-in amplifier (Figure 3.4). In our experiments comparing pristine and loaded nanoantennas, the zero-bias scattering signal (S_o) and the electric-field modulated change in the scattering signal ($\triangle S$) are monitored to obtain differential scattering signals ($(\triangle S)/S_o$). For the pristine nanoantenna, the differential scattering signal is shown to increase linearly with applied electric field, at a rate of $(\triangle S)/S_o)_P = 0.28 \times 10^{-2}$ nm/mV in agreement with previous experimental studies [55]. Remarkably, we demonstrated $\sim 3.25 \times 10^3$ fold enhanced sensitivity of $(\triangle S)/S_o)_{EP} = 0.91$ nm/mV for the electro-plasmonic nanoantenna. The high field sensitivities of our electro-plasmonic nanoantenna also compare favorably with those of quantum dot (QD) electric-field probes that has been recently used for monitoring the electrophysiological activity of neural cells [260]. Using the electro-plasmonic nanoantenna, we demonstrated substantially large scattering intensity changes of ~ 7 % for low field values of 8×10^{-2} mV/nm. QDs utilizing quantum-confined Stark effect, on the other hand, provide ~ 11 % change in photoluminescence signals for an applied field of 10 mV/nm, a field sensitivity that is nearly two orders of magnitude lower than that of electro-plasmonic nanoan-

tenna [260, 261, 278].

3.2.4 Analytical model of field-effect active plasmonic nanoantenna

To gain insight for drastically enhanced electric-field sensitivity with PEDOT: PSS loading, in the following we developed an analytical model of the active plasmonic nanoantenna using quasi-static approximation.

3.2.4.1 Pristine plasmonic nanoantenna

An external electric field impinged on a noble metal can repel (attract) the free electrons and create a very narrow strip of depletion (excess charge) region at the metal-dielectric boundary. This free carrier modulated zone, extent of which is determined by the Thomas-Fermi screening length, controls the effective dielectric permittivity of the localized surface plasmons (LSPs). Using a quasi-static model, we can find an analytical relation for the plasma frequency modulation as a result of this external electric-field. Induced charges on the gold surface should screen the external electric-field

$$\Delta\sigma = -\varepsilon_0 E \tag{3.2}$$

where E is the external electric-field acting on the plasmonic voltage probe. The corresponding modulation in electron density ΔN_{Au} is

$$\Delta N_{Au} = -\frac{\Delta\sigma}{e d_{TF}^{Au}} \tag{3.3}$$

where d_{TF}^{Au} is the Thomas-Fermi screening length in gold. The plasma frequency of gold surface

$$\omega_p = \sqrt{\frac{e^2 N_{Au}}{\varepsilon_o m}} \tag{3.4}$$

will alter as a result of electron density change. A linear relationship in between charge density variation and plasma frequency modulation can be established

$$\Delta\omega_p = \frac{\omega_p}{2N_{Au}} \Delta N_{Au} \tag{3.5}$$

Dielectric function of gold is described by the Drude's model

$$\varepsilon(\omega) = \varepsilon_\infty - \frac{\omega_p^2}{\omega(\omega + i\gamma)} \tag{3.6}$$

where ε_∞ is the relative permittivity at the high-frequency limit and γ is the damping coefficient. Within the quasi-static model, polarizability of a pristine nanoantenna is given by

$$\alpha = V \frac{\varepsilon(\omega) - \varepsilon_D}{L\left[\varepsilon(\omega) - \varepsilon_D\right] + \varepsilon_D} \tag{3.7}$$

where L is a geometrical factor [28], and ε_D is the real part of surrounding medium dielectric constant. Resonance occurs when the polarizability is maximum (

$$L\left[\mathrm{Re}\left(\varepsilon(\omega)\right) - \varepsilon_D\right] + \varepsilon_D = 0$$

). Combining equation (3.5) with this resonance condition,

$$\frac{\varepsilon_D(L-1)}{L} = \mathrm{Re}\left[\varepsilon(\omega_{LSP})\right] = \varepsilon_\infty - \frac{\omega_p^2}{\omega_{LSP}^2 + \gamma^2} \tag{3.8}$$

resonance frequency (ω_{LSP}) of the plasmonic nanoantenna can be found as

$$\omega_{LSP} = \sqrt{\frac{\omega_p^2}{\varepsilon_\infty + \varepsilon_D\left(\frac{1-L}{L}\right)} - \gamma^2} \tag{3.9}$$

Resonance frequency modulation ($\Delta\omega_{LSP}$) due to the changes in plasma frequency of the gold surface is given as

$$\Delta\omega_{LSP} = \frac{\omega_p}{\omega_{LSP}\left(\varepsilon_\infty + \varepsilon_D\left(\frac{1-L}{L}\right)\right)} \Delta\omega_p \tag{3.10}$$

Combining equations (3.2-3.3), (3.5) and (3.10), resonance wavelength shift

$$\Delta\lambda = -\left(\lambda^2/2\pi c\right)\Delta\omega$$

can be expressed as

$$\Delta\lambda_{LSP}^p = -\frac{\varepsilon_o \omega_p^2 \lambda_{LSP}^3}{8\pi^2 c^2 e N d_{TF}^{Au}\left(\varepsilon_\infty + \varepsilon_D\left(\frac{1-L}{L}\right)\right)} E \tag{3.11}$$

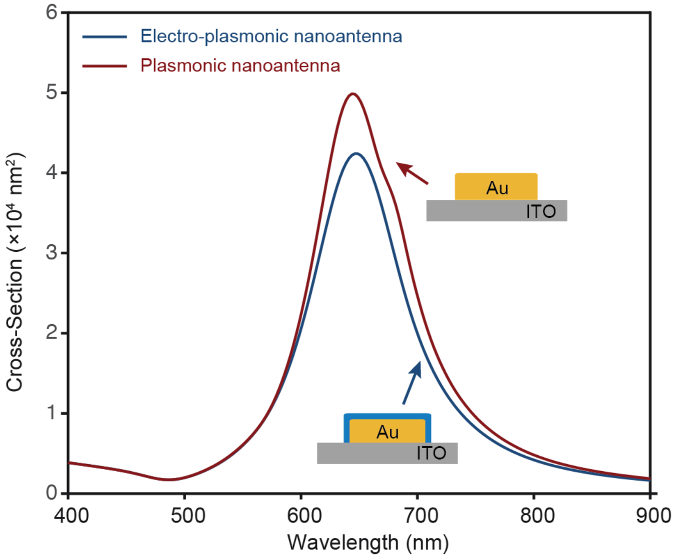

Figure 3.14: Scattering spectra of pristine and electro-plasmonic nanoantenna. Scattering spectra of plasmonic (red curve) and electro-plasmonic (blue curve) nanoantenna are compared using FDTD simulations. A metallic disk shape nanoantenna with 90 nm diameter and 45 nm thickness, and 20 nm thick conformally coated (doped) PEDOT polymer layer are assumed.

In agreement with experimental measurements (Figure 3.13, red line), a linear relationship between resonance wavelength shift and electric-field strength is obtained for the pristine nanoantenna. Negative sign highlights the blue shift of the scattering spectrum as a result of stiffening of the resonant free electron spring (plasma frequency of the metal).

3.2.4.2 Electro-plasmonic nanoantenna response to electric-field

Resonance frequency modulation of the electro-plasmonic nanoantenna is due to the variations in the dielectric constant ($\varepsilon_D = \varepsilon_{PEDOT}$) of the electrochromic load with external field. The electric-field controlled dielectric permittivity of the electrochromic load couples the low-frequency local electric field dynamics ($<$ 1 kHz) to high-frequency (few hundred THz) electromagnetic resonances. Following equation 3.9, this modulation can be written as

$$\Delta\omega_{LSP} = -\frac{\omega_p^2}{2\omega_{LSP}} \times \frac{\left(\frac{1-L}{L}\right)}{\left(\varepsilon_\infty + \varepsilon_{PEDOT}\left(\frac{1-L}{L}\right)\right)^2}\Delta\varepsilon_D \tag{3.12}$$

Here, we assume that the PEDOT: PSS layer is conformal and thick enough to completely enclose the plasmonic enhanced near-field regions around the metallic nanoantenna. Accordingly, resonance wavelength shift $\Delta\lambda = -\left(\lambda^2/2\pi c\right)\Delta\omega$ is given as

$$\Delta\lambda_{LSP}^{EP} = \frac{\omega_p^2\lambda_{LSP}^3}{8\pi^2c^2}\left(\frac{\left(\frac{1-L}{L}\right)}{\left(\varepsilon_\infty + \varepsilon_{PEDOT}\left(\frac{1-L}{L}\right)\right)^2}\right)\Delta\varepsilon_{PEDOT} \tag{3.13}$$

here, the electrochromic modulation can be described using frequency-dependent permittivity of the electrochromic load, which follows the Drude model [279, 280]

$$\varepsilon_{PEDOT}(\omega) = \varepsilon_{\infty,PEDOT} - \frac{\omega_{p,PEDOT}^2}{\omega^2 + i\gamma_{PEDOT}\omega} \tag{3.14}$$

where $\omega_{p,PEDOT}$ is the bulk plasma frequency, $\varepsilon_{\infty,PEDOT}$ is the relative permittivity at the high-frequency limit and γ_{PEDOT} is the damping coefficient. Real part of the PEDOT:PSS dielectric constant

$$\varepsilon_{PEDOT}^{re} = \varepsilon_{\infty,PEDOT} - \frac{\omega_{p,PEDOT}^2}{\gamma_{PEDOT}^2 + \omega^2} \tag{3.15}$$

is modulated as result of the varying plasma frequency

$$\Delta\varepsilon_{PEDOT}^{re} = -\frac{2\omega_{p,\ PEDOT}}{\gamma_{PEDOT}^2 + \omega^2}\Delta\omega_{p,PEDOT} \tag{3.16}$$

A similar analysis used above for the gold surface (Eqs. 3.2-3.4) leads to a linear relationship between the plasma frequency modulation and the charge density variation for the PEDOT: PSS load

$$\Delta\omega_{p,PEDOT} = \frac{\omega_{p,PEDOT}}{2N_{PEDOT}}\left(\frac{\varepsilon_0}{ed_{TF}^{PEDOT}}\right)E \tag{3.17}$$

where $\left(\varepsilon_0/ed_{TF}^{PEDOT}\right)E$ is the induced charge density ΔN_{PEDOT}. The plasma frequency and linear modulation of the dielectric permittivity with electric-field dictate linear relationship between differential signal change and local electric-field strength, a crucial characteristic needed for quantitative detection of local electric field strength. Combining equations (3.13) and (3.16) -(3.17) resonance wavelength shift for the electro-plasmonic nanoantenna is given as

$$\Delta\lambda_{LSP}^{EP} = \frac{\omega_p^2\lambda_{LSP}^3}{8\pi^2c^2}\left(\frac{\left(\frac{1-L}{L}\right)}{\left(\varepsilon_\infty+\varepsilon_{PEDOT}\left(\frac{1-L}{L}\right)\right)^2}\right)\frac{\omega_{p,PEDOT}^2}{\gamma_{PEDOT}^2+\omega^2}\left(\frac{\varepsilon_0}{N_{PEDOT}ed_{TF}^{PEDOT}}\right)E \tag{3.18}$$

In agreement with experimental measurements performed (Figure 3.13, blue line), our model demonstrates a linear relationship between resonance wavelength shift and the strength of the impinging external electric-field. In addition, our quasi-static model explains the experimentally observed reversal of wavelength shift in response to electric field for the pristine and electro-plasmonic nanoantennas as in equations 3.11 and 3.18.

3.2.4.3 Sensitivity enhancement with electrochromic loading

Spectral shifting of nanoantenna resonance with $\Delta\lambda$ leads to a differential scattering signal

$$\frac{\Delta S}{S_o} = -\frac{1}{1-T_o}\left(\frac{\Delta T}{\Delta\lambda}\right)\Delta\lambda \tag{3.19}$$

where $S_0 = 1 - T_0$ is the scattered signal, $\Delta S = -\left(\Delta T/\Delta\lambda\right)\Delta\lambda$ is the change in scattered light intensity, T_0 is the transmitted signal, and $\Delta T/\Delta\lambda$ is the derivative of the transmission spectrum. For both pristine and electro-plasmonic nanoantennas, the impact of electric field on the transmission spectrum can be described as a uniform shifting of the spectral resonance profile. Furthermore, as our FDTD analysis shows (Figure 3.9), $\Delta T/\Delta\lambda$ of the plasmonic resonance profile is nearly identical for pristine and electro-plasmonic nanoantennas. Combining equations (3.11), (3.18) and (3.19), the enhancement of the differential scattering signal with electrochromic loading can be written as

$$\frac{\Delta S/S_o{}^{EP}}{\Delta S/S_o{}^{P}} = \frac{\Delta\lambda_{LSP}^{EP}}{\Delta\lambda_{LSP}^{P}} = -\frac{\left(\frac{1-L}{L}\right)\left(\varepsilon_\infty+\varepsilon_D\left(\frac{1-L}{L}\right)\right)}{\left(\varepsilon_\infty+\varepsilon_{PEDOT}\left(\frac{1-L}{L}\right)\right)^2}\frac{\omega_{p,PEDOT}^2}{\gamma_{PEDOT}^2+\omega^2}\left(\frac{N_{Au}d_{TF}^{Au}}{N_{PEDOT}d_{TF}^{PEDOT}}\right) \tag{3.20}$$

Here, the enhancement factor is independent from the external electric-field strength following equations (3.11) and (3.20), Thomas-Fermi screening length is defined as $d_{TF} = 1/2\left(a_0^3/N\right)^{1/6}$, where $a_o = 5.29\times10^{-11}$ m Bohr radius and N is the electron density of the conducting medium under consideration. Hence, improvement in differential signal sensitivity to the electric-field strength is defined as

$$\frac{(\Delta S/S_oE\ )^{EP}}{(\Delta S/S_oE\ )^{P}} = -\frac{\left(\frac{1-L}{L}\right)\left(\varepsilon_\infty + \varepsilon_D\left(\frac{1-L}{L}\right)\right)}{\left(\varepsilon_\infty + \varepsilon_{PEDOT}\left(\frac{1-L}{L}\right)\right)^2}\frac{\omega_{p,PEDOT}^2}{\gamma_{PEDOT}^2 + \omega_{LSP}^2}\left(\frac{N_{Au}}{N_{PEDOT}}\right)^{\frac{5}{6}} \tag{3.21}$$

and PEDOT: PSS electron densities ($5.3 \times 10^{18} cm^{-3}$) [208].

$$\left|\frac{\Delta S/S_oE^{\ EP}}{\Delta S/S_oE^{\ P}}\right| \approx \left(\frac{N_{Au}}{N_{PEDOT}}\right)^{\frac{5}{6}} = 3.66 \times 10^3 \tag{3.22}$$

The calculated enhancement factor with electrochromic loading is in strong agreement with the observed values

$$\left|(\Delta S/S_oE\ )^{EP}/(\Delta S/S_oE\ )^{P}\ \right| \approx 3.25 \times 10^3 \tag{3.23}$$

in our experiments (Figure 3.13).

3.2.5 High SSNR recordings with single electro-plasmonic nanoantenna

The fundamental limit to any optical measurement technique is the shot noise. SSNR is proportional to the ratio of signal change, ΔS , and the baseline shot noise $S_o/\sqrt{N_{ph}}$, where Nph is the number of photons detected): SSNR$\sim$ $(\Delta S/S_o\ )\sqrt{N_{ph}}$. Hence, high field sensitivity ($\Delta S/S_oE$) probes providing high photon-counts (Nph) are needed to achieve reliable measurement of the electric-field dynamics with light. Typically, a small number of photons are detected from small structures, such as fluorescence molecules and QD field probes. In contrast, localized surface plasmon (LSP) mediated light scattering from electro-plasmonic nanoantenna leads to orders of magnitude higher photon-counts. Plasmon enhanced cross-sections of our electro-plasmonic nanoprobes are $\sim 3.6 \times 10^4$ nm^2 compared to typical values of $\sim 10^{-2}$nm^2 for GEVIs and ~ 1 nm^2 for QDs [261, 278].

3.2.6 SSNRs obtained using a single electro-plasmonic nanoantenna

The signal-to-shot-noise ratio (SSNR) is defined as the ratio of the signal change, ΔS, and the baseline shot noise, $S_o/\sqrt{N_{ph}}$

$$SSNR = \frac{\Delta S}{S_0}\sqrt{N_{ph}} \tag{3.24}$$

where N_{ph} is the number of photons. Assuming isotropic scattering from electro-plasmonic antenna, the detected signal $S_o = N_{ph}$ (photon-count) can be expressed as

$$S_0 = QE\left[\eta_{collection}T\right]P_{sca}t_{\text{int}}\left(\frac{\lambda}{hc}\right) \tag{3.25}$$

where P_{sca} is the scattered light power, $\eta_{collection}$ collection is the solid angle fraction of the total scattered light collected by the microscope objective, T is the transmittance of the objective lens at the scattering wavelength, QE is the quantum efficiency of the photodetector at the scattering wavelength, c is the speed of light, h is Planck's constant, and λ is the wavelength, and t_{int} is the integration time. $\eta_{collection}$, the solid angle fraction of the total scattered light collected by the microscope objective, is given by [281]

$$\eta_{collection} = \frac{1}{2}\left(1 - \sqrt{1 - \left(\frac{NA}{n_{coup}}\right)^2}\right) \tag{3.26}$$

where NA is the numerical aperture of the objective, and n_{coup} is the refractive index of the objective lens coupling medium. The scattered power is

$$P_{sca} = I_{inc}\left(Q_{sca}\pi r^2\right) \tag{3.27}$$

where I_{inc} is the incident light intensity, $Qsca$ is the scattering efficiency (calculated using FDTD simulations as shown in Figure 3.14), and r is the radius of the electro-plasmonic nanoantenna. Using equation (3.24)-(3.27), the signal can be calculated

$$S_0 = QE\left(\eta_{collection}T\right)I_{inc}\left(Q_{scat}\pi r^2\right)t_{\text{int}}\left(\frac{\lambda}{hc}\right) \tag{3.28}$$

Change in detected light signal (photon-count) with applied electric-field is given by

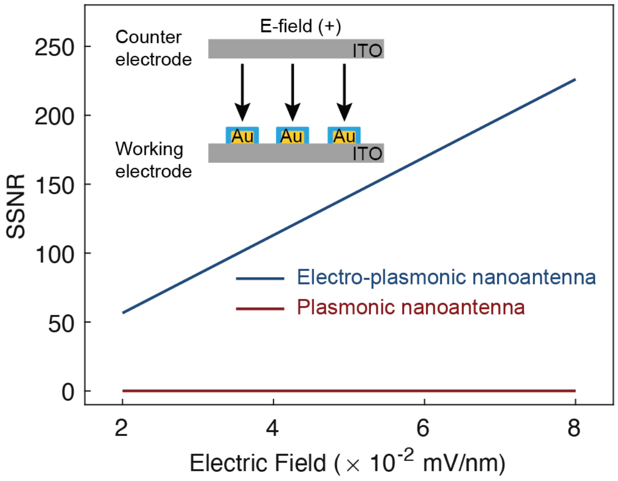

Figure 3.15: Detection limits of single electro-plasmonic and plasmonic nanoantennas. SSNR ratios are compared for single field probes at an illumination intensity of 3 μW/μm^2. An integration time of 1 ms is considered. High SSNRs ($\sim 60-220$) are shown for the electro-plasmonic nanoantenna even for low field values (2×10^{-2} mV/mm -8 $\times 10^{-2}$ mV/nm). Reference field direction corresponding to positive electric field is shown (inset).

$$\Delta S = S_0 \left(\frac{\Delta S}{S_0 E}\right)^{EP} E \tag{3.29}$$

where $(\Delta S/S_o E\ )^{EP}$ is the rate of differential scattering signal change with electric-field for the electro-plasmonic voltage probe, E is the local electric-field acting on electro-plasmonic nanoantenna. Following equation (3.27), the signal change can be rewritten as

$$\Delta S = QE\left[\eta_{collection} T\right] I_{inc} \left(Q_{scat} \pi r^2\right) t_{\text{int}} \left(\frac{\lambda}{hc}\right) \left(\frac{\Delta S}{S_0 E}\right)^{EP} E \tag{3.30}$$

Combining equations. (3.27) and (3.30), the signal-to-shot-noise ratio (SSNR) is found as

$$SSNR = \frac{\Delta S}{S_0}\sqrt{N_{ph}} = \sqrt{QE\left[\eta_{collection} T\right] I_{inc} \left(Q_{scat} \pi r^2\right) t_{\text{int}} \left(\frac{\lambda}{hc}\right)} \left(\frac{\Delta S}{S_0 E}\right)^{EP} E \tag{3.31}$$

We calculated SSNRs for our electro-plasmonic nanoantenna for varying electric-field strengths. In our calculations, we used our experimentally obtained differential signal values,

Table 3.2: Parameters used in the signal-to-shot-noise ratio (SSNR) calculations.

Parameter	Description	value	units
I_{inc}	Incident Intensity	3	μW/μm^2
t_{int}	Integration time	1	ms
NA	Numerical aperture	0.45	
n_{coup}	Dry objective coupling	1	
$T.QE$	Quantum efficiency combined with the transmission efficiency	0.5	
$Q_{sca,EP}$	Scattering efficiency of electro-plasmonic antenna	5.6	
$Q_{sca,P}$	Scattering efficiency of plasmonic antenna	6.3	

typical light intensities (3 μW/μm^2 used in flouresence measurements and scattering cross-sections obtained from our FDTD simulations (Figure 3.14). Parameters used in Eq. (3.31) for SSNR calculations are summarized in Table 3.2. As shown in Figure 3.15 (blue curve), a single electro-plasmonic antenna enables optical detection of local field dynamics at 1 kHz with a remarkably high SSNRs of $\sim$ 60 to 220 for low field values of 2×10^{-2} mV/mm -8×10^{-2} mV/nm. This high SSNR measurement capability, outperforming whole cell-body voltage sensitive fluorescence measurements [75], paves the way to extracellular voltage measurements from diffraction limited spots. Further improvements in photon counts and SSNRs can be achieved by packing higher number of electro-plasmonic nanoantenna within a diffraction limited spot size. Our SSNR calculations also reveal the strong contribution of electrochromic load for reliable detection of electrical signals with light. As shown in Figure 3.15 (red curve), with conventional plasmonic nanoantennas, SSNRs are far below the theoretical detection limits (SSNR < 0.1) preventing reliable measurement of electric-field dynamics with high spatial resolution.

3.2.7 High-bandwidth opto-electrochemical detection

We determined the optical response times of our electro-plasmonic through in-situ opto-electrochemical testing using a custom-built three-electrode electrochemical cell. In our measurements, electro-plasmonic nanoantenna substrate is employed as the working electrode. We obtained the far-field scattering signal of the electro-plasmonic nanoantenna using a dark-field transmission set up illustrated in Figure 3.16a. Here, the high (NA $0.8-0.95$) condenser is used for sample illumination through a hollow cone. The low NA objective ($20\times$, NA 0.45) is designed to collect only the scattered light, which is continuously recorded with an amplified photodetector at a gain (Hi-Z) 4.75×10^6 V/A ±5 %. To obtain the temporal response of the

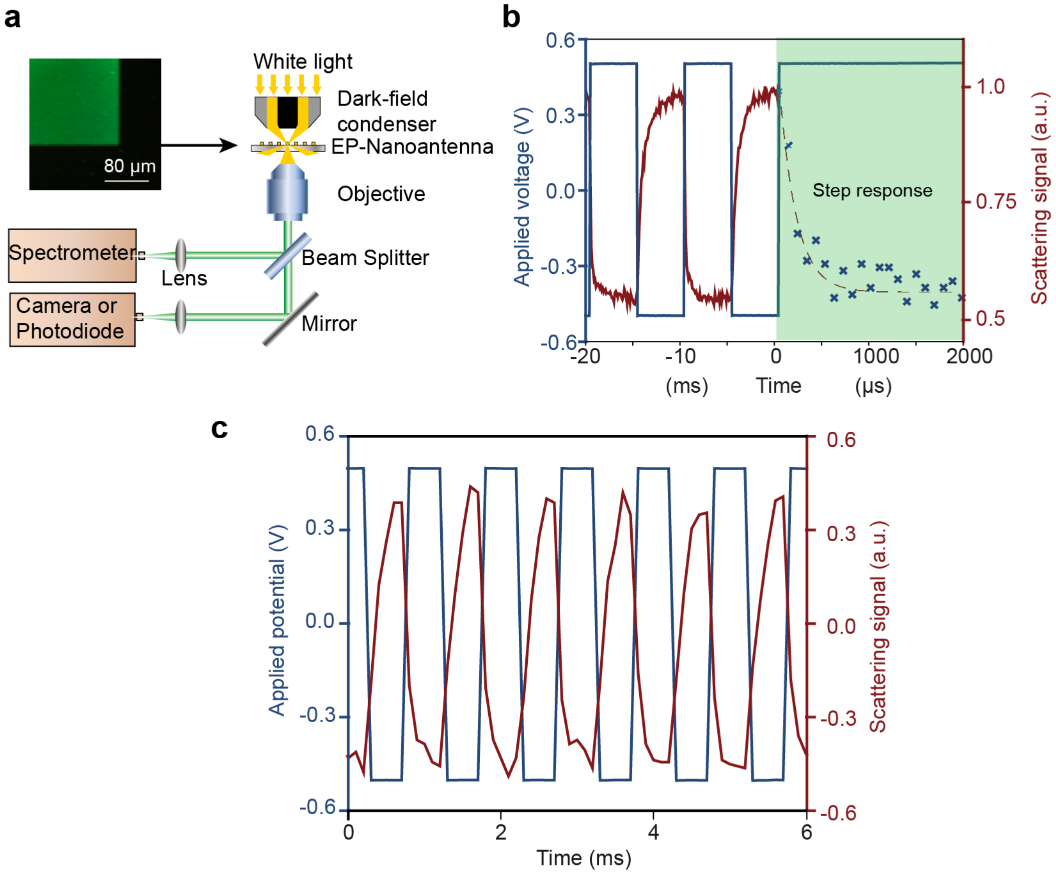

Figure 3.16: Dynamic response of electro-plasmonic nanoantenna. (a) Schematics of the transmission dark-field measurement setup. Strong light scattering contrast in between the spatial regions with (green) and without (dark) electro-plasmonic nanoantenna is observed (inset). (b) Temporal response of the electro-plasmonic nanoantenna obtained using a square wave voltage for spectroelectrochemical recording. Optical response of the electro-plasmonic nanoantenna is shown (red curve) for potential steps (blue curve) in between -500 mV (versus $Ag/AgCl$) and 500 mV (versus $Ag/AgCl$) with a residence time of 5 ms. A switching time of 191 μs is obtained after fitting a decaying-exponential function to the scattered light intensity. (c) Optical scattering signal obtained from a PEDOT: PSS coated plasmonic nanoantenna array modulated by a square wave of ± 500 mV versus $Ag/AgCl$ with a frequency of 1 kHz. Data acquired using a silicon (Si) amplified photodetector 4.75×10^6 V/A ± 5 % .

electro-plasmonic nanoantenna, a square wave voltage (-500 mV to 500 mV, 100 Hz) is applied using a potentiostat (Gamry reference 600^{TM}). Response time of our electro-plasmonic nanoantenna is determined by fitting a decaying-exponential function to the scattered optical signal. In our experiments, we demonstrated sub-millisecond response times ($\sim$ 191 μs) suf-

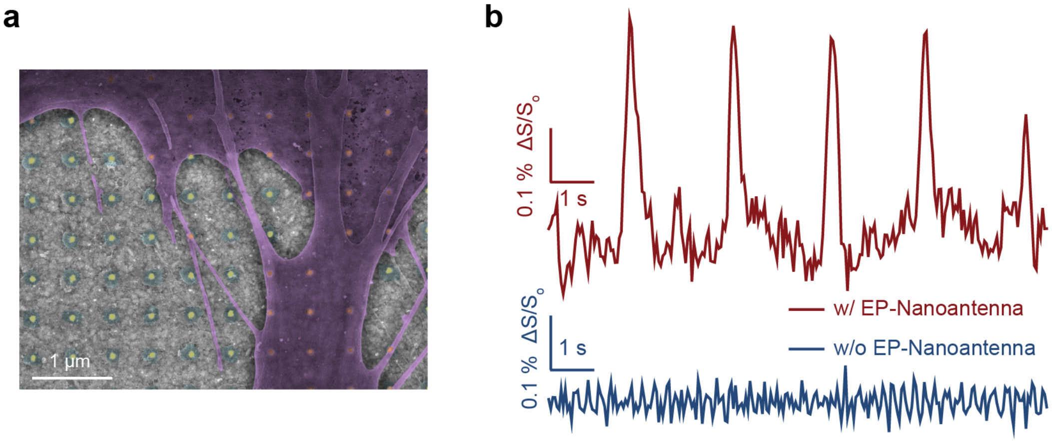

Figure 3.17: Optical recording of electrogenic activity. (a) False-color scanning electron micrograph of hiPSC derived cardiomyocytes (iCMs) (colored in purple) cultured on electro-plasmonic nanoantenna array. (b) Differential scattering signal in response to electrogenic activity of a network of cardiomyocyte cells. Strong far-field signal allowing label-free and real-time optical detection of electrogenic activity of iCMs are obtained from substrates with electro-plasmonic nanoantennas (red curve). Control measurements are performed to verify the origin of the electro-optic signal. In the absence of electro-plasmonic nanoantenna, no far-field signal is detected (blue curve).

ficient to resolve electrogenic activity of cells (Figure 3.16b). We also proved high bandwidth functionality of our electro-plasmonic nanoantenna at kilohertz frequencies (Figure 3.16c). Our in-situ opto-electrochemical experiments also confirmed the excellent stability and reversible response of ultrathin and nanoscale electrochromic load over millions of switching cycles.

3.2.8 In vitro optical detection of electrogenic signals

We demonstrated in vitro functionality of our field probes for label-free optical detection of electrophysiological activity of the excitable cells. In our experiments, stem cell derived cardiomyocytes (iCMs) are used (Materials and Methods) [269]. Before electro-optic testing, iCMs are seeded at a density of 2×10^6 cells/mL on fibronectin coated electro-plasmonic nanoantenna array (Figure 3.17a), and their electrophysiological functionality is confirmed using Ca2+ indicators (Materials and Methods, Figure 3.18). Electro-plasmonic nanoantenna ($\sim 3.6\times10^4$ nm^2 has more than few million times larger cross sections than the genetically encoded voltage indicators ($\sim 10^{-2}$ nm^2) [74]. Thus, the light intensities used in our experiments (11mW/mm^2) were $\sim 10^2 - 10^3$ times lower than the typical excitation sources used in optical experiments with fluorescence molecules [75, 259]. To assure that the optical signal is a result of electrical activity only, a myosin II inhibitor, blebbistatin (10 μM) is used [282, 283]. In our network-level experiments, the scattering signal is continuously collected using a $20\times$objective in transmission dark-field measurement configuration (Figure 3.16a) and a spectrometer (Ocean Optics, HR4000) with 50 ms integration time. Photon counts are obtained following a spectral integration method as a function of time (Figure 3.17b). Our measurements show that the electrogenic activity of spontaneously firing iCMs leads to increased light scattering (Figure 3.17, red curve). This observation is in strong agreement with our opto-electrochemical measurements as spontaneous depolarization of cardiomyocytes (Na^+ influx into the cell) results in a transient electric-field directed towards the electro-plasmonic nanoantennas (as in Figure 3.15, inset). To verify the electro-plasmonic origin of the label-free and real-time optical signal, measurements are repeated with iCMs cultured on substrates without electro-plasmonic nanoantenna. No far-field optical signal for the cellular firing events is observed in the absence of electro-plasmonic nanoantenna (Figure 3.17b, blue curve). We theoretically investigated the local temperature increase as a result of photothermal heat generation during our experiments. Our analysis shows that the temperature increase is limited (< 3 ^{o}C) and confined at the nanoscale vicinity (< 10 nm) of electro-plasmonic nanoantenna. As shown in Figure 3.6, plasmon-assisted temperature increase is too low to cause any thermal damage to cardiomyocyte cells. Furthermore, no phototoxic effect of light is observed during our experiments. Phototoxicity is an important concern for the viability of fluorescently label cells [76, 258]; fluorescence excitation always produces disruptive oxygen free-radicals [284]. Extracellular electro-plasmonic nanoantenna, on the other hand, uses a different optical signaling mechanism from fluorescence excitation. In addition, the light intensities used in our experiments are much lower than those used in fluorescence-based measurements.

3.3 Discussion

We introduced an extremely bright electro-plasmonic field probe offering ultrasensitive and label-free detection of electrical signals at kilohertz frequencies with light. To achieve this, we developed a novel electropolymerization technique enabling us to exploit biocompatible electrochromic polymer PEDOT: PSS as an electric-field controlled ultrathin and nanoscale optical load. Existing optical field probes run into signal-to-noise ratio limitations due to either

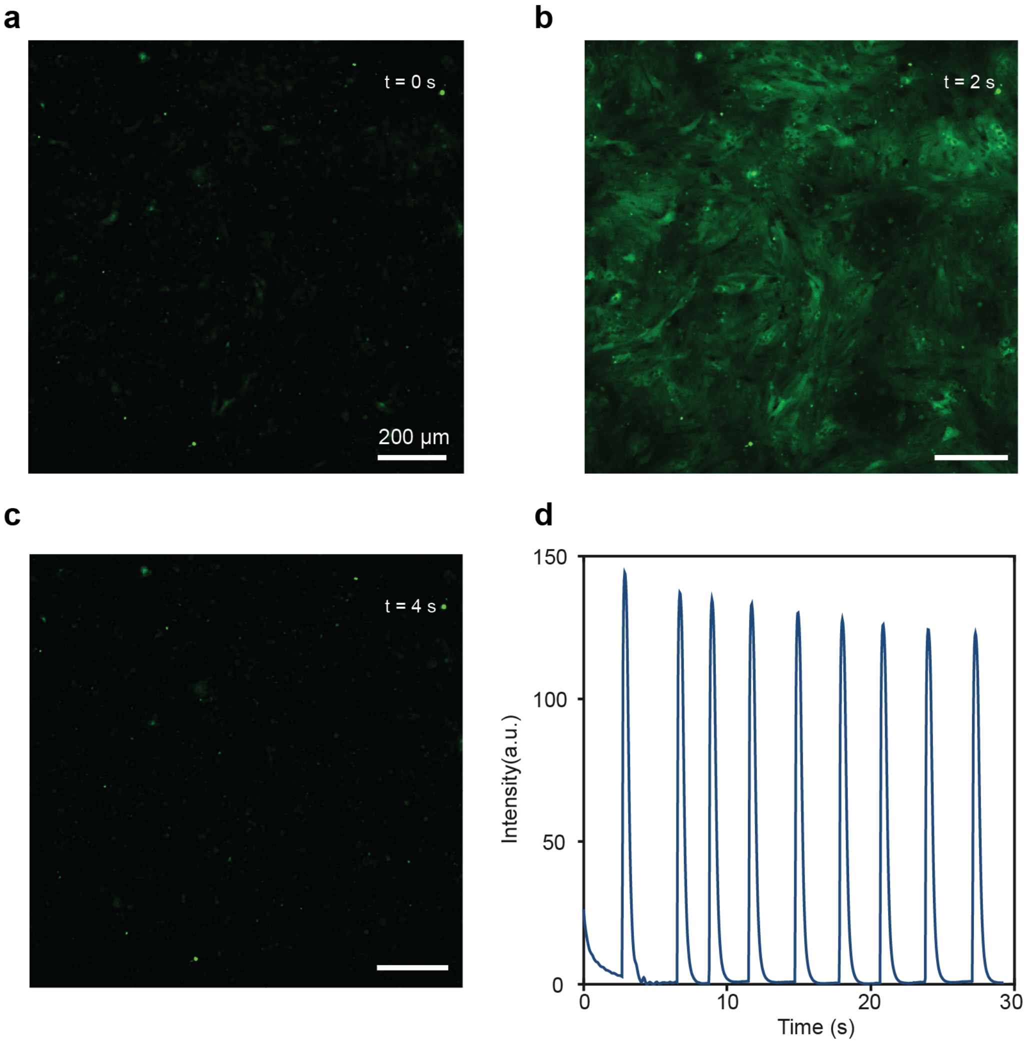

Figure 3.18: Ca^{2+} flux of iCMs captured using fast Ca^{2+} imaging.Time lapse fluorescent images of Ca^{2+} flux. (a) at $t = 0$ s. (b) $t = 2$ s. (c) $t = 4$ s. (d) Fluorescent intensity over time.
.

low photon counts (e.g., GEVIs) or low electric-field sensitivities (e.g., QDs and plasmonic nanoantenna). In our experiments, we demonstrated that electro-plasmonic nanoantenna enables optical transduction of local field dynamics with more than 3.25×10^3 times enhanced field sensitivities over conventional plasmonic nanoantennas [55] and nearly two orders of magnitude higher intensity modulations over QD field probes [260, 261]. Furthermore, enhanced cross-sections ($\sim 3.6 \times 10^4$ nm^2) of our electro-plasmonic nanoprobes are orders of magnitude larger than those of GEVIs ($\sim 10^{-2}$ nm^2) [74] and QDs (~ 1 nm^2) [261, 278]. By merging high field sensitivity and photon-counts together, we show that our electro-plasmonic probes offer remarkably high signal-to-shot-noise ratio (SSNR $\sim 60-220$) measurement capability from diffraction limited spots. Our study also includes the first practical uses of electro-plasmonic field probes for in vitro electrophysiological tests at network level. By tracking the far-field spectral response of our field probes, we demonstrated real-time label-free detection of spiking activity of cardiomyocyte cells with low-intensity light (11mW/mm^2).

Chapter 4

Nanoelectrochromic Flat Optical Modulators

Active control of optical-frequency plasmonic signals is the subject of intensive research in plasmonics [285]. Recently, there has been a strong drive to achieve this active control by combining plasmonics with electrochromic materials due to the (i) unprecedented light-matter interactions enabled by plasmonics, (ii) fast electrochemical response times of ultrathin (< 25 nm) nano-electrochromic polymers, (iii) high voltage sensitivity of the low electron density electrochromic polymers compared to the plasmonic metals [54, 67, 79–82]. A strong electro-optical interaction within a thin layer of electrochromic polymer (a few tens of nanometers) can be achieved using plasmonic hot spots, enabling faster response time due to shorter ionic diffusion time. Recent pioneering work on electro-plasmonic modulation has shown that a fast switching time of ~ 9 ms can be achieved with an optical contrast ratio of ~ 8.2 dB [79]. However, one limitation of the conventional electro-plasmonic modulator is that they harness the imaginary part of the complex effective refractive index k (extinction coefficient) instead of the real part n of the electrochromic material to achieve plasmonic resonance modulation [286]. Ability to modulate the extinction coefficient is limited by the inherent characteristics of the electrochromic polymer, setting a fundamental upper limit on achievable the modulation depth of the electro-plasmonic modulator even with plasmonic enhancement.

Here we report a new class of Electrochemical PlaSmonic Optical Modulators (EPSOMs) with an ultrahigh contrast ratio ($\sim$ 17.6 dB) and sub-millisecond (~ 500 μs) temporal response time. Our approach leverages the spectral (wavelength) shift of the highly dispersive and distinctively narrow Fano resonance of plasmonic nanohole array due to the n. We further utilize a novel spectral engineering that tunes the transmission band of the Fano resonance spectrum (electro-plasmonic bandpass filter) with the transmission window of the narrow bandpass filter. The principle underlying our flat optical modulator is summarized in the Figure 4.1. The processes are initiated by negative(positive) voltages which induce ion influx (efflux) and electron injection (extraction) due to the reduction(oxidation): the inserted(extracted) electrons modify the net electron density and in turn its optical properties via electronic structure modification. Application of a positive (negative) applied potential to electro-plasmonic filter makes the electrochromic polymer "oxidized" or "doped" ("reduced" or "de-doped") due to the simultaneous efflux (influx) of electron (e^{-}) and cations (Na^{+}) from the polymer host (Fig. 4.1). The doped electrochromic polymer (Fig. 4.1b) results in the spectral overlapping of the electro-plasmonic bandpass filter with the notch filter. Thus, EPSOM passes the incident light, resulting in the "ON" state (Fig. 4.1a). De-doped (Fig. 4.1d) PEDOT, on the other hand, causes a large wavelength shift in the pass-band of the electro-plasmonic bandpass filter and no longer overlaps with the notch filter bandpass.Therefore, EPSOM blocks incident light and results in the "OFF" state (Fig. 4.1b). In the following, we present a phenomenological model that accurately explains the complex nature of Fano resonances in electrochromically loaded nanohole arrays. We show that effective refractive index modulation of the ultrathin PEDOT causes a large spectral shift of the Fano resonance profile. We then show that the EPSOM response time drastically improves with the lateral and vertical downscaling of the polymer load. Using electrochemical and optoelectrochemical measurements, we demonstrate the sub-millisecond ($\sim$ 500 μs) response time of EPSOM. Last, through our optoelectrochemical measurements, we prove the drastically increased optical contrast ratio ($\sim$ 17.6 dB) with EPSOM. Our electrochromic flat optical modulator, i.e., EPSOM establishes a blueprint for a completely new family of ultrahigh optical contrast and high response time nanoelectrochromic flat optical modulator.

4.1 Materials and methods

4.1.1 Nanohole array fabrication

Suspended plasmonic nanohole array chips were manufactured using high-throughput and large-area Lift-off-Free Evaporation (LIFE) lithography. Figure 4.2 summarizes the manufacturing process schematically. First, a 100 nm thick silicon nitride (Si_3N_4) thin film was deposited on 4 inch diameter silicon (Si) wafer using a low-pressure chemical vapor deposi-

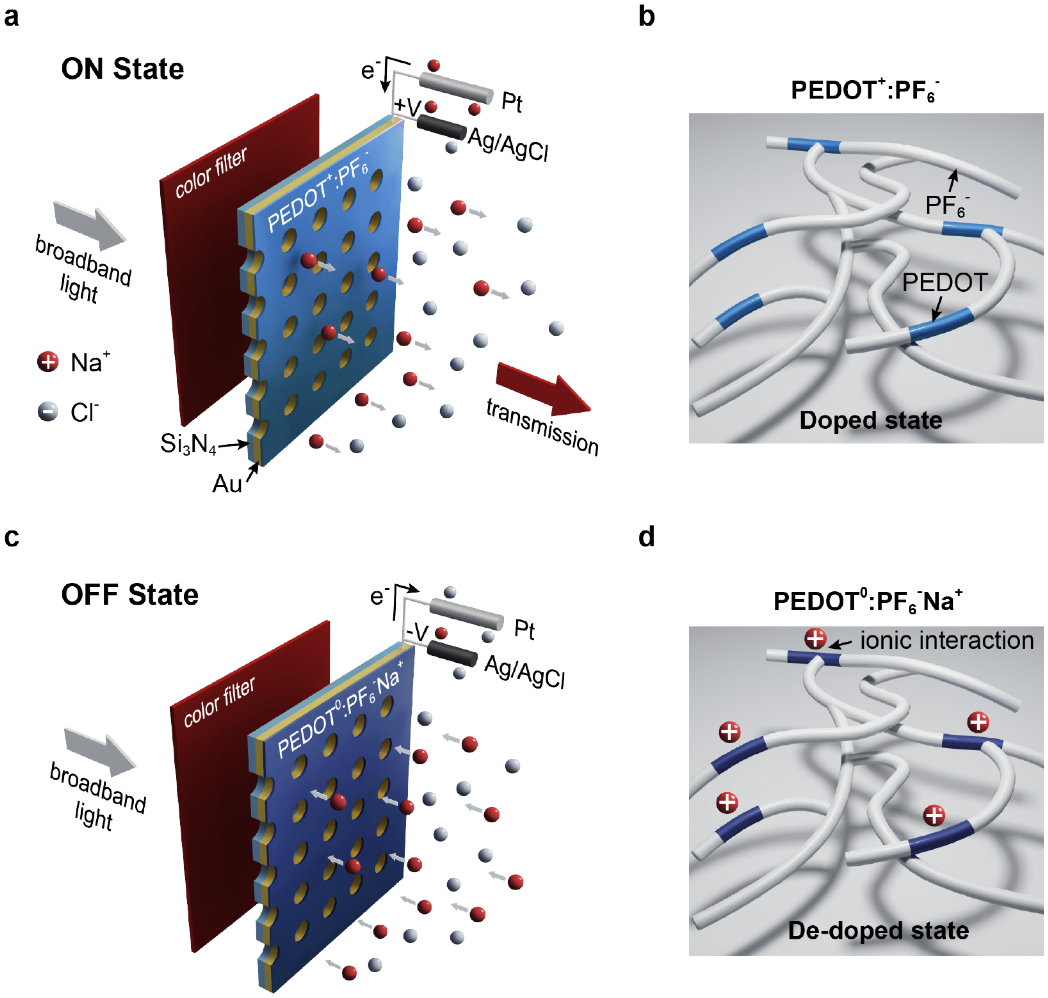

Figure 4.1: The working mechanism of the subwavelength thick EPSOM. a. Schematic of the EPSOM under positive applied potential (ON-state). A positively applied potential leads to the oxidation (doping) of the $PEDOT - PF_6$ load. Efflux of electrons (e^-) and sodium ions (Na^+) occurs simultaneously from the electrochromic polymer backbone. In the doped state of the load, electro-plasmonic filter is precisely tuned with the fixed bandpass filter, resulting in a strong transmitted signal. b. Schematic diagram of the $PEDOT - PF_6$ load in the doped state. c. Schematic of the EPSOM under negative applied voltage. The negative applied voltage initiates the reduction (dedoping) of the load. Influx of electrons (e^-) and sodium ions (Na^+) modulates the optical properties of the load. The modulated load causes a mismatch between the passband of the electro-plasmonic filter and fixed bandpass filter, therefore, leads to a suppression of the optical transmission. d. Schematic diagram of the $PEDOT - PF_6$ load in the de-doped state.

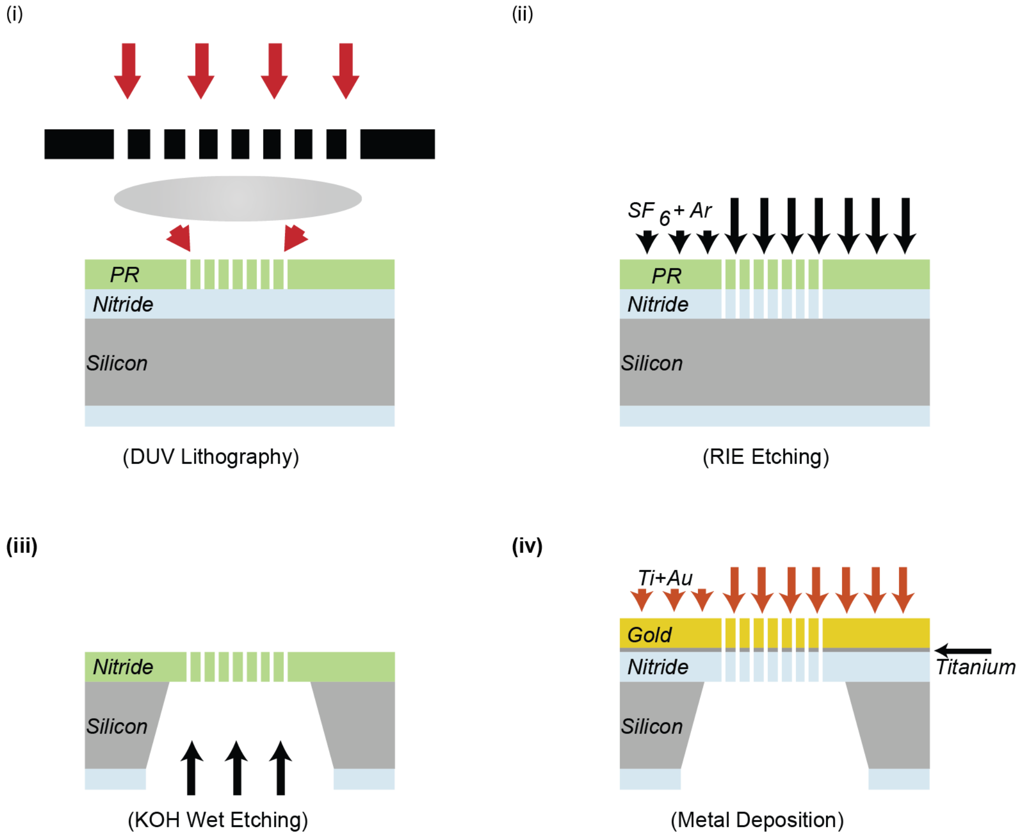

Figure 4.2: Large-scale fabrication of plasmonic nanohole arrays. Lift-off free deep UV nanolithography of plasmonic nanohole arrays. It consists of three consecutive steps: (i) spin coating of antireflection and photoresist layers, and wafer-scale patterning of plasmonic devices using deep UV (DUV) lithography, (iii) fabrication of the free-standing nanostructures using wet and reactive ion processes, and (iv) direct deposition of the metal layer.

tion (LPCVD) technique. A 300 nm thick negative photoresist (PR) was coated on the wafer and patterned using deep ultraviolet (DUV, 248 nm) light followed by reactive ion etching and PR removal. The Si substrate was removed by potassium hydroxide (KOH) to produce a free-standing Si_3N_4 membrane. Finally, suspended plasmonic nanohole array was defined on the Si_3N_4 membrane by electron beam evaporation of 125 nm thick gold using a custom-built electron beam evaporator. Before evaporation of gold, an interlayer of 5 nm titanium (Ti) was evaporated on Si_3N_4 to increase adhesion. The depositions were carried out at a pressure of 1.2×10^{-6} Torr and an evaporation rate of 0.5 Å/sec.

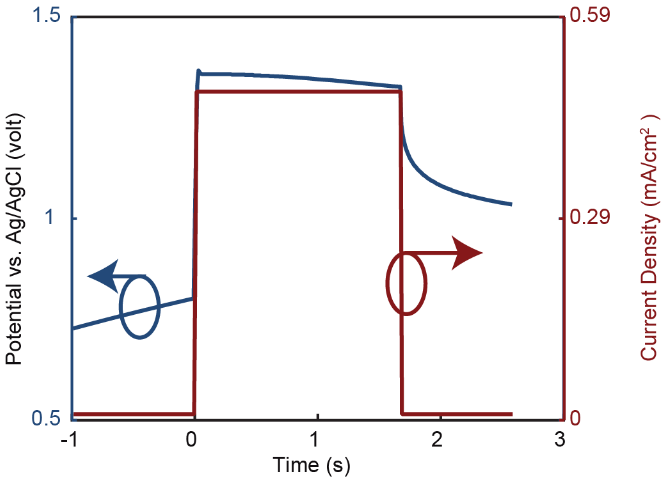

Figure 4.3: Electrochemical deposition of the PEDOT. We use a constant current density of 0.47 mA/ cm^2 for 1.67 s (blue curve) for 5 nm thick PEDOT. We measure the potential during the deposition (red curve). The potential is gradually decreasing with time is the indication of PEDOT deposition.

4.1.2 Electrochemical Deposition of PEDOT

The electrochemical deposition of $PEDOT - PF_6$ polymer was performed in an electrochemical medium consisting of 10 mM EDOT (3,4-Ethylenedioxythiophene) (Sigma-Aldrich, 483028) monomer and 100 mM tetrabutylammonium hexafluorophosphate (TBAPF$_6$) (Sigma-Aldrich, 281026) supporting electrolyte and propylene carbonate (PC) (Sigma-Aldrich, 310328) solvent. For deposition, three-electrode electrochemical cells (nanohole array as a working electrode, platinum as a counter electrode, and $Ag/AgCl$ wire as a reference electrode) and a potentiostat (Gamry Reference 600) were used. The deposition was performed in galvanostatic mode with a deposition current density of 0.47 mA/ cm^2 for 1.67 seconds for each ~ 5 nm PEDOT thickness. The measured potential during deposition begun at around 1.45 V and gradually decreases with deposition time due to a decrease in electrode impedance during deposition of PEDOT that confirmed the reliable deposition of PEDOT (Figure 4.3).

4.1.3 Full-wave numerical simulations

In our finite time difference (FDTD) simulation, the experimental dielectric data 'Au (Gold)-CRC' was used for the gold layer [267]. The refractive index of the Si_3N_4 and electrolyte background was set to $n_s = 2.16$ and $n_w = 1.33$. For the simulation results presented in this work, we considered the 25 nm thick PEDOT layer. The PEDOT reactive index was taken from the literature [166]. Similar electrochromic-plasmonic modeling approaches were reported in previous publications [166, 225]. A pair of periodic boundary conditions were used in the directions x and y. Perfectly match layer (PML) boundary conditions were used in z directions. An adaptive meshing scheme with a minimum grid size of 1.5 nm was adopted.

4.1.4 Electrochemical characterization

The electrochemical properties of PEDOT load were characterized by cyclic voltammetry (CV) and electrical impedance spectroscopy (EIS) measurements. The CV was scanned over a potential range of 0 V to 0.5 V versus $Ag/AgCl$ at a scan rate of 50 mV/sec in a monomer-free solution of 100 mM of $TBAPF_6$ in propylene carbonate solvent. The thickness of the deposited PEDOT thin film was measured using scanning electron microscopy (SEM). Impedance spectra of EIS are recorded in the frequency range 1 Hz to 10 kHz by applying a sinusoidal excitation signal with an excitation amplitude of 10 mV (Eac) superimposed on the constant dc potential of 200 mV (E_{dc}) in 1 M NaCl solution. The impedance data were fitted to an equivalent electrical circuit in order to obtain quantitative values for the circuit components. Gamry Echem Analyst software was used for fitting EIS data.

4.1.5 Spectroelectrochemical measurements

All the spectral data were obtained using Nikon TE 2000-U inverted microscope coupled to Ocean optics HR4000 spectrometer, Thorlabs DCU223 USB CCD camera, and Thorlabs PDA100A photodiode. We used a normally incident dia-illumination unpolarized broadband light source ($400 - 1100$ nm) to obtain the transmission spectrum of the plasmonic nanohole array. NI USB-6001 data acquisition device and LabView software were used for the acquisition of the photodiode signal. MATLAB toolbox 'cftool' (curve fitting toolbox) was used to obtain PEDOT switching time τ by fitting experimental transmitted signal $T(t)$ data with decaying exponential function ($T(t) = a \times \exp(-t/\tau) + c$, where a is the switching contrast, and c is the transmitting intensity in the 'OFF' state).

4.2 Results

4.2.1 Large contrast from ultrathin electrochromic polymer

The ability to structure electrochromic materials at nanoscale dimensions opens the door for nanoionic field-effect devices with drastically enhanced ionic conductivity and high spatiotemporal response. Exploiting such enhanced material characteristics for electro-optic applications, on the other hand, require new device engineering strategies. To realize ultra-fast and high-modulation depth electro-optic switching, we merge the emergent behavior of nanoscale electrochromic polymers with drastically enhanced light-matter interactions in plasmonic structures. The EOT effect materializes in plasmonic subwavelength nanohole arrays at resonance wavelengths leading to strong coupling between the incident surface plasmon polaritons (SPPs) and the localized surface plasmons (LSPs). As shown in our FDTD simulations in Figure 4.4a for an excitation wavelength of 690 nm, coupling between incident surface SPPs and LSPs occurs within the plasmonic hot-spots around the rims of the nano-apertures, a volume that is enclosed within the ultra-thin electrochromic polymer load. The presence of bright hot-spots for the doped state of PEDOT load indicates efficient fueling of the electromagnetic energy to the out-coupling surface plasmons resulting in enhanced light transmission (EOT effect). De-doping of the PEDOT polymer strongly modulates the SPP-LSP coupling and causes a drastic drop of transmitted light intensity as suggested by the absence of hot spots around the nanohole apertures at the same wavelength (Figure 4.4b). Figure 4.4c is the chemical structure of the PEDOT that shows the reversible transition between the doped (top panel) to de-doped state (bottom panel) and associated charge carrier modulation. By exploiting a strong coupling mechanism among three plasmonic oscillators that are responsible for the EOT signal, the field-controlled modulations of the PEDOT load are transferred to a strong optical transmission signal at this excitation wavelength.

This electrochromic-plasmonic behavior could be understood within the framework of optical circuit theory. The SPPs created on in-coupling (SPP_1) and out-coupling (SPP_2) surfaces can be thought of as two lumped nanocircuits (LC resonators [287]) that are tied to each other through the LSP excitations (Figure 4.4d). PEDOT load controls the LSP resonances through the strong light-matter interactions enabled within the hot-spots. Accordingly, the doped/de-doped electrochromic load is incorporated to the LSP circuit as a parallel arm com-

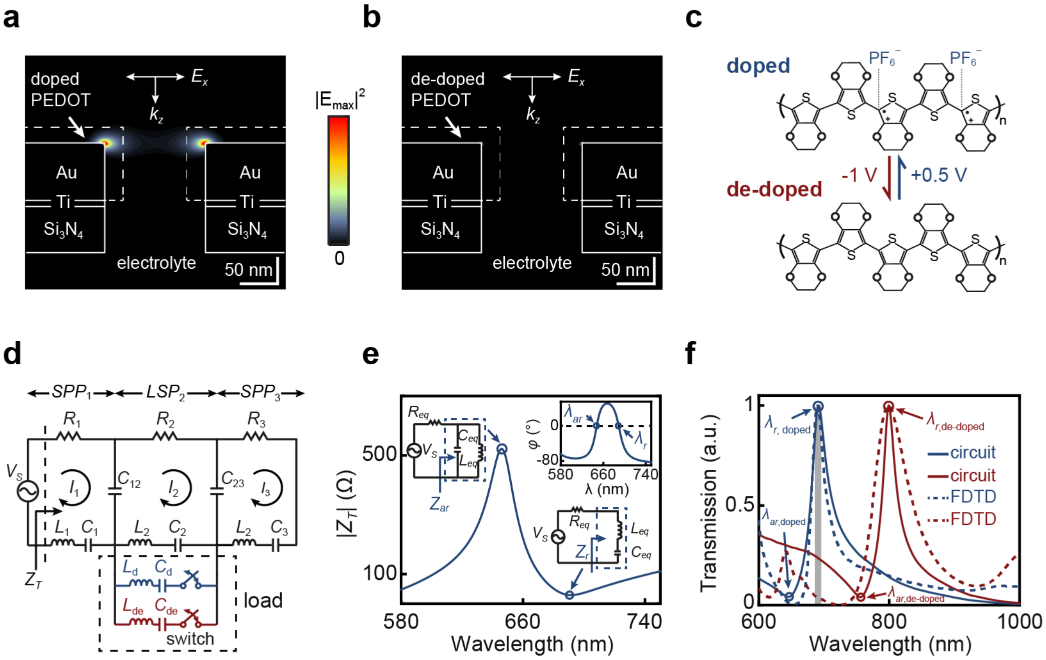

Figure 4.4: Large contrast ratio with an ultrathin electrochromic polymer. a. Side view of near-field enhancements along the pristine nanohole array structure (diameter 160 nm, pitch 450 nm) at 690 nm for x-polarized incident light propagating along the z-direction (normal to the nanohole surface). FDTD simulation shows the presence of strong light confinement (hot spots) due to the strong SPP-LSP coupling at the doped state of the PEDOT (25 nm thick). b. FDTD simulation shows the absence of hot spots due to the weak SPP-LSP coupling at the de-doped state of the PEDOT. c. Chemical structure of the PEDOT. During the doped (top panel) to de-doped (bottom panel) transition, the number of positive charge carriers in the PEDOT decreases due a negative applied potential (reduction reaction; PEDOT accepts electron). The opposite occurs when the doped to de-doped transition occurs due to a positive potential (oxidation reaction; PEDOT donates an electron). d. The coupled LC-oscillator model capturing the Fano resonant EOT effect in electrochromically loaded plasmonic nanohole structure. Meshes I_1, I_2, and I_3 represent plasmonic oscillators on the in-coupling metal/water interface (SPP$_1$), at hole aperture rims (LSP) and at the out-coupling metal/Si_3N_4 interface (SPP$_2$), respectively. An external voltage $V_s = V_o \cos(\omega t)$ is introduced as the electrical analogue of the incident light excitation. e. The magnitude of the total impedance $|Z_T|$ seen by the voltage source is calculated from the circuit model using the Thevenin theorem. The top left inset shows a parallel RLC (anti-resonant) circuit. Bottom right inset shows a series (resonant) RLC resonant circuit. The top right inset shows that phase (φ) of $|Z_T|$ varies with the wavelength (λ). f. Transmission spectrum of the EPOSM to the doping state of the PEDOT load. Switching of the load from the doped (blue curve) leads to the de-doped (red curve) state leads to red shifting of the transmission spectrum. Circuit model (solid line) and FDTD (dashed line) are compared.

posed of tunable inductive and capacitive circuit elements [288]. Resistors are added in each plasmonic resonator to account for the radiative and non-radiative losses [136]. The equivalent impedance of the electro-plasmonic circuit controls the power delivered from the source ($P = |V_s|^2/Z_{eq}$), the circuit counterpart of the transmitted light intensity through the nanohole array. Here, input impedance Z_{eq} is a combination of equivalent resistance R_{eq} and equivalent reactance X_{eq}. As shown in Figure 4.4e, at $\sim$ 645 nm corresponding to the minimum power delivery (light transmission), equivalent reactance X_{eq} can be projected to a circuit consisting of parallel inductive and capacitive reactances (left inset) operating at the resonance condition $\omega^2 = L_{eq}C_{eq}$. A large reactance$X_p = (L_{eq}/C_{eq})/(j\omega L_{eq} - j/\omega C_{eq})$) and the zero-phase difference between the source voltage and current (Figure 4.4e, top right inset) is observed at this “open-circuit” or “anti-resonant” condition corresponding to one of the natural resonances of the three coupled oscillator circuit. As shown in Figure 4.4e, the next resonance condition is satisfied at $\sim$ 690 nm as a result of the cancelation of equivalent inductive and capacitive reactances ($X_s = j\omega L_{eq} - j/\omega C_{eq}$) that are in series at this operating frequency (bottom right inset). For this near “short-circuit“ or “resonant” condition ($Z_{eq} = R_{eq}$), we observe zero phase difference between the source voltage and current (Figure 4.4e, top right inset) and enhanced power transfer corresponding to the EOT transmission peak.

Fano resonance lineshape of the transmission spectrum plays a critically important role in achieving large electro-optic modulation with ionic doping of the electrochromic load. As shown in Figure 4.4f (blue curve), the interplay between open and short circuit resonance conditions within a narrow spectral window is responsible for the highly dispersive power transmission characteristics ($P = |V_s|^2/Z_{eq}$) with a distinctly asymmetric shape. With the de-doping of the electrochromic polymer, resonances corresponding to the open (transmission minimum) and short (transmission peak) circuit conditions are shifted to longer wavelengths (Figure 4.4f, red curve) due to the increased load inductance and capacitance. This observation is in strong agreement with our FDTD simulations (Figure 4.4f, dashed curves); the Fano resonance spectrum is firmly controlled by the doping state of the ultrathin PEDOT load without distorting the Fano resonance line shape. Addition of a narrow band-pass filter ($FWHM \approx 20$nm) spectrally tuned to the short circuit resonance condition (EOT peak) for the doped state of the PEDOT load (Figure 4.4f, blue curve) allows us to translate the EOT resonance wavelength shift to large intensity modulations. As shown in Figure 4.4f, in a precisely designed platform, de-doping of the PEDOT load leads to red shifting of the Fano resonance spectrum and spectral overlapping of the open circuit condition (corresponding to transmission minimum of the nanohole array) with the bandpass window of the band-pass filter. This causes a dramatic reduction in the transmitted light intensity, an effect that we exploit to achieve high-contrast ratio electro-optic switching using low-power voltage sources.

4.2.2 Flat modulator geometry optimization towards ultrafast switching

For ultrathin nano-electrochromic loads, ionic diffusion time ($\tau_D \propto L^2/D$, where L is the film thickness and D is the diffusion constant) plays a critically important role in determining the response time of conducting polymers: fast electro-optic switching of an electrochromic polymer require the rapid formation of a charged doping/de-doping layer. To achieve a fast-electro-optic response, we experimentally analyzed and optimized the contribution of ionic mass transfer and capacitive doping effects in ultrathin electrochromic polymers by mapping out Au electrode-PEDOT system to an equivalent circuit model (Fig. 4.5a inset). In this model, a solution resistance R_S is added in series with an electrolyte-polymer interface element consisting of an electrical double layer (non-faradic) capacitance C_{EDL} and a charge transfer resistance R_{CT}. Doping capacitance and diffusion impedance of the electrochromic polymer is incorporated in series to this circuit through electronic bulk capacitance C_{PEDOT} and finite-length Warburg diffusion impedance $Z_{Warburg}$, which is characterized by the diffusional time constant τ_D and the diffusional pseudocapacitance C_D [289, 290]

$$Z_{warburg} = \frac{\sqrt{\tau_D}}{C_D\sqrt{j\omega}} \coth\left(j\omega\tau_D\right)^{1/2} \tag{4.1}$$

where ω is the angular frequency. We conduct electrochemical impedance spectroscopy (EIS) of PEDOT film electrodeposited on Au surfaces (see methods) to find equivalent circuit parameters (see methods). As shown in Figure 4.5a and Figure 4.5b, an excellent agreement between our circuit model and experimental measurements is observed within a wide frequency range from 1 Hz to 10 kHz. The total impedance is represented as $Z_{total}\left(\omega\right) = Z_{re} - jZ_{im}$, where Z_{re} and Z_{re} are the real and imaginary parts of the total impedance. Our EIS analysis shows that the (Au) electrode-PEDOT system displays a resistive behavior at high frequencies ($\sim$ 10 kHz), corresponding to a near 0 phase angle between current and voltage (Figure 4.5b, red curve). The total impedance is mainly the solution resistance R_s of the 1 M NaCl electrolyte solution at this

Table 4.1: The numerical fitting results of equivalent circuit components of $PEDOT - PF_6$ coated electrodes: Bottom: $\sqrt{Area} = 13$ mm, Top: 25 nm thick $PEDOT - PF_6$.

PEDOT layer area vs. capacitances with fixed area				
$\sqrt{Area}$ (mm)	$Z_{Warburg}$		C_{PEDOT} (mF)	C_D (mF)
	$Y_o\left(S.\text{sec}^{0.5}\right)$	$\sqrt{\tau_D}$ ($\text{sec}^{0.5}$)		
5	4.559×10^{-3}	0.0970	0.348	0.414
13	133.7×10^{-3}	0.1337	0.877	17.87
PEDOT layer thickness vs. capacitances with fixed area				
Thickness (nm)	$Z_{Warburg}$		C_{PEDOT} (mF)	C_D (mF)
	$Y_o\left(S.\text{sec}^{0.5}\right)$	$\sqrt{\tau_D}$ ($\text{sec}^{0.5}$)		
5	12.78×10^{-3}	0.0881	0.241	1.12
25	133.7×10^{-3}	0.1337	0.877	17.87

high frequency. It is evident from the Nyquist plot in Figure 4.5a that the Au-PEDOT system in 1 M NaCl electrolyte solution does not show a high-frequency semicircle in the impedance spectrum described by R_{ct} and C_{EDL} connected in parallel. The impedance spectrum (Nyquist) is therefore mainly dominated by the C_{PEDOT} and $Z_{Warburg}$ (or C_D) components (Figure 4.5a). When the frequency decreases, the capacitive nature of the (Au) electrode-PEDOT system begins to predominate as indicated by the decreasing phase angle in Figure 4.5b (red curve). Our analysis using equation 4.1 , and the equivalent circuit parameters (Table 4.1-top) shows that the $Im(Z_{Warburg})$ varies from to 0.02 to $8.9\ \Omega$ in the frequency range 10 kHz to 1 Hz. This observation indicates that the imaginary part of the total impedance Z_{im} of the (Au) electrode-PEDOT system is dominated by the C_{PEDOT} in the frequency range mentioned above (Figure 4.5a). Equation 4.1 also indicates that for very low frequencies (< 1 Hz) $Z_{Warburg}$ (or C_D) dominates due to diffusion-controlled faradic reactions. Therefore, given their contribution, C_{PEDOT} and/or C_D play a critical role in the trade-off between the electro-optical response time and the contrast ratio.

We optimize the PEDOT capacitances by using equivalent circuit modeling of experimental EIS data for different areas and thicknesses of the PEDOT. Besides, we conduct spectroelectrochemical measurements with EPSOM to determine the response time and confirm the validity of the optimization through equivalent circuit modeling. Our Equivalent Cir-

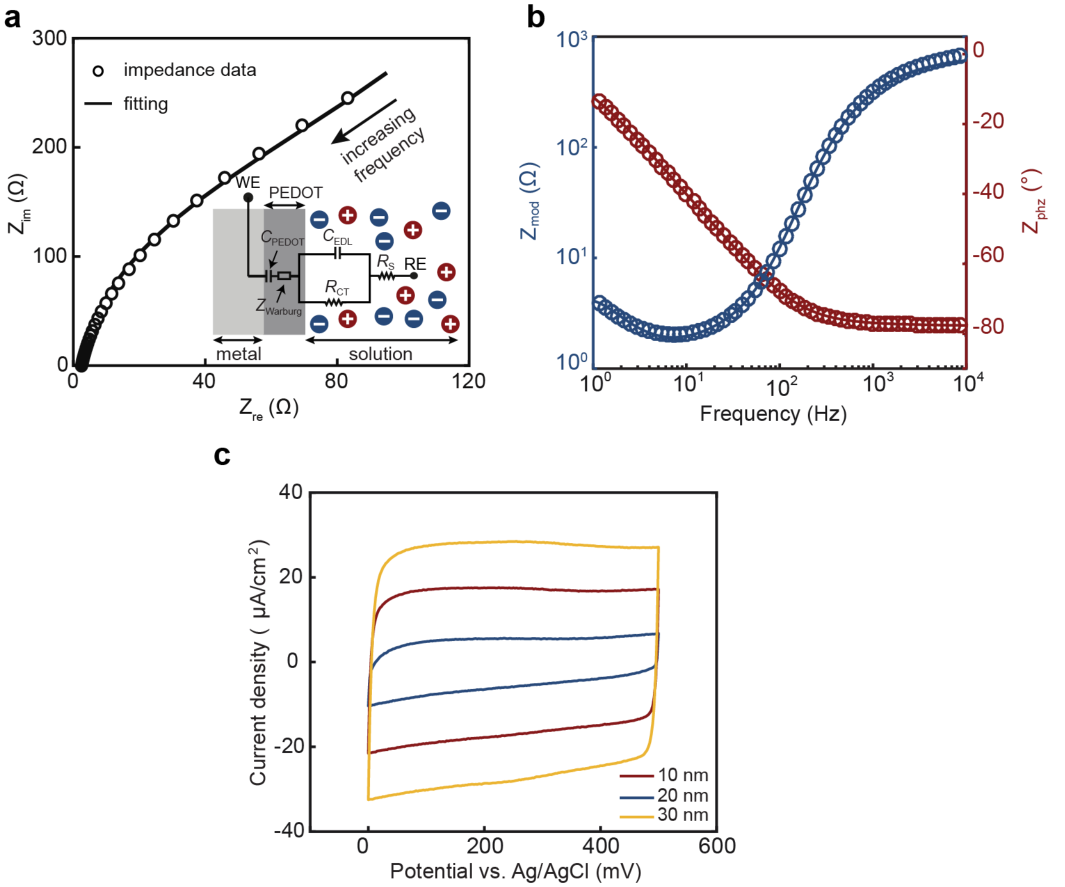

Figure 4.5: Electrochemical characterization of the electrochromic load. a. Complex plane impedance plot or Nyquist plot of the Au-PEDOT system with a PEDOT thickness of 25 nm and an area of 169 mm^2 measured at 0.2 V vs. $Ag/AgCl$. The frequency range is 1 Hz to 10 kHz. $\Delta E_{ac} = 10$ mV. Inset shows the equivalent circuit model for fitting (solid line) the measured impedance data (open circle). Bode plot (phase shift (blue), and total impedance (red)) of PEDOT coated (thickness 25 nm and area 169 mm^2) gold with the frequency range from 1 Hz -10 kHz. c. Cyclic voltammetry (CV) of the PEDOT load. Cyclic voltammetry of the PEDOT load with different thicknesses at scan rate 50 mV/sec over potential range of 0 V to 0.5 V in a 100 mM TBAPF$_6$ supporting electrolyte in propylene carbonate solvent.

cuit Model describing EIS experimental data shows that C_{PEDOT} decreases significantly with decreasing polymer thickness (Table 4.1-bottom). The capacitance value is 0.241 mF for 5 nm thick PEDOT film and 0.877 mF for 25 nm thick PEDOT film (Table 4.1-bottom). This observation is associated to the deterioration of the faradic charge storage capacity within a thin electrochromic polymer. On the other hand, due to the considerable decrease in ion diffusion, a drastically lower C_D value of 1.12 mF is obtained for a 5 nm thick PEDOT compared to 17.87

mF for a 25 nm thick layer (Table 4.1-bottom). The strong correlation between PEDOT capacitances and thicknesses is also established in our cyclic voltammetry measurement (Figure 4.5). The area enclosed below (above) the baseline of zero, which determines the charge accumulation (depletion) during anodic (cathodic) scanning, is a measure of PEDOT capacitance. The total capacitance increases with the thickness of the PEDOT results in the rise of the enclosed area, as predicted from the EIS observation. Capacitances (C_{PEDOT} and C_D) increase with an increasing PEDOT area, as confirmed by our EIS data (Table 4.1-top). Although the total faradaic capacitance is given as the capacitances (C_{PEDOT} and C_D) connected in series (Figure 4.5a inset), the value of the C_D is significantly higher than that of C_{PEDOT} (Table 4.1), which is consistent with the previous reports [291]. This observation confirms that the total faradaic capacitance is dominated by the C_{PEDOT}. We show that the C_{PEDOT} can be scaled down to a very low value with decreasing surface area while the thickness of the PEDOT layer is fixed (Figure 4.6a-blue). As a result, the smaller surface area of the PEDOT load is advantageous for the EPSOM; since it responds to voltage changes much faster than the larger ones. Similarly, our EIS measurements predict faster switching times with a thinner PEDOT load with a fixed area ($\sqrt{Area} =$ 13mm) due to a decrease in C_{PEDOT} (Figure 4.6a-red)

The EIS measurement predictions are confirmed by spectroelectrochemical measurements with our EPSOM (see methods). To this end, we use an inverted microscope (Nikon, TE 2000) combined with a free-space amplified photodetector and a grating spectrometer (Figure 4.6b). The inset of Figure 4.6b shows the electron scanning microscopy (SEM) of the electro-plasmonic filter, where the nanoholes are coated with PEDOT conformally. The measurement is carried out in an in-situ 3-electrode electrochemical cell designed in-house: the electro-plasmonic filter as a working electrode, the platinum coil as a counter electrode, and the AgCl-coated flexible Ag wire as a reference electrode, and the 1 M NaCl solution as an electrolyte. Also, using the unpolarized broadband halogen light source and the bright-field condenser lens of the microscope, we focus broadband light on the electro-plasmonic filter from the PEDOT-gold side. Electro-plasmonic modulator's transmission signals are collected by a microscope objective (Nikon, $10\times$, $NA = 0.30$) and then measured by the photodiode. We demonstrate faster switching by scaling down the thickness of the PEDOT load. As shown in Figure 4.6c-blue, the switching time is linearly proportional to the thickness of the load for a fixed area ($\sqrt{Area} =$ 13 mm). Similarly, in agreement with the EIS measurement, switching

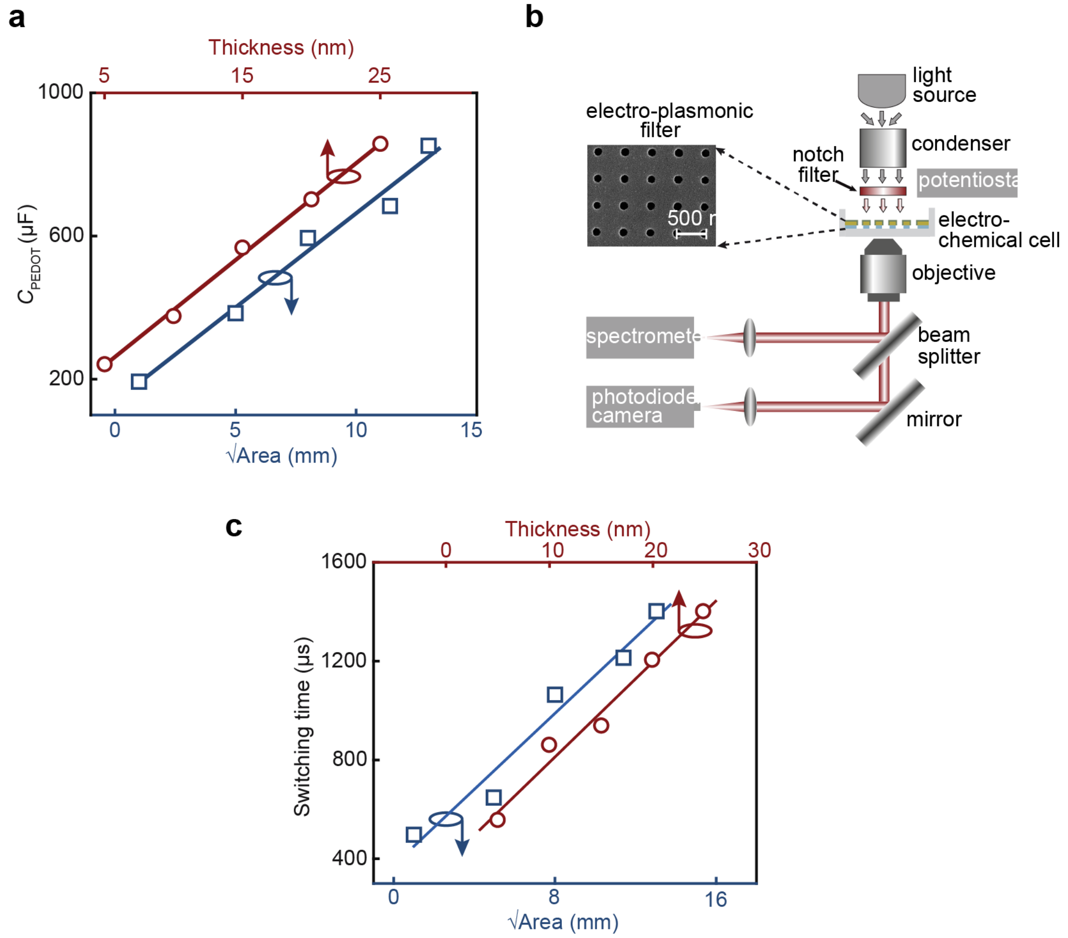

Figure 4.6: Ultrafast temporal response of the electrochromic load. a. Capacitance C_{PEDOT} as a function of the thickness and the area for Au/PEDOT electrodes in 1 M NaCl. $E_{dc} = 0.2$ V. C_{PEDOT} scales linearly with the active area for a fixed thickness of 25 nm (blue curve) and the thickness for fixed area $\sqrt{Area} = 13$ mm) (red curve). b. Schematic of the spectro-electrochemical setup that consists of a broadband light source, microscope condenser, a 10× objective, a beam splitter, a reflection mirror, two convex lenses, a high-resolution spectrometer, a 3-electroe electrochemical cell, and a potentiostat. Scanning electron microscope image of a plasmonic nanohole array (diameter 160 nm, pitch 450 nm) conformally coated with 25 nm PEDOT is shown (inset). c. Electro-optic measurements of EPSOM to analyze the temporal response of the PEDOT film. Linear scaling of the PEDOT switching speed with the active area for fixed thickness 25 nm (blue curve,) and thickness for the fixed area $\sqrt{Area} = 13$ mm) (red curve) is shown. d. Spectro-electrochemical measurement of PEDOT switching time. Switching time of PEDOT with area 1 mm^2 and thickness 25 nm. We measure switching time of electro-plasmonic modulator with 1 mm^2 electrode area expose to the 1 M NaCl solution

time scales with the active area of the PEDOT load at a fixed thickness ($\sim$ 25 nm) (Figure 4.6c, blue line). Therefore, we demonstrate that the switching time is scaled down with the area and thickness of the electrochromic polymer, in agreement with previous experimental studies [272]. Remarkably, for the EPSOM with a PEDOT thickness of 25 nm and an active area of 1 mm^2, we demonstrate sub-millisecond switching time approximately 500 μs (Figure 4.6d). The ultra-fast switching time of our EPSOM is three orders of magnitude faster than the switching time of the electrochromic plasmonic device recently used for electro-optical modulation [67, 79, 292]. Also, for a pixel size of 124 μm of the desktop LCD display, extrapolation of our experimental results predicts a switching time of 358 μs, which is significantly higher than the commercially available LCDs (response time often in the order of milliseconds) [293].

4.2.3 Electro-plasmonic modulation

Highly dispersive Fano resonance line shape plays a critical role in realizing high contrast ratio electro-plasmonic modulation with nanoscale thin electrochromic load. To this aim, we first spectrally tune the transmission maximum electro-plasmonic filter to the transmission window of a notch filter (Figure 4.7a). The electro-plasmonic filter is biased at $+0.5$ V using a potentiostat in a three-electrode spectroelectrochemical cell (Figure 4.7b). Incident light from a broadband light source passes through the electro-plasmonic filter due to the EOT effect. Transmitted light is collected with a microscope objective and is coupled to a spectrometer or a CCD camera (see methods). Figure 4.7a (blue line) shows the transmission maximum of the electro-plasmonic filter spectrally overlapping the transmission window of a notch filter (pink rectangle). The application of negative bias causes a red shift in the electro-plasmonic filter spectrum due to the doped to dedoped transition of PEDOT load and associated change in the real part of the complex dielectric constant (Figure 4.7a, red curve). We exploit the ability of PEDOT to change its complex dielectric constant (real part) due to the applied potential and achieve a gigantic plasmonic resonance shift of $\sim$ 110 nm. The wavelength shift is sufficient to cause the spectral overlapping of the transmission minimum of the electro-plasmon filter and the transmission window of the notch filter (Figure 4.7a). As a result, a drastic reduction of the transmitted light intensity is observed in the transmission window of the notch filter (Figure 4.7a).

The contrast ratio between bright and dark state is defined by [294] $10 \times log_{10} \left(T_{on}/T_{off}\right)$,

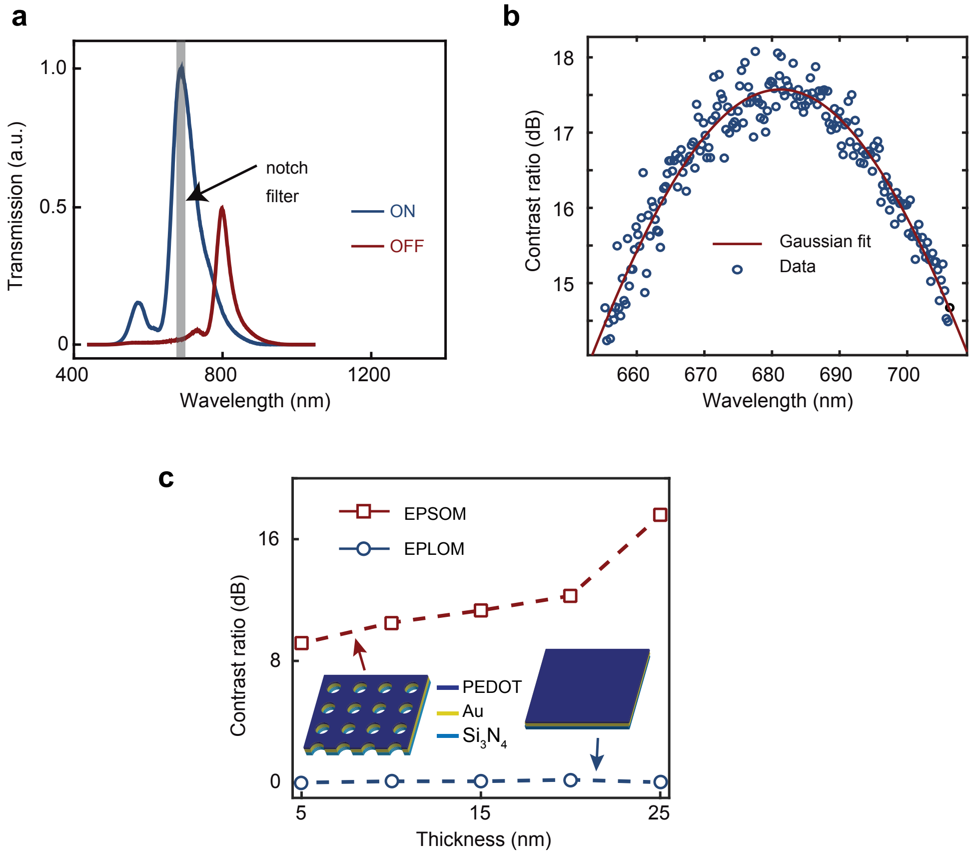

Figure 4.7: Demonstration of active modulation with electro-plasmonic modulator. a. Spectral measurements are obtained with doped (blue line) and de-doped (red line) PEDOT. Notch filter(pink) represents a bandpass filter spectrally tuned to the transmission maximum of the electro-plasmonic filter placed between the light source and electro-plasmonic filter. b. The high contrast ratio of the electro-plasmonic filter is achieved in the spectral range from 650 to 705 nm due to the small T_{off}. The red line is a Gaussian fit to the contrast ratio calculated with $10 \times log_{10}\,(T_{on}/T_{off})$ from the experimental data. The fitting shows a maximum contrast ratio of 17.6 dB for the spectral of interest c. Modulation depth of EPSOM is compared with EPLOM for a fixed area 1 mm^2 and thinness of the PEDOT varies from5 nm to 25 nm. The dashed lines are guide for the eye.

where T_{on} (T_{off}) stand for transmission value at $+0.5$ V (-1 V). It is obvious that high (low) value of T_{on} (T_{off}) leads to large contrast ratio. In electro-plasmonic filter, the electrochromic polymer (i.e., PEDOT) acts as a mediator that couples the external signal to the spectrum shift of the electro-plasmonic filter by changing the real part of the dielectric constant $Re(\varepsilon)$. In addition the red curve of the Figure 4.7a shows that electrochromic polymer dedoping increases the absorption of light in agreement with the previous study [295]. Increased absorption of light, associated with the imaginary part of the dielectric constant $Re(\varepsilon)$, is the result of the free carrier optical absorption effect of the additional electrons during the dedoping process. However, the modulation is primarily controlled by the EOT transmission spectrum that is controlled by the electrochromic load rather increased absorption Fig.4.7b . To prove this, we compare EPSOM with the reference Electrochromic PoLymer Optic Modulator (EPLOM) at a wavelength of 683 nm, which falls within the spectral range of interest. EPLOM is fabricated by depositing PEDOT on 16 nm Au coated (Si_3N_4) membrane (without nanoholes). Figure 4.7c shows a significantly higher contrast ratio in the EPSOM (red circle) than in the EPLOM (blue circle). For example, the EPSOM with a 5 nm thick PEDOT layer shows a contrast ratio of $\sim$ 9.16 dB, which is more than 1000-fold larger than the EPLOM ($\sim$ 0.0076 dB) with a similar PEDOT thickness (Figure 4.7c). Thus, our experimental results show that the $Im(\varepsilon)$ of the electrochromic polymer has a negligible contribution to the contrast ratio. Another key piece of information Fig.4.7c indicates that the contrast ratio increases with the thickness of the PEDOT. This is consistent with our FDTD calculation and EIS measurement predictions. Our FDTD calculations show that we need a PEDOT thickness of approximately 25 nm to cover the drastically enhanced electrical field in plasmonic hot spots and to make use of enhanced light-matter interactions. In addition, our EIS results predicted that increasing thickness would enhance the doping / depositing process by enhancing the faradaic capacitance C_{PEDOT}. We therefore need an electrochromic thickness that covers hot spots and offers a relatively large C_{PEDOT}. In this regard, the thickness of $\sim$ 25 nm addresses both of these criteria and results in a higher contrast ratio compared to the thickness of less than 25 nm, as confirmed by our demonstration in Figure 4.7c.

Our system inherits ultra-fast time response due to the use of nanoscale thick electrochromic loads. To confirm this, we demonstrate the ultra-fast switching dynamics of the EPSOM using a nanoscale PEDOT load (thickness 25 nm). We apply a square wave voltage of 100 Hz between $+0.5$ volt and -1 volt versus $Ag/AgCl$. A high-speed Si photodetector is used to detect the signal. The photodiode signal is collected with a data acquisition device and LabVIEW. Figure 4.8a presents the dynamic response plot in which the left vertical modulator response axis (blue line) and right vertical applied potential axis (red line) are plotted as a function of time on the horizontal axis. The measurements shown here indicate that even with a

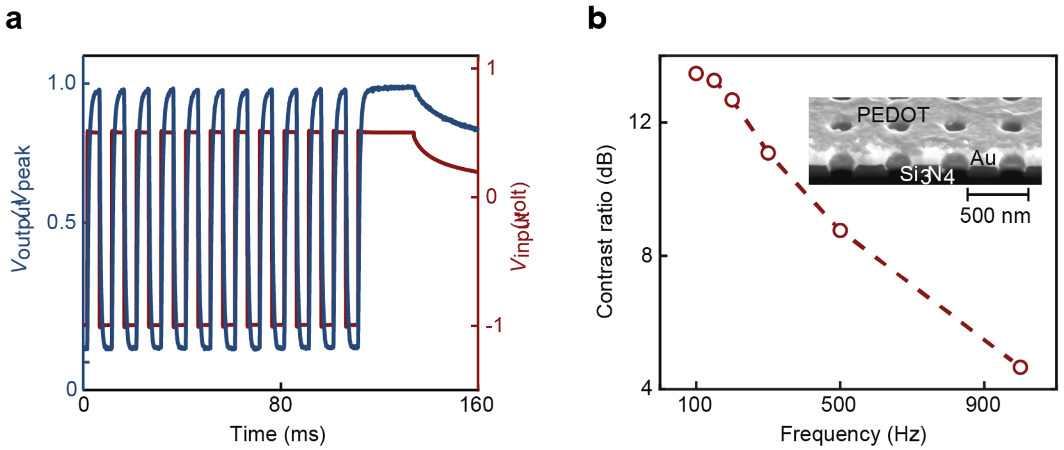

Figure 4.8: Demonstration of high bandwidth operation of EPSOM. (a) Timing data of the EPSOM (blue curve) subject to applied square wave voltage between $+0.5$ V and -1 V (red curve) with a frequency 100 Hz. PEDOT active area is 1 mm^2 and thickness is 25 nm. Light form broadband source transmitted through the EPSOM. Transmitted light is collected with 10× objectives and couple to the photodiode. (b) High bandwidth capability of the EPSOM is shown. Contrast ratio varies with frequency in the range of 100 Hz to 1000 Hz. The dashed lines are guide for the eye.

Table 4.2: Summary of previously reported electrochromic (EC) polymer modulators.

Reference	Mechanism	EC Polymer	Thickness (nm)	Switching (ms)	Contrast ratio (dB)
DeLongchamp et al. [296]	Electrochemical	PEDOT	1000	> 1000	7.4
Agrawal et al. [80]	Electroplasmonic	Persian blue	20	600	14
Xu at al. [79]	Electroplasmonic	PANI	25	9	8.2
Peng et al. [67]	Electroplasmonic	PANI	25	20	3
This work	Electroplasmonic	PEDOT	25	0.5	17.6

relatively large surface area ($\sim 1\ mm^2$), the modulated signal is precisely following the square wave applied at 100 Hz. Also, our EPSOM allows the electro-optical modulation of light up to a few kilohertz without substantially losing the contrast ratio (Figure 4.8b).

4.3 Discussion

In summary, we introduced an elegant and powerful electro-plasmonic approach enabling ultra-high contrast ratio electro-optic switching at high video rates. Remarkably, this approach shows that the Fano resonant EOT spectrum of the plasmonic nanohole array can be sensitively tuned to the notch filter passband by harnessing the electrical field tunability of the electrochromic load. A relatively small potential (~ 1.5 volt) causes reversible tuning of the electrochromic load by doping (dedoping) due to cation efflux (influx) in the electrolyte medium. Such 'electro-plasmonic' tuning effects contradict conventional electrochromic device trends. In conventional electrochromic devices, the thicker film achieves a higher contrast ratio of switching, but takes an inevitable dramatic toll on switching time. However, the combination of nanometer thick electrochromic material with plasmonic resonators favors our system with a high contrast ratio in conjunction with faster switching time thanks to enhanced light-matter interactions due to nanoscale light confinement in plasmonic nanostructures and a highly dispersive Fano resonance EOT effect. Further, the interplay between the transmission window of the notch filter (second filter) with the minimum transmission (maximum) electro-plasmon filter enables a bright (dark) state. The dark state has a negligible intensity and is much better than the recently reported electrochemical and electrochemical plasmonic devices [67, 79]. The excellent dark state realizes an ultra-high contrast ratio beyond the scope of recently reported electrochromic technologies. Table 4.2 summarizes the performance metrics of some of the recent reports on the experimental demonstration of electrochromic devices. Our EPSOM with a contrast ratio of up to 17.6 dB and a sub-millisecond switching time down to 0.5 ms represents, to the best of our knowledge, the best performance of any type of electrochromic device that has been experimentally demonstrated so far.

From a technological standpoint, EPSOM can be used to create high-definition, high-fresh-rate electronic displays, and it can overcome the limitations of liquid crystal displays (LCD) in displaying moving images due to their slow decay time in the millisecond range [293, 297]. The slow decay time τ_d is inherent to LCDs, depends on the distance between LCD parallel electrodes d, rotational viscosity and elastic constant K of LCs ($\tau_d = \gamma d^2/\pi^2 K$) [298]. With EPSOM 's superior sub-microsecond decay time, high refresh rate displays suitable for viewing moving images can be realized. Another drawback of LCDs is the difficulty of achieving a high pixel density (resolution) greater than 1000 pixels/ inch due to increased optical crosstalk [293]. EPSOM based displays can achieve ultrahigh resolution with a pixel pitch (~ 3 μm) and pixel footprint less than 1 μm^2 area [299]. Thus, a large number of pixels with a resolution of more than 6000 pixels / inch can be easily integrated into the active area of the displays without running into the optical crosstalk issues by adding plasmonic Bragg mirrors surrounding the nanohole array. Future studies should explore how the current understanding of the performance of the EPSOM on a rigid substrate evolves with a flexible substrate. Future studies should also explore how full color plasmonic pixels can be achieved by using alternative plasmonic materials such as aluminum.

Chapter 5

Conclusions and Future Work

Active plasmonic is a growing and challenging plasmonic sub-field. Active control over plasmonic resonances is inevitably needed for the advancement of future plasmonic technologies such as modulators, switches and field-effect neurophotonics devices. This thesis has demonstrated such active control by incorporating nanoelectrochromic load consist of lumped nanocircuit elements. The nanoelectrochromic loading approaches demonstrated in this thesis overcome the inherent low voltage sensitivities of plasmonic resonators [72, 265]. Findings in this thesis pave the way for realizing ultrasensitive field-effect neuroelectrode and ultra-high modulation depth flat optical modulators for ultrathin display applications. In conclusion, this thesis has achieved three aims:

- **Active plasmonic nanoantenna**. I discussed the underlying physical mechanisms underpinning the dynamic reconfigurability and outline several promising approaches in realizing active plasmonic nanoantennas with novel characteristics. I envision that this review will provide unambiguous insights and guidelines in building high-performance dynamic plasmonic nanoantennas for a plethora of emerging applications, including ultra-broadband sensors and detectors, dynamic switches and large-scale electrophysiological recordings for neuroscience applications.
- **Nanoelectrochromic field reporters in electrophysiological applications**. I introduced an ultrasensitive and extremely bright nanoscale electric-field probe overcoming the low photon-count limitations of existing optical field reporters. My electro-plasmonic approach lays foundation of a new class of extracellular in vitro and in vivo electrophys-

iological probes offering non-invasive, ultrasensitive and high spatiotemporal resolution measurement capabilities with light.

- **Nanoelectrochromic flat optical modulators**. I introduced a subwavelength-thick ($<$ 250 nm) nano-electrochromic flat optic modulator that can simultaneously deliver ultrafast ($\sim$ 500 μs) and remarkably high-contrast ratio $\sim$ 17.6 dB) electro-optic switching capability and operate at high operational bandwidths (2 kHz). The field-effect flat optic modulator shown here paves the way to the advancement of ultrathin and high bandwidth display technologies based on electrochromic soft materials suitable for flexible electronics.

5.1 Future Work

Beyond the in vitro experiments I have shown in chapter 3, our electro-plasmonic probes open the possibility of in vivo electrophysiological studies with high SSNRs for prolonged periods. For in vivo electrophysiological testing, it is possible to utilize our electro-plasmonic probes using two distinct approaches: (i) electro-plasmonic probes can be integrated on flexible and biocompatible substrates for surgical implantation, and (ii) colloidal versions of them can be synthesized and functionalized with cell specific biomolecules for deep tissue brain imaging. Several recent studies have already demonstrated integration of plasmonic devices on flexible substrates and optical fibers using high-throughput fabrication techniques [127, 300]. For deep tissue use, high quality colloidal plasmonic nanoparticles can be synthesized in solution [301] and loaded with electrochromic polymers using electrostatic oxidative polymerization [231]. Furthermore, biocompatible PEDOT polymer enables surface functionalization with proteins for tethering colloidal electro-plasmonic nanoprobes to specific cell types [275]. A similar approach has been successfully used for interfacing extracellular QDs to a range of cell lines, including neurons [260]. An important consideration for in vivo applications is the light scattering and absorption in tissue. Electrochromic properties of PEDOT polymer are manifested over a broad wavelength spectrum spanning well into near-infrared wavelengths [266]. Using spherically symmetric core-shell plasmonic structures [301] loaded with electrochromic polymers, it is possible to operate electro-plasmonic probes at near-infrared wavelengths, which is particularly amenable for in vivo applications due to reduced photon scattering and absorption in deep tissue as shown in a recent study [302]. Another important consideration for in vivo probes is the inherent immune response. In this respect, electro-plasmonic nanoparticles offers two important advantages. PEDOT films functionalized with bioactive molecules are shown to dramatically minimize immune response and enable in vivo recording of electrical activity for long time periods [275]. Moreover, probe dimensions that are smaller than 12 μm are shown induce minimal reactive cell responses [274]. In this sense, nanoscale dimensions of our polymer coated electro-plasmonic probes is particularly advantageous for long-term operation.

Bibliography

[1] S. A. Maier, M. L. Brongersma, P. G. Kik, S. Meltzer, A. A. Requicha, and H. A. Atwater, "Plasmonics—a route to nanoscale optical devices," *Advanced materials*, vol. 13, no. 19, pp. 1501–1505, 2001.

[2] S. A. Maier and H. A. Atwater, "Plasmonics: Localization and guiding of electromagnetic energy in metal/dielectric structures," *Journal of applied physics*, vol. 98, no. 1, p. 10, 2005.

[3] E. Ozbay, "Plasmonics: merging photonics and electronics at nanoscale dimensions," *Science*, vol. 311, no. 5758, pp. 189–193, 2006.

[4] J. C. Ndukaife, V. M. Shalaev, and A. Boltasseva, "Plasmonics—turning loss into gain," *Science*, vol. 351, no. 6271, pp. 334–335, 2016.

[5] A. Naldoni, V. M. Shalaev, and M. L. Brongersma, "Applying plasmonics to a sustainable future," *Science*, vol. 356, no. 6341, pp. 908–909, 2017.

[6] D. K. Gramotnev and S. I. Bozhevolnyi, "Plasmonics beyond the diffraction limit," *Nature photonics*, vol. 4, no. 2, pp. 83–91, 2010.

[7] W. L. Barnes, A. Dereux, and T. W. Ebbesen, "Surface plasmon subwavelength optics," *Nature*, vol. 424, no. 6950, pp. 824–830, 2003.

[8] M. Moskovits, "The case for plasmon-derived hot carrier devices," *Nature Nanotechnology*, vol. 10, no. 1, pp. 6–8, 2015.

[9] A. Polman and H. A. Atwater, "Photonic design principles for ultrahigh-efficiency photovoltaics," *Nature materials*, vol. 11, no. 3, pp. 174–177, 2012.

[10] A. Polman, “Plasmonics applied,” *Science*, vol. 322, no. 5903, pp. 868–869, 2008.

[11] H. A. Atwater and A. Polman, “Plasmonics for improved photovoltaic devices,” *Nature Materials*, vol. 9, no. 3, pp. 205–213, 2010.

[12] H. Yu, Y. Peng, Y. Yang, and Z.-Y. Li, “Plasmon-enhanced light–matter interactions and applications,” *npj Computational Materials*, vol. 5, no. 1, pp. 1–14, 2019.

[13] M. L. Brongersma and V. M. Shalaev, “The case for plasmonics,” *science*, vol. 328, no. 5977, pp. 440–441, 2010.

[14] N. Dean, “Colouring at the nanoscale,” *Nature nanotechnology*, vol. 10, no. 1, pp. 15–16, 2015.

[15] Y. Zeng, R. Hu, L. Wang, D. Gu, J. He, S.-Y. Wu, H.-P. Ho, X. Li, J. Qu, B. Z. Gao *et al.*, “Recent advances in surface plasmon resonance imaging: detection speed, sensitivity, and portability,” *Nanophotonics*, vol. 6, no. 5, pp. 1017–1030, 2017.

[16] J. N. Anker, W. P. Hall, O. Lyandres, N. C. Shah, J. Zhao, and R. P. Van Duyne, “Biosensing with plasmonic nanosensors,” *Nature Materials*, vol. 7, no. 6, pp. 442–453, 2008. [Online]. Available: https://doi.org/10.1038/nmat2162

[17] R. Gordon, “Biosensing with nanoaperture optical tweezers,” *Optics & Laser Technology*, vol. 109, pp. 328–335, 2019.

[18] F. Yesilkoy, R. A. Terborg, J. Pello, A. A. Belushkin, Y. Jahani, V. Pruneri, and H. Altug, “Phase-sensitive plasmonic biosensor using a portable and large field-of-view interferometric microarray imager,” *Light: Science & Applications*, vol. 7, no. 2, pp. 17 152–17 152, 2018.

[19] R. Adato, A. A. Yanik, J. J. Amsden, D. L. Kaplan, F. G. Omenetto, M. K. Hong, S. Erramilli, and H. Altug, “Ultra-sensitive vibrational spectroscopy of protein monolayers with plasmonic nanoantenna arrays,” *Proceedings of the National Academy of Sciences*, vol. 106, no. 46, pp. 19 227–19 232, 2009.

[20] A. A. Yanik, M. Huang, O. Kamohara, A. Artar, T. W. Geisbert, J. H. Connor, and H. Altug, “An optofluidic nanoplasmonic biosensor for direct detection of live viruses from biological media,” *Nano letters*, vol. 10, no. 12, pp. 4962–4969, 2010.

[21] A. A. Yanik, A. E. Cetin, M. Huang, A. Artar, S. H. Mousavi, A. Khanikaev, J. H. Connor, G. Shvets, and H. Altug, "Seeing protein monolayers with naked eye through plasmonic fano resonances," *Proceedings of the National Academy of Sciences*, vol. 108, no. 29, pp. 11 784–11 789, 2011.

[22] K. Turcheniuk, T. Dumych, R. Bilyy, V. Turcheniuk, J. Bouckaert, V. Vovk, V. Chopyak, V. Zaitsev, P. Mariot, N. Prevarskaya, R. Boukherroub, and S. Szunerits, "Plasmonic photothermal cancer therapy with gold nanorods/reduced graphene oxide core/shell nanocomposites," *RSC Advances*, vol. 6, no. 2, pp. 1600–1610, 2016. [Online]. Available: http://dx.doi.org/10.1039/C5RA24662H

[23] F. Lütolf, G. Basset, D. Casari, A. Luu-Dinh, and B. Gallinet, "Plasmonics for the industry," in *Plasmonics: Metallic Nanostructures and Their Optical Properties XIII*, vol. 9547. International Society for Optics and Photonics, 2015, p. 954717.

[24] S. Aksu, A. A. Yanik, R. Adato, A. Artar, M. Huang, and H. Altug, "High-throughput nanofabrication of infrared plasmonic nanoantenna arrays for vibrational nanospectroscopy," *Nano letters*, vol. 10, no. 7, pp. 2511–2518, 2010.

[25] Editorial, "Commercializing plasmonics," *Nat. Photonics*, vol. 9, p. 477, 2015.

[26] S.-H. Oh and H. Altug, "Performance metrics and enabling technologies for nanoplasmonic biosensors," *Nature communications*, vol. 9, no. 1, pp. 1–5, 2018.

[27] Editorial, "Focusing in on applications," *Nature Nanotechnology*, vol. 10, no. 1, p. 1, 2015.

[28] S. A. Maier, *Plasmonics: fundamentals and applications*. Springer Science & Business Media, 2007.

[29] X. Zhu, G. M. Imran Hossain, M. George, A. Farhang, A. Cicek, and A. A. Yanik, "Beyond noble metals: High q-factor aluminum nanoplasmonics," *ACS Photonics*, vol. 7, no. 2, pp. 416–424, 2020.

[30] M. L. Brongersma, "Introductory lecture: nanoplasmonics," *Faraday discussions*, vol. 178, pp. 9–36, 2015.

[31] J. Krupka, M. E. Tobar, J. G. Hartnett, D. Cros, and J.-M. Le Floch, “Extremely high-q factor dielectric resonators for millimeter-wave applications,” *IEEE transactions on microwave theory and techniques*, vol. 53, no. 2, pp. 702–712, 2005.

[32] K. A. Willets and R. P. Van Duyne, “Localized surface plasmon resonance spectroscopy and sensing,” *Annu. Rev. Phys. Chem.*, vol. 58, pp. 267–297, 2007.

[33] L. E. Kreno, K. Leong, O. K. Farha, M. Allendorf, R. P. Van Duyne, and J. T. Hupp, “Metal–organic framework materials as chemical sensors,” *Chemical reviews*, vol. 112, no. 2, pp. 1105–1125, 2012.

[34] A. D. McFarland and R. P. Van Duyne, “Single silver nanoparticles as real-time optical sensors with zeptomole sensitivity,” *Nano letters*, vol. 3, no. 8, pp. 1057–1062, 2003.

[35] A. J. Haes and R. P. Van Duyne, “A nanoscale optical biosensor: sensitivity and selectivity of an approach based on the localized surface plasmon resonance spectroscopy of triangular silver nanoparticles,” *Journal of the American Chemical Society*, vol. 124, no. 35, pp. 10 596–10 604, 2002.

[36] A. J. Haes, W. P. Hall, L. Chang, W. L. Klein, and R. P. Van Duyne, “A localized surface plasmon resonance biosensor: First steps toward an assay for alzheimer’s disease,” *Nano letters*, vol. 4, no. 6, pp. 1029–1034, 2004.

[37] A. J. Haes, L. Chang, W. L. Klein, and R. P. Van Duyne, “Detection of a biomarker for alzheimer’s disease from synthetic and clinical samples using a nanoscale optical biosensor,” *Journal of the American Chemical Society*, vol. 127, no. 7, pp. 2264–2271, 2005.

[38] J. Zhao, X. Zhang, C. R. Yonzon, A. J. Haes, and R. P. Van Duyne, “Localized surface plasmon resonance biosensors,” 2006.

[39] C. R. Yonzon, D. A. Stuart, X. Zhang, A. D. McFarland, C. L. Haynes, and R. P. Van Duyne, “Towards advanced chemical and biological nanosensors—an overview,” *Talanta*, vol. 67, no. 3, pp. 438–448, 2005.

[40] D. Stuart, A. Haes, C. Yonzon, E. Hicks, and R. Van Duyne, “Biological applications of localised surface plasmonic phenomenae,” in *IEE Proceedings-Nanobiotechnology*, vol. 152, no. 1. IET, 2005, pp. 13–32.

[41] J. M. Bingham, J. N. Anker, L. E. Kreno, and R. P. Van Duyne, “Gas sensing with high-resolution localized surface plasmon resonance spectroscopy,” *Journal of the American Chemical Society*, vol. 132, no. 49, pp. 17 358–17 359, 2010.

[42] N. Liu, M. Mesch, T. Weiss, M. Hentschel, and H. Giessen, “Infrared perfect absorber and its application as plasmonic sensor,” *Nano letters*, vol. 10, no. 7, pp. 2342–2348, 2010.

[43] N. Liu, M. L. Tang, M. Hentschel, H. Giessen, and A. P. Alivisatos, “Nanoantenna-enhanced gas sensing in a single tailored nanofocus,” *Nature materials*, vol. 10, no. 8, pp. 631–636, 2011.

[44] A. Tittl, P. Mai, R. Taubert, D. Dregely, N. Liu, and H. Giessen, “Palladium-based plasmonic perfect absorber in the visible wavelength range and its application to hydrogen sensing,” *Nano letters*, vol. 11, no. 10, pp. 4366–4369, 2011.

[45] A. Tittl, X. Yin, H. Giessen, X.-D. Tian, Z.-Q. Tian, C. Kremers, D. N. Chigrin, and N. Liu, “Plasmonic smart dust for probing local chemical reactions,” *Nano Letters*, vol. 13, no. 4, pp. 1816–1821, 2013.

[46] A. Tittl, H. Giessen, and N. Liu, “Plasmonic gas and chemical sensing,” *Nanophotonics*, vol. 3, no. 3, pp. 157–180, 2014.

[47] F. Eftekhari, C. Escobedo, J. Ferreira, X. Duan, E. M. Girotto, A. G. Brolo, R. Gordon, and D. Sinton, “Nanoholes as nanochannels: flow-through plasmonic sensing,” *Analytical chemistry*, vol. 81, no. 11, pp. 4308–4311, 2009.

[48] J. Ferreira, M. J. Santos, M. M. Rahman, A. G. Brolo, R. Gordon, D. Sinton, and E. M. Girotto, “Attomolar protein detection using in-hole surface plasmon resonance,” *Journal of the American Chemical Society*, vol. 131, no. 2, pp. 436–437, 2009.

[49] S. Chen, M. Svedendahl, R. P. Van Duyne, and M. Käll, “Plasmon-enhanced colorimetric elisa with single molecule sensitivity,” *Nano Letters*, vol. 11, no. 4, pp. 1826–1830, 2011.

[50] S. Kim, M. S. Jang, V. W. Brar, Y. Tolstova, K. W. Mauser, and H. A. Atwater, "Electronically tunable extraordinary optical transmission in graphene plasmonic ribbons coupled to subwavelength metallic slit arrays," *Nature communications*, vol. 7, no. 1, pp. 1–8, 2016.

[51] D. Ansell, I. Radko, Z. Han, F. Rodriguez, S. Bozhevolnyi, and A. Grigorenko, "Hybrid graphene plasmonic waveguide modulators," *Nature communications*, vol. 6, no. 1, pp. 1–6, 2015.

[52] M. Ayata, Y. Fedoryshyn, W. Heni, B. Baeuerle, A. Josten, M. Zahner, U. Koch, Y. Salamin, C. Hoessbacher, C. Haffner *et al.*, "High-speed plasmonic modulator in a single metal layer," *Science*, vol. 358, no. 6363, pp. 630–632, 2017.

[53] M. Klein, B. H. Badada, R. Binder, A. Alfrey, M. McKie, M. R. Koehler, D. G. Mandrus, T. Taniguchi, K. Watanabe, B. J. LeRoy *et al.*, "2d semiconductor nonlinear plasmonic modulators," *Nature communications*, vol. 10, no. 1, pp. 1–7, 2019.

[54] A. Habib, X. Zhu, U. I. Can, M. L. McLanahan, P. Zorlutuna, and A. A. Yanik, "Electro-plasmonic nanoantenna: A nonfluorescent optical probe for ultrasensitive label-free detection of electrophysiological signals," *Science advances*, vol. 5, no. 10, p. eaav9786, 2019.

[55] J. Zhang, T. Atay, and A. V. Nurmikko, "Optical detection of brain cell activity using plasmonic gold nanoparticles," *Nano letters*, vol. 9, no. 2, pp. 519–524, 2009.

[56] K. Chen, E. S. P. Leong, M. Rukavina, T. Nagao, Y. J. Liu, and Y. Zheng, "Active molecular plasmonics: tuning surface plasmon resonances by exploiting molecular dimensions," *Nanophotonics*, vol. 4, no. 2, pp. 186–197, 2015.

[57] N. Jiang, X. Zhuo, and J. Wang, "Active plasmonics: principles, structures, and applications," *Chemical reviews*, vol. 118, no. 6, pp. 3054–3099, 2017.

[58] A. Habib, X. Zhu, S. Fong, and A. A. Yanik, "Active plasmonic nanoantenna: an emerging toolbox from photonics to neuroscience:," *Nanophotonics*, vol. 9, no. 12, pp. 3805–3829, 2020.

[59] A. V. Krasavin and N. Zheludev, “Active plasmonics: Controlling signals in au/ga waveguide using nanoscale structural transformations,” *Applied Physics Letters*, vol. 84, no. 8, pp. 1416–1418, 2004.

[60] X. Duan and N. Liu, “Magnesium for dynamic nanoplasmonics,” *Accounts of Chemical Research*, vol. 52, no. 7, pp. 1979–1989, 2019.

[61] S. Dong, K. Zhang, Z. Yu, and J. A. Fan, “Electrochemically programmable plasmonic antennas,” *ACS nano*, vol. 10, no. 7, pp. 6716–6724, 2016.

[62] R. Liu, X. Shan, H. Wang, and N. Tao, “Plasmonic measurement of electron transfer between a single metal nanoparticle and an electrode through a molecular layer,” *Journal of the American Chemical Society*, vol. 141, no. 29, pp. 11 694–11 699, 2019.

[63] T. B. Hoang and M. H. Mikkelsen, “Broad electrical tuning of plasmonic nanoantennas at visible frequencies,” *Applied Physics Letters*, vol. 108, no. 18, p. 183107, 2016.

[64] Y. B. Zheng, L. Jensen, W. Yan, T. R. Walker, B. K. Juluri, L. Jensen, and T. J. Huang, “Chemically tuning the localized surface plasmon resonances of gold nanostructure arrays,” *The Journal of Physical Chemistry C*, vol. 113, no. 17, pp. 7019–7024, 2009.

[65] J. Merlein, M. Kahl, A. Zuschlag, A. Sell, A. Halm, J. Boneberg, P. Leiderer, A. Leitenstorfer, and R. Bratschitsch, “Nanomechanical control of an optical antenna,” *Nature Photonics*, vol. 2, no. 4, pp. 230–233, 2008.

[66] Q. Wang, L. Liu, Y. Wang, P. Liu, H. Jiang, Z. Xu, Z. Ma, S. Oren, E. K. Chow, M. Lu *et al.*, “Tunable optical nanoantennas incorporating bowtie nanoantenna arrays with stimuli-responsive polymer,” *Scientific reports*, vol. 5, p. 18567, 2015.

[67] J. Peng, H.-H. Jeong, Q. Lin, S. Cormier, H.-L. Liang, M. F. De Volder, S. Vignolini, and J. J. Baumberg, “Scalable electrochromic nanopixels using plasmonics,” *Science advances*, vol. 5, no. 5, p. eaaw2205, 2019.

[68] A. Agrawal, S. H. Cho, O. Zandi, S. Ghosh, R. W. Johns, and D. J. Milliron, “Localized surface plasmon resonance in semiconductor nanocrystals,” *Chemical reviews*, vol. 118, no. 6, pp. 3121–3207, 2018.

[69] P. Mulvaney, J. Pérez-Juste, M. Giersig, L. M. Liz-Marzán, and C. Pecharromán, "Drastic surface plasmon mode shifts in gold nanorods due to electron charging," *Plasmonics*, vol. 1, no. 1, pp. 61–66, 2006.

[70] G. Garcia, R. Buonsanti, E. L. Runnerstrom, R. J. Mendelsberg, A. Llordes, A. Anders, T. J. Richardson, and D. J. Milliron, "Dynamically modulating the surface plasmon resonance of doped semiconductor nanocrystals," *Nano letters*, vol. 11, no. 10, pp. 4415–4420, 2011.

[71] R. Chapman and P. Mulvaney, "Electro-optical shifts in silver nanoparticle films," *Chemical physics letters*, vol. 349, no. 5-6, pp. 358–362, 2001.

[72] X. Liu, J.-H. Kang, H. Yuan, J. Park, S. J. Kim, Y. Cui, H. Y. Hwang, and M. L. Brongersma, "Electrical tuning of a quantum plasmonic resonance," *Nature nanotechnology*, vol. 12, no. 9, pp. 866–870, 2017.

[73] L. Sjulson and G. Miesenbock, "Optical recording of action potentials and other discrete physiological events: a perspective from signal detection theory," *Physiology*, vol. 22, no. 1, pp. 47–55, 2007.

[74] L. Kastrup and S. W. Hell, "Absolute optical cross section of individual fluorescent molecules," *Angewandte Chemie International Edition*, vol. 43, no. 48, pp. 6646–6649, 2004.

[75] D. R. Hochbaum, Y. Zhao, S. L. Farhi, N. Klapoetke, C. A. Werley, V. Kapoor, P. Zou, J. M. Kralj, D. Maclaurin, N. Smedemark-Margulies *et al.*, "All-optical electrophysiology in mammalian neurons using engineered microbial rhodopsins," *Nature methods*, vol. 11, no. 8, pp. 825–833, 2014.

[76] M. Scanziani and M. Häusser, "Electrophysiology in the age of light," *Nature*, vol. 461, no. 7266, pp. 930–939, 2009.

[77] Y. Zhang, C. Fowler, J. Liang, B. Azhar, M. Y. Shalaginov, S. Deckoff-Jones, S. An, J. B. Chou, C. M. Roberts, V. Liberman *et al.*, "Electrically reconfigurable non-volatile metasurface using low-loss optical phase-change material," *Nature Nanotechnology*, vol. 16, no. 6, pp. 661–666, 2021.

[78] J. Karst, M. Floess, M. Ubl, C. Dingler, C. Malacrida, T. Steinle, S. Ludwigs, M. Hentschel, and H. Giessen, “Electrically switchable metallic polymer nanoantennas,” *Science*, vol. 374, no. 6567, pp. 612–616, 2021.

[79] T. Xu, E. C. Walter, A. Agrawal, C. Bohn, J. Velmurugan, W. Zhu, H. J. Lezec, and A. A. Talin, “High-contrast and fast electrochromic switching enabled by plasmonics,” *Nature Communications*, vol. 7, no. 1, pp. 1–6, 2016.

[80] A. Agrawal, C. Susut, G. Stafford, U. Bertocci, B. McMorran, H. J. Lezec, and A. A. Talin, “An integrated electrochromic nanoplasmonic optical switch,” *Nano letters*, vol. 11, no. 7, pp. 2774–2778, 2011.

[81] N. J. Greybush, K. Charipar, J. A. Geldmeier, S. J. Bauman, P. Johns, J. Naciri, N. Charipar, K. Park, R. A. Vaia, and J. Fontana, “Dynamic plasmonic pixels,” *ACS nano*, vol. 13, no. 4, pp. 3875–3883, 2019.

[82] K. Xiong, G. Emilsson, A. Maziz, X. Yang, L. Shao, E. W. Jager, and A. B. Dahlin, “Plasmonic metasurfaces with conjugated polymers for flexible electronic paper in color,” *Advanced Materials*, vol. 28, no. 45, pp. 9956–9960, 2016.

[83] V. Giannini, A. I. Fernández-Domínguez, S. C. Heck, and S. A. Maier, “Plasmonic nanoantennas: fundamentals and their use in controlling the radiative properties of nanoemitters,” *Chemical reviews*, vol. 111, no. 6, pp. 3888–3912, 2011.

[84] L. Novotny and N. Van Hulst, “Antennas for light,” *Nature photonics*, vol. 5, no. 2, pp. 83–90, 2011.

[85] P. Biagioni, J.-S. Huang, and B. Hecht, “Nanoantennas for visible and infrared radiation,” *Reports on Progress in Physics*, vol. 75, no. 2, p. 024402, 2012.

[86] M. L. Brongersma, “Engineering optical nanoantennas,” *Nature Photonics*, vol. 2, no. 5, pp. 270–272, 2008.

[87] P. Ghenuche, S. Cherukulappurath, T. H. Taminiau, N. F. van Hulst, and R. Quidant, “Spectroscopic mode mapping of resonant plasmon nanoantennas,” *Physical review letters*, vol. 101, no. 11, p. 116805, 2008.

[88] T. J. Davis, D. E. Gómez, and A. Roberts, "Plasmonic circuits for manipulating optical information," *Nanophotonics*, vol. 6, no. 3, pp. 543–559, 2016.

[89] A. Kinkhabwala, Z. Yu, S. Fan, Y. Avlasevich, K. Müllen, and W. Moerner, "Large single-molecule fluorescence enhancements produced by a bowtie nanoantenna," *Nature Photonics*, vol. 3, no. 11, pp. 654–657, 2009.

[90] A. F. Koenderink, "Single-photon nanoantennas," *ACS photonics*, vol. 4, no. 4, pp. 710–722, 2017.

[91] L. Rodríguez-Lorenzo, R. A. Alvarez-Puebla, I. Pastoriza-Santos, S. Mazzucco, O. Stéphan, M. Kociak, L. M. Liz-Marzán, and F. J. García de Abajo, "Zeptomol detection through controlled ultrasensitive surface-enhanced raman scattering," *Journal of the American Chemical Society*, vol. 131, no. 13, pp. 4616–4618, 2009.

[92] R. Averitt, D. Sarkar, and N. Halas, "Plasmon resonance shifts of au-coated au 2 s nanoshells: insight into multicomponent nanoparticle growth," *Physical Review Letters*, vol. 78, no. 22, p. 4217, 1997.

[93] T. Kosako, Y. Kadoya, and H. F. Hofmann, "Directional control of light by a nano-optical yagi–uda antenna," *Nature Photonics*, vol. 4, no. 5, pp. 312–315, 2010.

[94] I. S. Maksymov, I. Staude, A. E. Miroshnichenko, and Y. S. Kivshar, "Optical yagi-uda nanoantennas," *Nanophotonics*, vol. 1, no. 1, pp. 65–81, 2012.

[95] D. Vercruysse, Y. Sonnefraud, N. Verellen, F. B. Fuchs, G. Di Martino, L. Lagae, V. V. Moshchalkov, S. A. Maier, and P. Van Dorpe, "Unidirectional side scattering of light by a single-element nanoantenna," *Nano letters*, vol. 13, no. 8, pp. 3843–3849, 2013.

[96] D. Vercruysse, X. Zheng, Y. Sonnefraud, N. Verellen, G. Di Martino, L. Lagae, G. A. Vandenbosch, V. V. Moshchalkov, S. A. Maier, and P. Van Dorpe, "Directional fluorescence emission by individual v-antennas explained by mode expansion," *Acs Nano*, vol. 8, no. 8, pp. 8232–8241, 2014.

[97] M. L. Brongersma, N. J. Halas, and P. Nordlander, "Plasmon-induced hot carrier science and technology," *Nature nanotechnology*, vol. 10, no. 1, pp. 25–34, 2015.

[98] D. Punj, M. Mivelle, S. B. Moparthi, T. S. Van Zanten, H. Rigneault, N. F. Van Hulst, M. F. García-Parajó, and J. Wenger, “A plasmonic ‘antenna-in-box’platform for enhanced single-molecule analysis at micromolar concentrations,” *Nature nanotechnology*, vol. 8, no. 7, pp. 512–516, 2013.

[99] A. Akimov, A. Mukherjee, C. Yu, D. Chang, A. Zibrov, P. Hemmer, H. Park, and M. Lukin, “Generation of single optical plasmons in metallic nanowires coupled to quantum dots,” *Nature*, vol. 450, no. 7168, pp. 402–406, 2007.

[100] J. S. Fakonas, H. Lee, Y. A. Kelaita, and H. A. Atwater, “Two-plasmon quantum interference,” *Nature Photonics*, vol. 8, no. 4, pp. 317–320, 2014.

[101] X. Ni, N. K. Emani, A. V. Kildishev, A. Boltasseva, and V. M. Shalaev, “Broadband light bending with plasmonic nanoantennas,” *Science*, vol. 335, no. 6067, pp. 427–427, 2012.

[102] L. Huang, X. Chen, H. Mühlenbernd, H. Zhang, S. Chen, B. Bai, Q. Tan, G. Jin, K.-W. Cheah, C.-W. Qiu *et al.*, “Three-dimensional optical holography using a plasmonic metasurface,” *Nature communications*, vol. 4, no. 1, pp. 1–8, 2013.

[103] P. Muehlschlegel, H.-J. Eisler, O. J. Martin, B. Hecht, and D. Pohl, “Resonant optical antennas,” *science*, vol. 308, no. 5728, pp. 1607–1609, 2005.

[104] I. Zoric, M. Zach, B. Kasemo, and C. Langhammer, “Gold, platinum, and aluminum nanodisk plasmons: material independence, subradiance, and damping mechanisms,” *ACS nano*, vol. 5, no. 4, pp. 2535–2546, 2011.

[105] A. Dasgupta, M.-M. Mennemanteuil, M. Buret, N. Cazier, G. Colas-des Francs, and A. Bouhelier, “Optical wireless link between a nanoscale antenna and a transducing rectenna,” *Nature communications*, vol. 9, no. 1, pp. 1–7, 2018.

[106] A. Alu and N. Engheta, “Input impedance, nanocircuit loading, and radiation tuning of optical nanoantennas,” *Physical review letters*, vol. 101, no. 4, p. 043901, 2008.

[107] P. B. Johnson and R.-W. Christy, “Optical constants of the noble metals,” *Physical review B*, vol. 6, no. 12, p. 4370, 1972.

[108] C. Jia, X. Li, N. Xin, Y. Gong, J. Guan, L. Meng, S. Meng, and X. Guo, "Interface-engineered plasmonics in metal/semiconductor heterostructures," *Advanced Energy Materials*, vol. 6, no. 17, p. 1600431, 2016.

[109] C. Clavero, "Plasmon-induced hot-electron generation at nanoparticle/metal-oxide interfaces for photovoltaic and photocatalytic devices," *Nature Photonics*, vol. 8, no. 2, pp. 95–103, 2014.

[110] P. R. West, S. Ishii, G. V. Naik, N. K. Emani, V. M. Shalaev, and A. Boltasseva, "Searching for better plasmonic materials," *Laser & Photonics Reviews*, vol. 4, no. 6, pp. 795–808, 2010.

[111] G. V. Naik, V. M. Shalaev, and A. Boltasseva, "Alternative plasmonic materials: beyond gold and silver," *Advanced Materials*, vol. 25, no. 24, pp. 3264–3294, 2013.

[112] J. M. McMahon, G. C. Schatz, and S. K. Gray, "Plasmonics in the ultraviolet with the poor metals al, ga, in, sn, tl, pb, and bi," *Physical Chemistry Chemical Physics*, vol. 15, no. 15, pp. 5415–5423, 2013.

[113] J. Sanz, D. Ortiz, R. Alcaraz De La Osa, J. Saiz, F. González, A. Brown, M. Losurdo, H. Everitt, and F. Moreno, "Uv plasmonic behavior of various metal nanoparticles in the near-and far-field regimes: geometry and substrate effects," *The Journal of Physical Chemistry C*, vol. 117, no. 38, pp. 19 606–19 615, 2013.

[114] M. G. Blaber, M. D. Arnold, and M. J. Ford, "A review of the optical properties of alloys and intermetallics for plasmonics," *Journal of Physics: Condensed Matter*, vol. 22, no. 14, p. 143201, 2010.

[115] U. Guler, A. Boltasseva, and V. M. Shalaev, "Refractory plasmonics," *Science*, vol. 344, no. 6181, pp. 263–264, 2014.

[116] C. Sönnichsen, T. Franzl, T. Wilk, G. von Plessen, J. Feldmann, O. Wilson, and P. Mulvaney, "Drastic reduction of plasmon damping in gold nanorods," *Physical review letters*, vol. 88, no. 7, p. 077402, 2002.

[117] A. Sobhani, A. Manjavacas, Y. Cao, M. J. McClain, F. J. Garcia de Abajo, P. Nordlander, and N. J. Halas, "Pronounced linewidth narrowing of an aluminum nanoparticle plasmon

resonance by interaction with an aluminum metallic film," *Nano letters*, vol. 15, no. 10, pp. 6946–6951, 2015.

[118] W. Zhou and T. W. Odom, "Tunable subradiant lattice plasmons by out-of-plane dipolar interactions," *Nature nanotechnology*, vol. 6, no. 7, pp. 423–427, 2011.

[119] B. Auguié and W. L. Barnes, "Collective resonances in gold nanoparticle arrays," *Physical review letters*, vol. 101, no. 14, p. 143902, 2008.

[120] G. Baffou, P. Berto, E. Bermúdez Ureña, R. Quidant, S. Monneret, J. Polleux, and H. Rigneault, "Photoinduced heating of nanoparticle arrays," *Acs Nano*, vol. 7, no. 8, pp. 6478–6488, 2013.

[121] R. Sundararaman, P. Narang, A. S. Jermyn, W. A. Goddard III, and H. A. Atwater, "Theoretical predictions for hot-carrier generation from surface plasmon decay," *Nature communications*, vol. 5, no. 1, pp. 1–8, 2014.

[122] J. B. Khurgin, "How to deal with the loss in plasmonics and metamaterials," *Nature nanotechnology*, vol. 10, no. 1, pp. 2–6, 2015.

[123] P. Dastmalchi and G. Veronis, "Efficient design of nanoplasmonic waveguide devices using the space mapping algorithm," *Optics express*, vol. 21, no. 26, pp. 32 160–32 175, 2013.

[124] I. Malkiel, M. Mrejen, A. Nagler, U. Arieli, L. Wolf, and H. Suchowski, "Plasmonic nanostructure design and characterization via deep learning," *Light: Science & Applications*, vol. 7, no. 1, pp. 1–8, 2018.

[125] H. Duan, H. Hu, K. Kumar, Z. Shen, and J. K. Yang, "Direct and reliable patterning of plasmonic nanostructures with sub-10-nm gaps," *ACS nano*, vol. 5, no. 9, pp. 7593–7600, 2011.

[126] H. Kollmann, X. Piao, M. Esmann, S. F. Becker, D. Hou, C. Huynh, L.-O. Kautschor, G. Bösker, H. Vieker, A. Beyer *et al.*, "Toward plasmonics with nanometer precision: nonlinear optics of helium-ion milled gold nanoantennas," *Nano letters*, vol. 14, no. 8, pp. 4778–4784, 2014.

[127] S. Aksu, M. Huang, A. Artar, A. A. Yanik, S. Selvarasah, M. R. Dokmeci, and H. Altug, “Flexible plasmonics on unconventional and nonplanar substrates,” *Advanced Materials*, vol. 23, no. 38, pp. 4422–4430, 2011.

[128] J. C. Hulteen and R. P. Van Duyne, “Nanosphere lithography: A materials general fabrication process for periodic particle array surfaces,” *Journal of Vacuum Science & Technology A: Vacuum, Surfaces, and Films*, vol. 13, no. 3, pp. 1553–1558, 1995.

[129] X. Zhang, A. V. Whitney, J. Zhao, E. M. Hicks, and R. P. Van Duyne, “Advances in contemporary nanosphere lithographic techniques,” *Journal of Nanoscience and Nanotechnology*, vol. 6, no. 7, pp. 1920–1934, 2006.

[130] R. Jin, Y. C. Cao, E. Hao, G. S. Métraux, G. C. Schatz, and C. A. Mirkin, “Controlling anisotropic nanoparticle growth through plasmon excitation,” *Nature*, vol. 425, no. 6957, pp. 487–490, 2003.

[131] J. Z. Zhang, “Biomedical applications of shape-controlled plasmonic nanostructures: a case study of hollow gold nanospheres for photothermal ablation therapy of cancer,” *The Journal of Physical Chemistry Letters*, vol. 1, no. 4, pp. 686–695, 2010.

[132] G. Acuna, F. Möller, P. Holzmeister, S. Beater, B. Lalkens, and P. Tinnefeld, “Fluorescence enhancement at docking sites of dna-directed self-assembled nanoantennas,” *Science*, vol. 338, no. 6106, pp. 506–510, 2012.

[133] M. J. McClain, A. E. Schlather, E. Ringe, N. S. King, L. Liu, A. Manjavacas, M. W. Knight, I. Kumar, K. H. Whitmire, H. O. Everitt *et al.*, “Aluminum nanocrystals,” *Nano letters*, vol. 15, no. 4, pp. 2751–2755, 2015.

[134] V. Flauraud, M. Mastrangeli, G. D. Bernasconi, J. Butet, D. T. Alexander, E. Shahrabi, O. J. Martin, and J. Brugger, “Nanoscale topographical control of capillary assembly of nanoparticles,” *Nature nanotechnology*, vol. 12, no. 1, pp. 73–80, 2017.

[135] X. Zhu, N. Cao, B. J. Thibeault, B. Pinsky, and A. A. Yanik, “Mechanisms of fano-resonant biosensing: Mechanical loading of plasmonic oscillators,” *Optics Communications*, vol. 469, p. 125780, 2020.

[136] N. Engheta, “Circuits with light at nanoscales: optical nanocircuits inspired by metamaterials,” *Science*, vol. 317, no. 5845, pp. 1698–1702, 2007.

[137] N. Engheta, A. Salandrino, and A. Alu, “Circuit elements at optical frequencies: nanoinductors, nanocapacitors, and nanoresistors,” *Physical Review Letters*, vol. 95, no. 9, p. 095504, 2005.

[138] N. Engheta, “From rf circuits to optical nanocircuits,” *IEEE Microwave Magazine*, vol. 13, no. 4, pp. 100–113, 2012.

[139] N. Liu, F. Wen, Y. Zhao, Y. Wang, P. Nordlander, N. J. Halas, and A. Alù, “Individual nanoantennas loaded with three-dimensional optical nanocircuits,” *Nano letters*, vol. 13, no. 1, pp. 142–147, 2013.

[140] A. Alu and N. Engheta, “Tuning the scattering response of optical nanoantennas with nanocircuit loads,” *Nature photonics*, vol. 2, no. 5, pp. 307–310, 2008.

[141] M. Schnell, A. Garcia-Etxarri, A. Huber, K. Crozier, J. Aizpurua, and R. Hillenbrand, “Controlling the near-field oscillations of loaded plasmonic nanoantennas,” *Nature Photonics*, vol. 3, no. 5, p. 287, 2009.

[142] P.-Y. Chen and A. Alù, “Optical nanoantenna arrays loaded with nonlinear materials,” *Physical Review B*, vol. 82, no. 23, p. 235405, 2010.

[143] A. Alù and N. Engheta, “Wireless at the nanoscale: optical interconnects using matched nanoantennas,” *Physical review letters*, vol. 104, no. 21, p. 213902, 2010.

[144] Y. Choi, D. Choi, and L. P. Lee, “Metal–insulator–metal optical nanoantenna with equivalent-circuit analysis,” *Advanced Materials*, vol. 22, no. 15, pp. 1754–1758, 2010.

[145] Y. Zhao, N. Engheta, and A. Alù, “Effects of shape and loading of optical nanoantennas on their sensitivity and radiation properties,” *JOSA B*, vol. 28, no. 5, pp. 1266–1274, 2011.

[146] Y. Sun, B. Edwards, A. Alù, and N. Engheta, “Experimental realization of optical lumped nanocircuits at infrared wavelengths,” *Nature materials*, vol. 11, no. 3, pp. 208–212, 2012.

[147] A. Alù and N. Engheta, “Theory, modeling and features of optical nanoantennas,” *IEEE Transactions on Antennas and Propagation*, vol. 61, no. 4, pp. 1508–1517, 2013.

[148] Y. Wang, M. Abb, S. A. Boden, J. Aizpurua, C. De Groot, and O. L. Muskens, “Ultrafast nonlinear control of progressively loaded, single plasmonic nanoantennas fabricated using helium ion milling,” *Nano letters*, vol. 13, no. 11, pp. 5647–5653, 2013.

[149] Q. Zhang, L. Bai, Z. Bai, P. Hu, and C. Liu, “Equivalent-nanocircuit-theory-based design to infrared broad band-stop filters,” *Optics express*, vol. 23, no. 7, pp. 8290–8297, 2015.

[150] F. Benz, B. de Nijs, C. Tserkezis, R. Chikkaraddy, D. O. Sigle, L. Pukenas, S. D. Evans, J. Aizpurua, and J. J. Baumberg, “Generalized circuit model for coupled plasmonic systems,” *Optics Express*, vol. 23, no. 26, pp. 33 255–33 269, 2015.

[151] X. Zhu, C. Vannahme, E. Højlund-Nielsen, N. A. Mortensen, and A. Kristensen, “Plasmonic colour laser printing,” *Nature nanotechnology*, vol. 11, no. 4, pp. 325–329, 2016.

[152] T. Ung, L. M. Liz-Marzán, and P. Mulvaney, “Controlled method for silica coating of silver colloids. influence of coating on the rate of chemical reactions,” *Langmuir*, vol. 14, no. 14, pp. 3740–3748, 1998.

[153] V. Lioubimov, A. Kolomenskii, A. Mershin, D. V. Nanopoulos, and H. A. Schuessler, “Effect of varying electric potential on surface-plasmon resonance sensing,” *Applied optics*, vol. 43, no. 17, pp. 3426–3432, 2004.

[154] C. Novo, A. M. Funston, and P. Mulvaney, “Direct observation of chemical reactions on single gold nanocrystals using surface plasmon spectroscopy,” *Nature nanotechnology*, vol. 3, no. 10, pp. 598–602, 2008.

[155] A. Yang, A. J. Hryn, M. R. Bourgeois, W.-K. Lee, J. Hu, G. C. Schatz, and T. W. Odom, “Programmable and reversible plasmon mode engineering,” *Proceedings of the National Academy of Sciences*, vol. 113, no. 50, pp. 14 201–14 206, 2016.

[156] F. Huang and J. J. Baumberg, “Actively tuned plasmons on elastomerically driven au nanoparticle dimers,” *Nano letters*, vol. 10, no. 5, pp. 1787–1792, 2010.

[157] H.-S. Ee and R. Agarwal, “Tunable metasurface and flat optical zoom lens on a stretchable substrate,” *Nano letters*, vol. 16, no. 4, pp. 2818–2823, 2016.

[158] J. Li, S. Kamin, G. Zheng, F. Neubrech, S. Zhang, and N. Liu, “Addressable metasurfaces for dynamic holography and optical information encryption,” *Science advances*, vol. 4, no. 6, p. eaar6768, 2018.

[159] W.-S. Chang, J. B. Lassiter, P. Swanglap, H. Sobhani, S. Khatua, P. Nordlander, N. J. Halas, and S. Link, “A plasmonic fano switch,” *Nano letters*, vol. 12, no. 9, pp. 4977–4982, 2012.

[160] A. Espinosa-Soria, E. Pinilla-Cienfuegos, F. J. Díaz-Fernández, A. Griol, J. Martí, and A. Martínez, “Coherent control of a plasmonic nanoantenna integrated on a silicon chip,” *ACS Photonics*, vol. 5, no. 7, pp. 2712–2717, 2018.

[161] N. Hardy, A. Habib, T. Ivanov, and A. A. Yanik, “Neuro-swarm^3: System-on-a-nanoparticle for wireless recording of brain activity,” *IEEE Photonics Technology Letters*, vol. 33, no. 16, pp. 900–903, 2021.

[162] X. Duan, S. Kamin, and N. Liu, “Dynamic plasmonic colour display,” *Nature communications*, vol. 8, no. 1, pp. 1–9, 2017.

[163] T. Sannomiya, H. Dermutz, C. Hafner, J. Vörös, and A. B. Dahlin, “Electrochemistry on a localized surface plasmon resonance sensor,” *Langmuir*, vol. 26, no. 10, pp. 7619–7626, 2010.

[164] N. Strohfeldt, J. Zhao, A. Tittl, and H. Giessen, “Sensitivity engineering in direct contact palladium-gold nano-sandwich hydrogen sensors,” *Optical Materials Express*, vol. 5, no. 11, pp. 2525–2535, 2015.

[165] W. M. Wilson, J. W. Stewart, and M. H. Mikkelsen, “Surpassing single line width active tuning with photochromic molecules coupled to plasmonic nanoantennas,” *Nano Letters*, vol. 18, no. 2, pp. 853–858, 2018.

[166] V. Stockhausen, P. Martin, J. Ghilane, Y. Leroux, H. Randriamahazaka, J. Grand, N. Felidj, and J. C. Lacroix, “Giant plasmon resonance shift using poly (3, 4-

ethylenedioxythiophene) electrochemical switching," *Journal of the American Chemical Society*, vol. 132, no. 30, pp. 10 224–10 226, 2010.

[167] B. Kim, J. K. Koh, J. Park, C. Ahn, J. Ahn, J. H. Kim, and S. Jeon, "Patternable pedot nanofilms with grid electrodes for transparent electrochromic devices targeting thermal camouflage," *Nano convergence*, vol. 2, no. 1, pp. 1–7, 2015.

[168] L. De Sio, A. Cunningham, V. Verrina, C. M. Tone, R. Caputo, T. Bürgi, and C. Umeton, "Double active control of the plasmonic resonance of a gold nanoparticle array," *Nanoscale*, vol. 4, no. 24, pp. 7619–7623, 2012.

[169] Y. Yao, M. A. Kats, P. Genevet, N. Yu, Y. Song, J. Kong, and F. Capasso, "Broad electrical tuning of graphene-loaded plasmonic antennas," *Nano letters*, vol. 13, no. 3, pp. 1257–1264, 2013.

[170] C. P. Byers, H. Zhang, D. F. Swearer, M. Yorulmaz, B. S. Hoener, D. Huang, A. Hoggard, W.-S. Chang, P. Mulvaney, E. Ringe *et al.*, "From tunable core-shell nanoparticles to plasmonic drawbridges: Active control of nanoparticle optical properties," *Science advances*, vol. 1, no. 11, p. e1500988, 2015.

[171] B. J. Roxworthy, A. M. Bhuiya, X. Yu, E. K. Chow, and K. C. Toussaint, "Reconfigurable nanoantennas using electron-beam manipulation," *Nature communications*, vol. 5, no. 1, pp. 1–7, 2014.

[172] C. Zhou, X. Duan, and N. Liu, "Dna-nanotechnology-enabled chiral plasmonics: from static to dynamic," *Accounts of chemical research*, vol. 50, no. 12, pp. 2906–2914, 2017.

[173] K. J. Palm, J. B. Murray, T. C. Narayan, and J. N. Munday, "Dynamic optical properties of metal hydrides," *ACS Photonics*, vol. 5, no. 11, pp. 4677–4686, 2018.

[174] T. Shegai, P. Johansson, C. Langhammer, and M. Käll, "Directional scattering and hydrogen sensing by bimetallic pd–au nanoantennas," *Nano letters*, vol. 12, no. 5, pp. 2464–2469, 2012.

[175] C. Wadell, F. A. A. Nugroho, E. Lidström, B. Iandolo, J. B. Wagner, and C. Langhammer, "Hysteresis-free nanoplasmonic pd–au alloy hydrogen sensors," *Nano letters*, vol. 15, no. 5, pp. 3563–3570, 2015.

[176] F. Den Broeder, S. Van der Molen, M. Kremers, J. Huiberts, D. Nagengast, A. Van Gogh, W. Huisman, N. Koeman, B. Dam, J. Rector *et al.*, "Visualization of hydrogen migration in solids using switchable mirrors," *Nature*, vol. 394, no. 6694, pp. 656–658, 1998.

[177] X. Duan and N. Liu, "Scanning plasmonic color display," *ACS nano*, vol. 12, no. 8, pp. 8817–8823, 2018.

[178] X. Duan, S. Kamin, F. Sterl, H. Giessen, and N. Liu, "Hydrogen-regulated chiral nanoplasmonics," *Nano Letters*, vol. 16, no. 2, pp. 1462–1466, 2016.

[179] Y. Sun, C. Shen, Q. Lai, W. Liu, D.-W. Wang, and K.-F. Aguey-Zinsou, "Tailoring magnesium based materials for hydrogen storage through synthesis: Current state of the art," *Energy Storage Materials*, vol. 10, pp. 168–198, 2018.

[180] J. Kern, R. Kullock, J. Prangsma, M. Emmerling, M. Kamp, and B. Hecht, "Electrically driven optical antennas," *Nature Photonics*, vol. 9, no. 9, pp. 582–586, 2015.

[181] J. C. Prangsma, J. Kern, A. G. Knapp, S. Grossmann, M. Emmerling, M. Kamp, and B. Hecht, "Electrically connected resonant optical antennas," *Nano letters*, vol. 12, no. 8, pp. 3915–3919, 2012.

[182] J. Yan, C. Ma, P. Liu, C. Wang, and G. Yang, "Electrically controlled scattering in a hybrid dielectric-plasmonic nanoantenna," *Nano Letters*, vol. 17, no. 8, pp. 4793–4800, 2017.

[183] X. Liu, J.-H. Kang, H. Yuan, J. Park, Y. Cui, H. Y. Hwang, and M. L. Brongersma, "Tuning of plasmons in transparent conductive oxides by carrier accumulation," *Acs Photonics*, vol. 5, no. 4, pp. 1493–1498, 2018.

[184] A. Melikyan, N. Lindenmann, S. Walheim, P. Leufke, S. Ulrich, J. Ye, P. Vincze, H. Hahn, T. Schimmel, C. Koos *et al.*, "Surface plasmon polariton absorption modulator," *Optics express*, vol. 19, no. 9, pp. 8855–8869, 2011.

[185] J. McIntyre, "Electrochemical modulation spectroscopy," *Surface science*, vol. 37, pp. 658–682, 1973.

[186] S. A. Abayzeed, R. J. Smith, K. F. Webb, M. G. Somekh, and C. W. See, “Sensitive detection of voltage transients using differential intensity surface plasmon resonance system,” *Optics express*, vol. 25, no. 25, pp. 31 552–31 567, 2017.

[187] V. E. Babicheva, A. Boltasseva, and A. V. Lavrinenko, “Transparent conducting oxides for electro-optical plasmonic modulators,” *Nanophotonics*, vol. 1, no. open-issue, pp. 165–185, 2015.

[188] A. M. Brown, M. T. Sheldon, and H. A. Atwater, “Electrochemical tuning of the dielectric function of au nanoparticles,” *ACS Photonics*, vol. 2, no. 4, pp. 459–464, 2015.

[189] C. Novo, A. M. Funston, A. K. Gooding, and P. Mulvaney, “Electrochemical charging of single gold nanorods,” *Journal of the American Chemical Society*, vol. 131, no. 41, pp. 14 664–14 666, 2009.

[190] S. S. Collins, X. Wei, T. G. McKenzie, A. M. Funston, and P. Mulvaney, “Single gold nanorod charge modulation in an ion gel device,” *Nano Letters*, vol. 16, no. 11, pp. 6863–6869, 2016.

[191] Y. Huang, M. C. Pitter, and M. G. Somekh, “Morphology-dependent voltage sensitivity of a gold nanostructure,” *Langmuir*, vol. 27, no. 22, pp. 13 950–13 961, 2011.

[192] W. Ou, Y. Zou, K. Wang, W. Gong, R. Pei, L. Chen, Z. Pan, D. Fu, X. Huang, Y. Zhao *et al.*, “Active manipulation of nir plasmonics: the case of cu2–x se through electrochemistry,” *The journal of physical chemistry letters*, vol. 9, no. 2, pp. 274–280, 2018.

[193] H. Zhou, Q. Liu, F. J. Rawson, W. Ma, D.-W. Li, D. Li, and Y.-T. Long, “Optical monitoring of faradaic reaction using single plasmon-resonant nanorods functionalized with graphene,” *Chemical Communications*, vol. 51, no. 15, pp. 3223–3226, 2015.

[194] X. Shan, U. Patel, S. Wang, R. Iglesias, and N. Tao, “Imaging local electrochemical current via surface plasmon resonance,” *Science*, vol. 327, no. 5971, pp. 1363–1366, 2010.

[195] Y. Huang, M. C. Pitter, and M. G. Somekh, “Time-dependent scattering of ultrathin gold film under potential perturbation,” *ACS Applied Materials & Interfaces*, vol. 4, no. 8, pp. 3829–3836, 2012.

[196] T. Ung, M. Giersig, D. Dunstan, and P. Mulvaney, “Spectroelectrochemistry of colloidal silver,” *Langmuir*, vol. 13, no. 6, pp. 1773–1782, 1997.

[197] S. Dondapati, M. Ludemann, R. Muller, S. Schwieger, A. Schwemer, B. Handel, D. Kwiatkowski, M. Djiango, E. Runge, and T. Klar, “Voltage-induced adsorbate damping of single gold nanorod plasmons in aqueous solution,” *Nano letters*, vol. 12, no. 3, pp. 1247–1252, 2012.

[198] Y. Li, J. T. Cox, and B. Zhang, “Electrochemical responses and electrocatalysis at single au nanoparticles,” *Journal of the American Chemical Society*, vol. 132, no. 9, pp. 3047–3054, 2010.

[199] X. Xiao, F.-R. F. Fan, J. Zhou, and A. J. Bard, “Current transients in single nanoparticle collision events,” *Journal of the American Chemical Society*, vol. 130, no. 49, pp. 16 669–16 677, 2008.

[200] P. Peljo, M. D. Scanlon, A. J. Olaya, L. Rivier, E. Smirnov, and H. H. Girault, “Redox electrocatalysis of floating nanoparticles: determining electrocatalytic properties without the influence of solid supports,” *The Journal of Physical Chemistry Letters*, vol. 8, no. 15, pp. 3564–3575, 2017.

[201] Y. Fang, H. Wang, H. Yu, X. Liu, W. Wang, H.-Y. Chen, and N. Tao, “Plasmonic imaging of electrochemical reactions of single nanoparticles,” *Accounts of Chemical Research*, vol. 49, no. 11, pp. 2614–2624, 2016.

[202] C. Novo and P. Mulvaney, “Charge-induced rayleigh instabilities in small gold rods,” *Nano letters*, vol. 7, no. 2, pp. 520–524, 2007.

[203] C. Jing, F. J. Rawson, H. Zhou, X. Shi, W.-H. Li, D.-W. Li, and Y.-T. Long, “New insights into electrocatalysis based on plasmon resonance for the real-time monitoring of catalytic events on single gold nanorods,” *Analytical chemistry*, vol. 86, no. 11, pp. 5513–5518, 2014.

[204] P. Saha, J. W. Hill, J. D. Walmsley, and C. M. Hill, “Probing electrocatalysis at individual au nanorods via correlated optical and electrochemical measurements,” *Analytical chemistry*, vol. 90, no. 21, pp. 12 832–12 839, 2018.

[205] G. Lei, P. F. Gao, T. Yang, J. Zhou, H. Z. Zhang, S. S. Sun, M. X. Gao, and C. Z. Huang, "Photoinduced electron transfer process visualized on single silver nanoparticles," *ACS nano*, vol. 11, no. 2, pp. 2085–2093, 2017.

[206] Y. Wang, X. Shan, H. Wang, S. Wang, and N. Tao, "Plasmonic imaging of surface electrochemical reactions of single gold nanowires," *Journal of the American Chemical Society*, vol. 139, no. 4, pp. 1376–1379, 2017.

[207] C. P. Byers, B. S. Hoener, W.-S. Chang, S. Link, and C. F. Landes, "Single-particle plasmon voltammetry (sppv) for detecting anion adsorption," *Nano Letters*, vol. 16, no. 4, pp. 2314–2321, 2016.

[208] Y. Du, X. Cui, L. Li, H. Tian, W.-X. Yu, and Z.-X. Zhou, "Dielectric properties of dmso-doped-pedot: Pss at thz frequencies," *physica status solidi (b)*, vol. 255, no. 4, p. 1700547, 2018.

[209] P. A. Kossyrev, A. Yin, S. G. Cloutier, D. A. Cardimona, D. Huang, P. M. Alsing, and J. M. Xu, "Electric field tuning of plasmonic response of nanodot array in liquid crystal matrix," *Nano letters*, vol. 5, no. 10, pp. 1978–1981, 2005.

[210] A. Abass, S. R.-K. Rodriguez, T. Ako, T. Aubert, M. Verschuuren, D. Van Thourhout, J. Beeckman, Z. Hens, J. Gómez Rivas, and B. Maes, "Active liquid crystal tuning of metallic nanoantenna enhanced light emission from colloidal quantum dots," *Nano letters*, vol. 14, no. 10, pp. 5555–5560, 2014.

[211] V. K. Hsiao, Y. B. Zheng, B. K. Juluri, and T. J. Huang, "Light-driven plasmonic switches based on au nanodisk arrays and photoresponsive liquid crystals," *Advanced Materials*, vol. 20, no. 18, pp. 3528–3532, 2008.

[212] J. Berthelot, A. Bouhelier, C. Huang, J. Margueritat, G. Colas-des Francs, E. Finot, J.-C. Weeber, A. Dereux, S. Kostcheev, H. I. E. Ahrach *et al.*, "Tuning of an optical dimer nanoantenna by electrically controlling its load impedance," *Nano letters*, vol. 9, no. 11, pp. 3914–3921, 2009.

[213] M. J. Dicken, L. A. Sweatlock, D. Pacifici, H. J. Lezec, K. Bhattacharya, and H. A. At-

water, “Electrooptic modulation in thin film barium titanate plasmonic interferometers,” *Nano letters*, vol. 8, no. 11, pp. 4048–4052, 2008.

[214] M. Kauranen and A. V. Zayats, “Nonlinear plasmonics,” *Nature photonics*, vol. 6, no. 11, pp. 737–748, 2012.

[215] M. Abb, P. Albella, J. Aizpurua, and O. L. Muskens, “All-optical control of a single plasmonic nanoantenna–ito hybrid,” *Nano letters*, vol. 11, no. 6, pp. 2457–2463, 2011.

[216] R. A. Pala, K. T. Shimizu, N. A. Melosh, and M. L. Brongersma, “A nonvolatile plasmonic switch employing photochromic molecules,” *Nano Letters*, vol. 8, no. 5, pp. 1506–1510, 2008.

[217] X. Yin, M. Schäferling, A.-K. U. Michel, A. Tittl, M. Wuttig, T. Taubner, and H. Giessen, “Active chiral plasmonics,” *Nano letters*, vol. 15, no. 7, pp. 4255–4260, 2015.

[218] Y. Abate, R. E. Marvel, J. I. Ziegler, S. Gamage, M. H. Javani, M. I. Stockman, and R. F. Haglund, “Control of plasmonic nanoantennas by reversible metal-insulator transition,” *Scientific reports*, vol. 5, p. 13997, 2015.

[219] N. A. Butakov, I. Valmianski, T. Lewi, C. Urban, Z. Ren, A. A. Mikhailovsky, S. D. Wilson, I. K. Schuller, and J. A. Schuller, “Switchable plasmonic–dielectric resonators with metal–insulator transitions,” *Acs Photonics*, vol. 5, no. 2, pp. 371–377, 2018.

[220] S. K. Earl, T. D. James, T. J. Davis, J. C. McCallum, R. E. Marvel, R. F. Haglund, and A. Roberts, “Tunable optical antennas enabled by the phase transition in vanadium dioxide,” *Optics express*, vol. 21, no. 22, pp. 27 503–27 508, 2013.

[221] A.-K. U. Michel, P. Zalden, D. N. Chigrin, M. Wuttig, A. M. Lindenberg, and T. Taubner, “Reversible optical switching of infrared antenna resonances with ultrathin phase-change layers using femtosecond laser pulses,” *Acs Photonics*, vol. 1, no. 9, pp. 833–839, 2014.

[222] M. K. Gupta, S. Chang, S. Singamaneni, L. F. Drummy, R. Gunawidjaja, R. R. Naik, and V. V. Tsukruk, “ph-triggered sers via modulated plasmonic coupling in individual bimetallic nanocobs,” *Small*, vol. 7, no. 9, pp. 1192–1198, 2011.

[223] V. Kozlovskaya, E. Kharlampieva, B. P. Khanal, P. Manna, E. R. Zubarev, and V. V. Tsukruk, “Ultrathin layer-by-layer hydrogels with incorporated gold nanorods as ph-sensitive optical materials,” *Chemistry of materials*, vol. 20, no. 24, pp. 7474–7485, 2008.

[224] Y. R. Leroux, J. C. Lacroix, K. I. Chane-Ching, C. Fave, N. Félidj, G. Lévi, J. Aubard, J. R. Krenn, and A. Hohenau, “Conducting polymer electrochemical switching as an easy means for designing active plasmonic devices,” *Journal of the American Chemical Society*, vol. 127, no. 46, pp. 16 022–16 023, 2005.

[225] Y. Leroux, J. C. Lacroix, C. Fave, G. Trippe, N. Félidj, J. Aubard, A. Hohenau, and J. R. Krenn, “Tunable electrochemical switch of the optical properties of metallic nanoparticles,” *ACS nano*, vol. 2, no. 4, pp. 728–732, 2008.

[226] C. A. Balanis, *Antenna theory: analysis and design*. John wiley & sons, 2015.

[227] N. Large, M. Abb, J. Aizpurua, and O. L. Muskens, “Photoconductively loaded plasmonic nanoantenna as building block for ultracompact optical switches,” *Nano letters*, vol. 10, no. 5, pp. 1741–1746, 2010.

[228] D. M. O’Carroll, J. S. Fakonas, D. M. Callahan, M. Schierhorn, and H. A. Atwater, “Metal–polymer–metal split-dipole nanoantennas,” *Advanced Materials*, vol. 24, no. 23, pp. OP136–OP142, 2012.

[229] Q. Zhang, J.-J. Xiao, M. Li, D. Han, and L. Gao, “Coexistence of scattering enhancement and suppression by plasmonic cavity modes in loaded dimer gap-antennas,” *Scientific reports*, vol. 5, no. 1, pp. 1–10, 2015.

[230] Z. Xu, Y. Hou, and S. Sun, “Magnetic core/shell fe3o4/au and fe3o4/au/ag nanoparticles with tunable plasmonic properties,” *Journal of the American Chemical Society*, vol. 129, no. 28, pp. 8698–8699, 2007.

[231] J.-W. Jeon, P. A. Ledin, J. A. Geldmeier, J. F. Ponder Jr, M. A. Mahmoud, M. El-Sayed, J. R. Reynolds, and V. V. Tsukruk, “Electrically controlled plasmonic behavior of gold nanocube@ polyaniline nanostructures: Transparent plasmonic aggregates,” *Chemistry of Materials*, vol. 28, no. 8, pp. 2868–2881, 2016.

[232] W. Lu, N. Jiang, and J. Wang, "Active electrochemical plasmonic switching on polyaniline-coated gold nanocrystals," *Advanced Materials*, vol. 29, no. 8, p. 1604862, 2017.

[233] D. F. Swearer, H. Zhao, L. Zhou, C. Zhang, H. Robatjazi, J. M. P. Martirez, C. M. Krauter, S. Yazdi, M. J. McClain, E. Ringe *et al.*, "Heterometallic antenna- reactor complexes for photocatalysis," *Proceedings of the National Academy of Sciences*, vol. 113, no. 32, pp. 8916–8920, 2016.

[234] I. Zubritskaya, N. Maccaferri, X. Inchausti Ezeiza, P. Vavassori, and A. Dmitriev, "Magnetic control of the chiroptical plasmonic surfaces," *Nano letters*, vol. 18, no. 1, pp. 302–307, 2018.

[235] Y. B. Zheng, Y.-W. Yang, L. Jensen, L. Fang, B. K. Juluri, A. H. Flood, P. S. Weiss, J. F. Stoddart, and T. J. Huang, "Active molecular plasmonics: controlling plasmon resonances with molecular switches," *Nano letters*, vol. 9, no. 2, pp. 819–825, 2009.

[236] H. Gehan, C. Mangeney, J. Aubard, G. Lévi, A. Hohenau, J. R. Krenn, E. Lacaze, and N. Félidj, "Design and optical properties of active polymer-coated plasmonic nanostructures," *The journal of physical chemistry letters*, vol. 2, no. 8, pp. 926–931, 2011.

[237] D. Schaming, V.-Q. Nguyen, P. Martin, and J.-C. Lacroix, "Tunable plasmon resonance of gold nanoparticles functionalized by electroactive bisthienylbenzene oligomers or polythiophene," *The Journal of Physical Chemistry C*, vol. 118, no. 43, pp. 25 158–25 166, 2014.

[238] P.-Y. Chen, C. Argyropoulos, and A. Alù, "Enhanced nonlinearities using plasmonic nanoantennas," *Nanophotonics*, vol. 1, no. 3-4, pp. 221–233, 2012.

[239] A. Yin, Q. He, Z. Lin, L. Luo, Y. Liu, S. Yang, H. Wu, M. Ding, Y. Huang, and X. Duan, "Plasmonic/nonlinear optical material core/shell nanorods as nanoscale plasmon modulators and optical voltage sensors," *Angewandte Chemie International Edition*, vol. 55, no. 2, pp. 583–587, 2016.

[240] N. Jiang, L. Shao, and J. Wang, "(gold nanorod core)/(polyaniline shell) plasmonic

switches with large plasmon shifts and modulation depths," *Advanced Materials*, vol. 26, no. 20, pp. 3282–3289, 2014.

[241] J. Zhou, S. R. Panikkanvalappil, S. Kang, S. Yu, S. Zhang, M. El-Sayed, and V. V. Tsukruk, "Enhanced electrochemical dark-field scattering modulation on a single hybrid core–shell nanostructure," *The Journal of Physical Chemistry C*, vol. 123, no. 46, pp. 28 343–28 352, 2019.

[242] I. M. Pryce, K. Aydin, Y. A. Kelaita, R. M. Briggs, and H. A. Atwater, "Highly strained compliant optical metamaterials with large frequency tunability," *Nano letters*, vol. 10, no. 10, pp. 4222–4227, 2010.

[243] D. Wang, M. R. Bourgeois, W.-K. Lee, R. Li, D. Trivedi, M. P. Knudson, W. Wang, G. C. Schatz, and T. W. Odom, "Stretchable nanolasing from hybrid quadrupole plasmons," *Nano letters*, vol. 18, no. 7, pp. 4549–4555, 2018.

[244] A. Kuzyk, R. Jungmann, G. P. Acuna, and N. Liu, "Dna origami route for nanophotonics," *ACS photonics*, vol. 5, no. 4, pp. 1151–1163, 2018.

[245] C. Thomas Jr, P. Springer, G. Loeb, Y. Berwald-Netter, and L. Okun, "A miniature microelectrode array to monitor the bioelectric activity of cultured cells," *Experimental cell research*, vol. 74, no. 1, pp. 61–66, 1972.

[246] P. Connolly, P. Clark, A. Curtis, J. Dow, and C. Wilkinson, "An extracellular microelectrode array for monitoring electrogenic cells in culture," *Biosensors and Bioelectronics*, vol. 5, no. 3, pp. 223–234, 1990.

[247] D. Tsai, D. Sawyer, A. Bradd, R. Yuste, and K. L. Shepard, "A very large-scale microelectrode array for cellular-resolution electrophysiology," *Nature Communications*, vol. 8, no. 1, pp. 1–11, 2017.

[248] M. E. J. Obien, K. Deligkaris, T. Bullmann, D. J. Bakkum, and U. Frey, "Revealing neuronal function through microelectrode array recordings," *Frontiers in neuroscience*, vol. 8, p. 423, 2015.

[249] E. S. Boyden, "Optogenetics and the future of neuroscience," *Nature neuroscience*, vol. 18, no. 9, pp. 1200–1201, 2015.

[250] M. Bresadola, “Animal electricity at the end of the eighteenth century: the many facets of a great scientific controversy,” *Journal of the History of the Neurosciences*, vol. 17, no. 1, pp. 8–32, 2008.

[251] S. D. Antic, R. M. Empson, and T. Knöpfel, “Voltage imaging to understand connections and functions of neuronal circuits,” *Journal of neurophysiology*, vol. 116, no. 1, pp. 135–152, 2016.

[252] R. M. Wightman, “Probing cellular chemistry in biological systems with microelectrodes,” *Science*, vol. 311, no. 5767, pp. 1570–1574, 2006.

[253] M. E. Spira and A. Hai, “Multi-electrode array technologies for neuroscience and cardiology,” *Nature nanotechnology*, vol. 8, no. 2, p. 83, 2013.

[254] G. Buzsáki, C. A. Anastassiou, and C. Koch, “The origin of extracellular fields and currents—eeg, ecog, lfp and spikes,” *Nature reviews neuroscience*, vol. 13, no. 6, pp. 407–420, 2012.

[255] V. Emmenegger, M. E. J. Obien, F. Franke, and A. Hierlemann, “Technologies to study action potential propagation with a focus on hd-meas,” *Frontiers in cellular neuroscience*, vol. 13, p. 159, 2019.

[256] G. Hong and C. M. Lieber, “Novel electrode technologies for neural recordings,” *Nature Reviews Neuroscience*, vol. 20, no. 6, pp. 330–345, 2019.

[257] V. Viswam, M. E. J. Obien, F. Franke, U. Frey, and A. Hierlemann, “Optimal electrode size for multi-scale extracellular-potential recording from neuronal assemblies,” *Frontiers in neuroscience*, vol. 13, p. 385, 2019.

[258] V. Emiliani, A. E. Cohen, K. Deisseroth, and M. Häusser, “All-optical interrogation of neural circuits,” *Journal of Neuroscience*, vol. 35, no. 41, pp. 13 917–13 926, 2015.

[259] T. Knöpfel, J. Díez-García, and W. Akemann, “Optical probing of neuronal circuit dynamics: genetically encoded versus classical fluorescent sensors,” *Trends in neurosciences*, vol. 29, no. 3, pp. 160–166, 2006.

[260] A. L. Efros, J. B. Delehanty, A. L. Huston, I. L. Medintz, M. Barbic, and T. D. Harris, “Evaluating the potential of using quantum dots for monitoring electrical signals in neurons,” *Nature nanotechnology*, vol. 13, no. 4, pp. 278–288, 2018.

[261] J. D. Marshall and M. J. Schnitzer, “Optical strategies for sensing neuronal voltage using quantum dots and other semiconductor nanocrystals,” *Acs Nano*, vol. 7, no. 5, pp. 4601–4609, 2013.

[262] S. A. Kim, K. M. Byun, J. Lee, J. H. Kim, D.-G. A. Kim, H. Baac, M. L. Shuler, and S. J. Kim, “Optical measurement of neural activity using surface plasmon resonance,” *Optics letters*, vol. 33, no. 9, pp. 914–916, 2008.

[263] S. A. Kim, S. J. Kim, H. Moon, and S. B. Jun, “In vivo optical neural recording using fiber-based surface plasmon resonance,” *Optics letters*, vol. 37, no. 4, pp. 614–616, 2012.

[264] P. K. Jain, K. S. Lee, I. H. El-Sayed, and M. A. El-Sayed, “Calculated absorption and scattering properties of gold nanoparticles of different size, shape, and composition: applications in biological imaging and biomedicine,” *The journal of physical chemistry B*, vol. 110, no. 14, pp. 7238–7248, 2006.

[265] M. C. Pitter, J. Paul, J. Zhang, and M. G. Somekh, “Limits to non-fluorescent voltage sensitivity using surface and particle plasmons,” in *Photons and Neurons*, vol. 7180. International Society for Optics and Photonics, 2009, p. 718006.

[266] A. Baba, J. Lübben, K. Tamada, and W. Knoll, “Optical properties of ultrathin poly (3, 4-ethylenedioxythiophene) films at several doping levels studied by in situ electrochemical surface plasmon resonance spectroscopy,” *Langmuir*, vol. 19, no. 21, pp. 9058–9064, 2003.

[267] E. D. Palik, *Handbook of optical constants of solids*. Academic press, 1998, vol. 3.

[268] A. Acun, T. D. Nguyen, and P. Zorlutuna, “An aged human heart tissue model showing age-related molecular and functional deterioration resembling the native heart,” *bioRxiv*, p. 287334, 2018.

[269] B. W. Ellis, A. Acun, U. I. Can, and P. Zorlutuna, “Human ipsc-derived myocardium-on-chip with capillary-like flow for personalized medicine,” *Biomicrofluidics*, vol. 11, no. 2, p. 024105, 2017.

[270] X. Lian, J. Zhang, S. M. Azarin, K. Zhu, L. B. Hazeltine, X. Bao, C. Hsiao, T. J. Kamp, and S. P. Palecek, “Directed cardiomyocyte differentiation from human pluripotent stem cells by modulating wnt/β-catenin signaling under fully defined conditions,” *Nature protocols*, vol. 8, no. 1, pp. 162–175, 2013.

[271] Z. J. Coppens, W. Li, D. G. Walker, and J. G. Valentine, “Probing and controlling photothermal heat generation in plasmonic nanostructures,” *Nano letters*, vol. 13, no. 3, pp. 1023–1028, 2013.

[272] V. Jain, H. M. Yochum, R. Montazami, and J. R. Heflin, “Millisecond switching in solid state electrochromic polymer devices fabricated from ionic self-assembled multilayers,” *Applied Physics Letters*, vol. 92, no. 3, p. 20, 2008.

[273] A. Elschner, S. Kirchmeyer, W. Lovenich, U. Merker, and K. Reuter, *PEDOT: principles and applications of an intrinsically conductive polymer*. CRC press, 2010.

[274] K. A. Ludwig, N. B. Langhals, M. D. Joseph, S. M. Richardson-Burns, J. L. Hendricks, and D. R. Kipke, “Poly (3, 4-ethylenedioxythiophene)(pedot) polymer coatings facilitate smaller neural recording electrodes,” *Journal of neural engineering*, vol. 8, no. 1, p. 014001, 2011.

[275] X. Cui and D. C. Martin, “Electrochemical deposition and characterization of poly (3, 4-ethylenedioxythiophene) on neural microelectrode arrays,” *Sensors and Actuators B: Chemical*, vol. 89, no. 1-2, pp. 92–102, 2003.

[276] C. Bédard and A. Destexhe, “Macroscopic models of local field potentials and the apparent 1/f noise in brain activity,” *Biophysical journal*, vol. 96, no. 7, pp. 2589–2603, 2009.

[277] S. Sylantyev, L. P. Savtchenko, Y.-P. Niu, A. I. Ivanov, T. P. Jensen, D. M. Kullmann, M.-Y. Xiao, and D. A. Rusakov, “Electric fields due to synaptic currents sharpen excitatory transmission,” *Science*, vol. 319, no. 5871, pp. 1845–1849, 2008.

[278] S. A. Empedocles and M. G. Bawendi, "Quantum-confined stark effect in single cdse nanocrystallite quantum dots," *Science*, vol. 278, no. 5346, pp. 2114–2117, 1997.

[279] S. H. Chang, C.-H. Chiang, F.-S. Kao, C.-L. Tien, and C.-G. Wu, "Unraveling the enhanced electrical conductivity of pedot: Pss thin films for ito-free organic photovoltaics," *IEEE Photonics Journal*, vol. 6, no. 4, pp. 1–7, 2014.

[280] K.-Y. Jung, W.-J. Yoon, Y. B. Park, P. R. Berger, and F. L. Teixeira, "Broadband finite-difference time-domain modeling of plasmonic organic photovoltaics," *ETRI Journal*, vol. 36, no. 4, pp. 654–661, 2014.

[281] C. A. DiMarzio, *Optics for engineers*. Crc Press, 2011.

[282] G. P. Farman, K. Tachampa, R. Mateja, O. Cazorla, A. Lacampagne, and P. P. de Tombe, "Blebbistatin: use as inhibitor of muscle contraction," *Pflügers Archiv-European Journal of Physiology*, vol. 455, no. 6, pp. 995–1005, 2008.

[283] J. Abbott, T. Ye, L. Qin, M. Jorgolli, R. S. Gertner, D. Ham, and H. Park, "Cmos nanoelectrode array for all-electrical intracellular electrophysiological imaging," *Nature nanotechnology*, vol. 12, no. 5, pp. 460–466, 2017.

[284] P. P. Laissue, R. A. Alghamdi, P. Tomancak, E. G. Reynaud, and H. Shroff, "Assessing phototoxicity in live fluorescence imaging," *Nature methods*, vol. 14, no. 7, pp. 657–661, 2017.

[285] K. F. MacDonald, Z. L. Sámson, M. I. Stockman, and N. I. Zheludev, "Ultrafast active plasmonics," *Nature Photonics*, vol. 3, no. 1, pp. 55–58, 2009.

[286] Y. Li, J. van de Groep, A. A. Talin, and M. L. Brongersma, "Dynamic tuning of gap plasmon resonances using a solid-state electrochromic device," *Nano Letters*, vol. 19, no. 11, pp. 7988–7995, 2019.

[287] J. Harden, A. Joshi, and J. D. Serna, "Demonstration of double eit using coupled harmonic oscillators and rlc circuits," *European journal of physics*, vol. 32, no. 2, p. 541, 2011.

[288] D. Tu and R. Forchheimer, "Self-oscillation in electrochemical transistors: An rlc modeling approach," *Solid-state electronics*, vol. 69, pp. 7–10, 2012.

[289] E. Barsoukov and J. Macdonald, *Impedance Spectroscopy: Theory, Experiment, and Applications*. Wiley, 2005. [Online]. Available: https://books.google.com/books?id=8hNkOWO_DLwC

[290] P. Danielsson, J. Bobacka, and A. Ivaska, "Electrochemical synthesis and characterization of poly (3, 4-ethylenedioxythiophene) in ionic liquids with bulky organic anions," *Journal of Solid State Electrochemistry*, vol. 8, no. 10, pp. 809–817, 2004.

[291] A. Vacca, M. Mascia, S. Rizzardini, S. Corgiolu, S. Palmas, M. Demelas, A. Bonfiglio, and P. C. Ricci, "Preparation and characterisation of transparent and flexible pedot: Pss/pani electrodes by ink-jet printing and electropolymerisation," *RSC advances*, vol. 5, no. 97, pp. 79 600–79 606, 2015.

[292] M. Atighilorestani, D. P. dos Santos, R. F. Jaimes, M. M. Rahman, M. L. Temperini, and A. G. Brolo, "Electrochemical control of light transmission through nanohole electrode arrays," *ACS Photonics*, vol. 3, no. 12, pp. 2375–2382, 2016.

[293] J.-K. Yoon, E.-M. Park, J.-S. Son, H.-W. Shin, H.-E. Kim, M. Yee, H.-G. Kim, C.-H. Oh, and B.-C. Ahn, "27.2: the study of picture quality of oled tv with wrgb oleds structure," in *SID Symposium Digest of Technical Papers*, vol. 44, no. 1. Wiley Online Library, 2013, pp. 326–329.

[294] A. E. Çetin, A. A. Yanik, A. Mertiri, S. Erramilli, Ö. E. Müstecaplıoğlu, and H. Altug, "Field-effect active plasmonics for ultracompact electro-optic switching," *Applied Physics Letters*, vol. 101, no. 12, p. 121113, 2012.

[295] J. Luo, D. Billep, T. Waechtler, T. Otto, M. Toader, O. Gordan, E. Sheremet, J. Martin, M. Hietschold, D. R. Zahn *et al.*, "Enhancement of the thermoelectric properties of pedot: Pss thin films by post-treatment," *Journal of Materials Chemistry A*, vol. 1, no. 26, pp. 7576–7583, 2013.

[296] D. M. DeLongchamp, M. Kastantin, and P. T. Hammond, "High-contrast elec-

trochromism from layer-by-layer polymer films," *Chemistry of Materials*, vol. 15, no. 8, pp. 1575–1586, 2003.

[297] S. H. Lee, H. Y. Kim, S. M. Lee, S. H. Hong, J. M. Kim, J. W. Koh, J. Y. Lee, and H. S. Park, "Ultra-ffs tft-lcd with super image quality, fast response time, and strong pressure-resistant characteristics," *Journal of the Society for Information Display*, vol. 10, no. 2, pp. 117–122, 2002.

[298] J. H. Yoon, S. J. Lee, Y. J. Lim, E. J. Seo, H. S. Shin, J.-M. Myoung, and S. H. Lee, "Fast switching, high contrast and high resolution liquid crystal device for virtual reality display," *Optics Express*, vol. 26, no. 26, pp. 34 142–34 149, 2018.

[299] N. C. Lindquist, A. Lesuffleur, H. Im, and S.-H. Oh, "Sub-micron resolution surface plasmon resonance imaging enabled by nanohole arrays with surrounding bragg mirrors for enhanced sensitivity and isolation," *Lab on a Chip*, vol. 9, no. 3, pp. 382–387, 2009.

[300] L. Gao, Y. Zhang, H. Zhang, S. Doshay, X. Xie, H. Luo, D. Shah, Y. Shi, S. Xu, H. Fang *et al.*, "Optics and nonlinear buckling mechanics in large-area, highly stretchable arrays of plasmonic nanostructures," *Acs Nano*, vol. 9, no. 6, pp. 5968–5975, 2015.

[301] E. Prodan, C. Radloff, N. J. Halas, and P. Nordlander, "A hybridization model for the plasmon response of complex nanostructures," *science*, vol. 302, no. 5644, pp. 419–422, 2003.

[302] G. Hong, S. Diao, J. Chang, A. L. Antaris, C. Chen, B. Zhang, S. Zhao, D. N. Atochin, P. L. Huang, K. I. Andreasson *et al.*, "Through-skull fluorescence imaging of the brain in a new near-infrared window," *Nature photonics*, vol. 8, no. 9, pp. 723–730, 2014.

Index